HIGHER STATISTICS INVESTIGATION OF $K_s^0 K^-$ DECAY OF THE A_2^- PRODUCED BY 23-GeV/c π^- ON HYDROGEN

by

MARTIN MARGULIES

A dissertation submitted to the Graduate Faculty in Physics in partial fulfillment of the requirements for the degree of Doctor of Philosophy, The City University of New York.

1975

This manuscript has been read and accepted for the Graduate Faculty in Physics in satisfaction of the dissertation requirement for the degree of Doctor of Philosophy.

4/24/75
date

Chairman of Examining Committee

4/24/75
date

Executive Officer

Supervisory Committee

The City University of New York

ABSTRACT

HIGHER STATISTICS INVESTIGATION OF $K_s^o K^-$ DECAY OF THE A_2^-

PRODUCED BY 23 GeV/c π^- ON HYDROGEN

by

Martin Margulies

Advisor: Professor Seymour J. Lindenbaum

We have, using the BNL Mkl Spectrometer, obtained and analyzed 3346 new events of the type $\pi^- P \rightarrow K_s^o K^- + P$ in the effective mass range $M(K_s^o K^-)$ = 1.1-1.5 GeV. The effective mass resolution is σ_{rms} = 4.3 ± .2 MeV. The statistics represent ≃ a fivefold increase compared to the previous experiment. The $K_s^o K^-$ effective mass spectrum shows a single peak in the A_2 mass region which is well fitted by a D-wave Breit-Wigner shape. The data in the A_2 peak region agree with our previous results and rule out conclusively (> 7.9 standard deviations) the split A_2 shape reported earlier by other investigators. The background level is ∿ 10-20%.

The data have been subdivided into the following three t' regions, where $t' = t - t_{min}$ [†] in units of $(GeV/c)^2$: (a) $0 < -t' < .2$, (b) $0.2 < -t' < 0.29$, and (c) $.29 < -t'$, and each region is well fit by a single D-wave Breit-Wigner. No split is observed in any -t' region. The "double pole" formula used for the CERN missing mass data, even

---

[†] See Appendix A

with the more limited statistics for each subdivision, gives a χ^2 equivalent to $\geq$ 3.0 standard deviations for the dipole fits.

Total and differential cross-section measurements were made at 22.4 and 23.9 GeV/c. The parameterization $\frac{d\sigma}{dt'} \alpha -t'e^{bt'}$ describes the differential cross-section data with the parameter $b = 7.0 \pm .2$ $(GeV/c)^{-2}$.

The momentum dependence of the cross sections for the reaction

$$\pi^- P \rightarrow A_2^- P$$
$$\downarrow$$
$$K^o K^-$$

was obtained using our data and the data from other experiments.[1,2] A least-squares fit to the form $\sigma_{Total} \alpha P_{Lab}^{-N}$ yields a value for $N = 1.18 \pm .11$. The total cross section for the reaction

$$\pi^- P \rightarrow A_2^- P$$
$$\downarrow$$
$$K^o K^-$$

seems to have a momentum dependence which falls off faster than that reported by other investigators[3] for the $\rho^o \pi^-$ decay mode of the A_2^-.

We have measured the A_2 decay angular distribution in the Gottfried-Jackson frame for the $K^o K^-$ decay mode of the A_2^-. The angular distribution may be explained by a dominant exchange of natural spin parity vector mesons (i.e. ρ^o and f^o) in the production process. The A_2 angular distributions are consistent with those of a single resonance with a $J^P = 2^+$.

ACKNOWLEDGEMENTS

The experiment, because of its size and complexity, involved many individuals both directly and indirectly. First, I am deeply indebted to Professor Seymour J. Lindenbaum, the author's thesis advisor, for his continued inspiration, encouragement, and invaluable assistance throughout the experiment. I am also gratefully appreciative of the assistance, motivation, and insight of Dr. Satoshi Ozaki in all facets of the experiment.

The author wishes to thank all the members of the Lindenbaum-Ozaki group: Drs. Kenneth Foley, William Love, Martin Kramer, Edward Platner, Alfred Saulys, and Erich Willen, without whose assistance and professional expertise this experiment would not have been possible.

Thanks are due to Dr. R.M. Sternheimer for many useful discussions.

The author thanks the staff of the Brookhaven On-Line Data Facility for their cooperation and assistance. The members include Dominick Bartolomeo, Lloyd Davis, Art Friedman, John Gould, Dick Imossi, Wally Johnson, Herb Langenbach, and Charles Zein.

The author is grateful for the assistance offered by Steve Eiseman and Dr. William Miller during the course of the experiment. I would also like to acknowledge the efforts of our group technicians, M. Conforte, G. Leigh, T. Mogavero, A. Roesch, and R. Wheeler, in the construction and operation of this spectrometer.

Contributions of Miss Usha Mallik of her time and assistance during and after the experiment are appreciated.

The author thanks Miss Katherine Paynter and Mrs. Grace Schiro for their patience in the typing of this manuscript.

TABLE OF CONTENTS

TABLE OF CONTENTS (Cont'd.)

TABLE OF CONTENTS (Cont'd.)

TABLE OF CONTENTS (Cont'd.)

LIST OF TABLES

LIST OF TABLES (con't)

LIST OF TABLES (con't)

FIGURE CAPTIONS

FIGURE CAPTIONS (Cont'd.)

FIGURE CAPTIONS (Cont'd.)

CHAPTER I

INTRODUCTION

A. Motivation for Experiment

Several previous experiments observing the A_2 meson had found a double mass peak.[4-8] Other experiments had found no significant structure within the A_2 peak.[9-13] We wanted a high statistics, low background and good mass resolution experiment to study further the shape of the A_2 mass spectrum and also to investigate the possibility that the mass spectrum exhibits a split in limited t'* regions.

We were also interested in measuring the total cross section for the reaction

$$\pi^- P \rightarrow A_2^- P$$
$$\hookrightarrow K^- K^o$$

at our momenta (22.4 and 23.9 GeV/c). Our total cross-section measurements in conjunction with the cross-section measurements at different momenta from other experiments[1,2] would permit us to evaluate the momentum dependence of the cross section for the above reaction.

B. The CERN Missing Mass Investigation of the A_2 Meson

The CERN missing mass spectrometer (MMS) group[4] had performed an experiment which investigated the shape of the A_2 meson. The MMS

---

* $t' = t - t_{min}$ and t is the negative four-momentum transfer squared.

had produced A_2 mesons in the reaction

$$\pi^- P \rightarrow X^- + P$$

where the mass spectrum M_X of the meson X^- was determined using a missing mass technique described below. Energy and momentum conservation allow one to express the mass of the meson M_{X^-} in terms of the momentum and energy of the incident particle, the mass of the target particle, and the momentum, energy, and angle of the recoiling proton. The mass of the meson X^- is given by

$$M_X^2 = (E_1+M_2-E_3)^2 - P_1^2 - P_3^2 + 2P_1P_3 \cos\theta.$$

P_1 and E_1 refer to the momentum and energy of the incident pion, θ, P_3, and E_3 to the recoil proton, and M_2 is the mass of the proton, where all quantities are measured in the lab system.

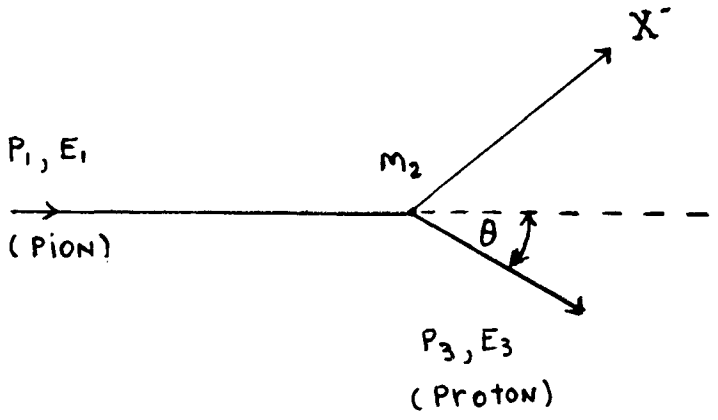

The missing mass technique has several inherent difficulties. Since one never looks at the resonance directly (i.e. the momenta and angles of the decay products of the resonance), one cannot study a

unique decay mode. Furthermore there are, due to the experimental method employed, restrictions on the observed range of the momentum transfer to the recoiling baryon, which depend on the momentum of the incident beam, the mass of the resonance being investigated, and the details of the experimental arrangement.

The results of several of these investigations[4-6] led the CERN collaboration to conclude that the A_2 meson exhibited a split structure which could be well fit by a dipole resonance.[4]

C. Effective Mass of the A_2

We investigated the known[10] decay mode of the A_2^- into a K^oK^- pair

$$A_2^- \rightarrow K^oK^-$$

Our experiment was an effective mass experiment where we determined the mass of the A_2^- from a direct measurement of the momenta and angles of the final decay products of the A_2. Using energy and momentum conservation we can write an expression for the effective mass of the A_2^-.

$$(1)\quad M^2_{A_2^-} = M^2_{K^o} + M^2_{K^-} + 2\sqrt{P^2_{K^o}+M^2_{K^o}}\ \sqrt{P^2_{K^-}+M^2_{K^-}} - 2P_{K^o}\,P_{K^-}\cos\theta_{K^oK^-}$$

where M_{K^o} is the effective mass of the K^o, M_{K^-} is the accepted value of the K^- meson mass (493.71 MeV), $\theta_{K^oK^-}$ is the opening angle between the K^o and K^- in the laboratory frame, and P_{K^o}, P_{K^-} are the laboratory momenta of the K^o and K^- respectively.

D. Definition of a Production Experiment

The experiment we performed was a "production experiment" involving the interaction of one hadron with another. In general the reaction in a production experiment can be written as:

$$M_1 + B \rightarrow X + B' \rightarrow (M_1 + M_2 + \ldots.) + B'$$

where X is a resonance which decays into two or more mesons, and B represents a baryon. This is in contrast to a "formation experiment" where the scattering of one hadron with another temporarily forms an intermediate state which subsequently decays (i.e. $M_1 + B_1 \rightarrow X \rightarrow M_2 + B_2$).

The production experiment we performed involved the investigation of the A_2^- meson produced in the reaction

$$\begin{array}{l} \pi^- P \rightarrow A_2^- P \\ \quad\quad\;\; \hookrightarrow K^- + K^0 \\ \quad\quad\quad\quad\quad\;\; \downarrow \\ \quad\quad\quad\quad\quad\; \pi^+ \pi^- \end{array}$$

at 22.4 and 23.9 GeV/c incident momenta.

E. The Decay Modes of the A_2

Below is a list of the known decay modes of the A_2 (14) including the percentage of the time it decays into each mode. The charge of the decay products would depend on the charge state of the A_2 (+1,0,-1).

Table 1a

A_2	$\rho(770)\pi$	$72.4 \pm 2.1\%$
	$\eta(549)\pi$	$15.3 \pm 1.3\%$
	$\omega(784)\pi\pi$	$7.6 \pm 2.2\%$
	$K\bar{K}$	$4.7 \pm .6\%$
	$\eta'(958)\pi$	$< 1\%$

We note that the dominant decay mode of the A_2 is into the $\rho\pi$ channel. This mode, however, is accompanied by non-resonant $\rho\pi$ events which creates difficulty for an accurate analysis of the mass spectrum and total cross sections. On the other hand, the non-resonant background associated with the $K\bar{K}$ mode is $\lesssim$ 20%, and therefore the analysis would not be subject to many of the difficulties associated with the analysis of data with high backgrounds.

F. The Quantum Numbers of the A_2^- Meson

Since the A_2^- is produced strongly in the reaction $\pi^- P \rightarrow A_2^- P$, its strangeness is zero. We also know that the A_2^- decays strongly into a K^oK^- pair:

$$(1)\ A_2^- \rightarrow K^oK^-$$

Strangeness is an additive quantum number and is conserved in strong interactions. Since the strangeness quantum number of the K^o and K^- are +1 and -1 respectively, we can thus alternatively deduce that the strangeness of the A_2 is zero.

Total isotopic spin is conserved in strong interactions. The total isotopic spin quantum numbers of the K^o and K^- (T_1 and T_2,

respectively) are both 1/2. The total isotopic spin for the right-hand side of reaction (1) can then be $T = |T_1+T_2| \ldots. |T_1-T_2|$; therefore T is either +1 or 0. The z-component of the isotopic spin for the R.H.S. of reaction (1) must be -1. We therefore deduce that the isotopic spin quantum number T for the R.H.S. of reaction (1) must be exactly 1. The conservation of isotopic spin in strong interactions requires that the total isotopic spin quantum number for the A_2 is 1.

Another strong decay of the A_2^- involves its decay into a $\rho^o\pi^-$:

$$(2) \quad A_2^- \rightarrow \rho^o\pi^- \\ \quad\quad\quad\quad\quad\quad \downarrow \\ \quad\quad\quad\quad\quad\quad \pi^+\pi^-$$

where the ρ_o subsequently decays strongly into a $\pi^+\pi^-$ pair. The G-parity of a resonance that decays strongly into an all-pion final state is $G = (-1)^N$ [15] where N is the number of pions. Thus for reaction (2) the G-parity of the R.H.S. is $(-1)^3 = -1$. The conservation of G-parity in strong interactions requires that the G-parity quantum number of the A_2^- be -1.

The G-parity of a resonance which decays strongly can also be expressed as

$$(3) \quad G = (-1)^{\ell+S+T} \quad [14]$$

where ℓ, S and T are the orbital angular momentum, spin and isotopic spin quantum numbers, respectively, for the decay products of the resonance. A knowledge of the G-parity, spin, and isotopic spin of the final state (i.e. K^oK^-) will permit us to determine the orbital angular momentum of the final state to be either even or odd. For reaction (1)

$$A_2^- \rightarrow K^o K^-,$$

in which the K^o and K^- are spin zero mesons, equation (3) becomes

$$(4) \quad G = -1 = (-1)^{\ell} (-1)^o (-1)^1 = (-1)^{\ell+1}$$

thus implying that ℓ is even and that the parity associated with the space coordinates is +1. The intrinsic parity of the R.H.S. in reaction (1) is determined by the intrinsic parity of the K^o and K^-, viz:

$$P_{Intrinsic} = P_{K^o(Intrinsic)} \quad P_{K^-(Intrinsic)} = (-1)(-1) = +1.$$

Thus the overall parity of the $K^o K^-$ state is

$$P_{Total} = P_{Space} \cdot P_{Intrinsic} = (+1)(+1) = +1.$$

The conservation of parity in strong decays requires that the A_2 have positive parity. Since K mesons have zero spin, the spin of the A_2 is equal to the orbital angular momentum of the $K^o K^-$ system. Therefore the spin-parity of the A_2^- can be $J^P = 0^+, 2^+, 4^+, \ldots$ (natural spin parity). Table 1b summarizes the quantum numbers of the A_2 deduced from the above arguments.

Table 1b

Quantum Numbers of the A_2^-

Strangeness	S = 0
Isotopic Spin	T = 1
Third Component of Isotopic Spin	$T_z = -1$
G-Parity	G = -1
Parity	= +1
J^P (one of the following even-even natural spin parity states)	$= 0^+, 2^+, 4^+ \ldots$

G. Decay Angular Distributions in the Gottfried-Jackson Frame

One of the reasons for studying the decay angular distributions of resonances is that it permits us to determine experimentally the probable values of the spin and parity of the decaying particle. In addition, one can obtain evidence for which particles are dominant in the exchange particle models for the reaction. We assume that a resonance "C" is produced in a given interaction with spin quantum number J and subsequently decays into two particles:

$$C \rightarrow M_1 + M_2.$$

After its production the resonance "C", which has a definite spin and parity, is in general in a mixture of magnetic quantum number states. The mixture depends on the spin and parity ($J_e^{P_e}$) of the exchanged particle "e" and is described by the (2J+1) dimensional density matrix of "C" with elements $\rho_{mm'}$, (m,m' correspond to the magnetic quantum numbers of "C" running from -J to J). The decay angular distribution of "C" depends on the mixture of spin states of "C" and, therefore, on the density matrix elements. Thus, by measuring the decay distribution of "C", one can determine spin density matrix elements and deduce the dominant characteristics of the particle(s) exchanged in the reaction producing "C".[16]

The decay angular distributions depend on the reference frame in which we measure the distributions. The most convenient frame to consider the angular correlations of the decay products of a resonance (i.e. the Gottfried-Jackson frame[17]) is in the rest frame of the resonance. For two-body decays, one can define the decay angles (θ,ϕ)

by the direction that one of the decay particles make with some suitable coordinate axes. The choice of axes is suggested by the production mechanism of the interaction. In a peripheral process the interactions are characterized by the tendency of the secondary particles to go off in the forward direction in the center-of-mass system (i.e. small momentum transfer). For peripheral collisions, the production process of the interaction may be described by an exchange of particle(s) in the t-channel. Figure 1a is a Feynman diagram for a process involving the exchange of a particle "e" in the t-channel. In Fig. 1a, "a" represents the incident particle, "b" the target particle, "c" is the resonance we are investigating, and "d" is the recoil particle. In the Gottfried-Jackson frame, the z-axis used for analyzing the decay angular distribution of the resonance is the direction of the incident particle "a" as viewed by an observer in the rest frame of "c". In the rest frame of "c" the momenta of particles "a" and "e" are equal and opposite. This is equivalent to choosing the momentum transfer direction. Figure 1b indicates the momenta of the various particles as viewed by an observer in the rest frame of the resonance "c". In the Gottfried-Jackson frame one defines the normal to the production plane (i.e. the plane formed by "a" and "d") as the y-axis. For two body decays one defines the azimuthal angle ϕ as the angle between the production plane and the plane formed by the z-axis and the momentum vector of one of the decay particles of the resonance, as viewed by an observer in the rest frame of the resonance.

For the reaction

$$\pi^- P \rightarrow A_2^- P$$
$$\downarrow$$
$$K^o K^-$$

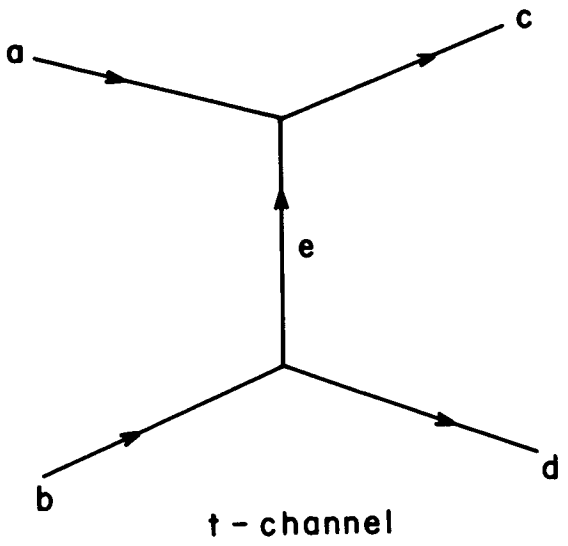

Figure 1a

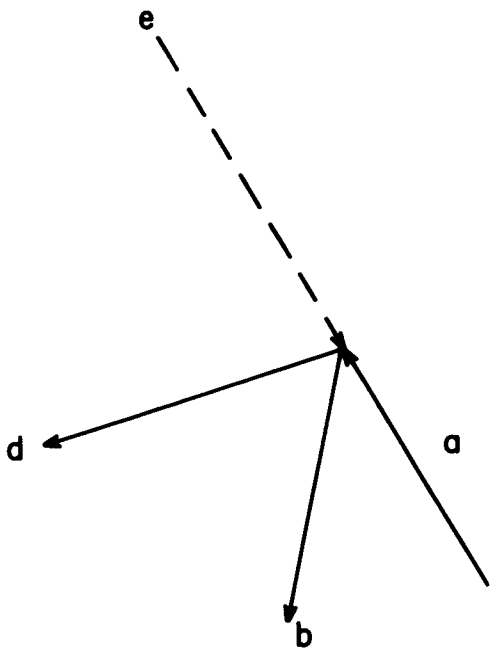

Figure 1b

one defines the z-axis as the direction of the incident pion as seen by an observer in the A_2^- rest frame (see Fig. 1c). The y-axis is defined to be normal to the plane formed by the incident pion and the recoiling proton. The Gottfried-Jackson angles (θ,ϕ) are thus such that the angle θ is the angle between the incoming π^- and the outgoing K^- in the A_2^- rest frame, and ϕ is the angle between the plane of production and the plane formed by the z-axis and the momentum vector of the K^- as viewed by an observer in the rest frame of the A_2^- (see Fig. 1c).

GOTTFRIED - JACKSON ANGLES (θ, ϕ)

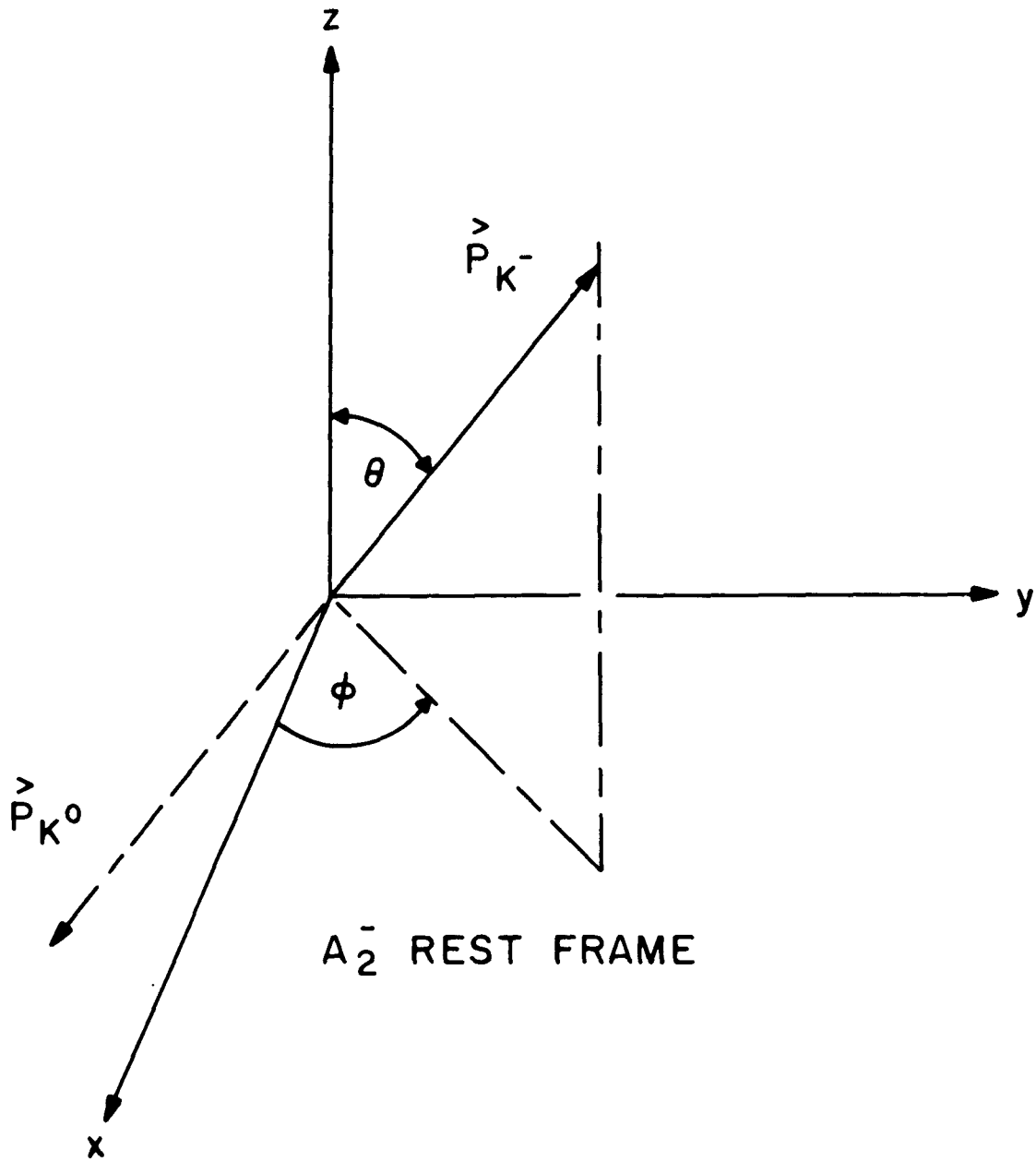

Figure 1c

CHAPTER II

DESCRIPTION OF THE APPARATUS

A. The Incident π^- Beam

The beam used was a 0° secondary beam from the A target station at the AGS. Approximately 3×10^{12} protons at 28.5 GeV/c were extracted each pulse and directed onto a beryllium target .1" high by .2" wide by 4.7" long. The beam system selected and transported particles produced at approximately 23 GeV/c and at 0°. A schematic of the beam system is shown in Fig. 2.

Quadrupoles Q1 through Q5, powered in a triplet configuration, focused the beam onto collimator C5. The collimator C5 defined the momentum acceptance (typically $\pm 1\%$). Dipoles D1 and D2 bent the secondary beam through 2.90° and 2.46° respectively and selected the beam momentum. The primary extracted proton beam, after traversing the target, traversed the same vacuum pipe as the secondary beam and was dumped downstream of D2 in an iron-concrete beam stop. Quadrupoles Q7 through Q10, acting in pairs in a doublet configuration, recaptured the diverging beam and made it parallel in the horizontal plane and slightly divergent in the vertical plane.

Dipoles D3-D5 deflected the beam through 8.7°. Finally, a doublet configuration of quadrupoles Q12 and Q13, having asymmetric focal lengths, focused the beam onto the liquid hydrogen target.

Our negative beam contained a background of approximately .7% kaons, .1% electrons, .07% antiprotons, and approximately 3% muons.[18] Pions

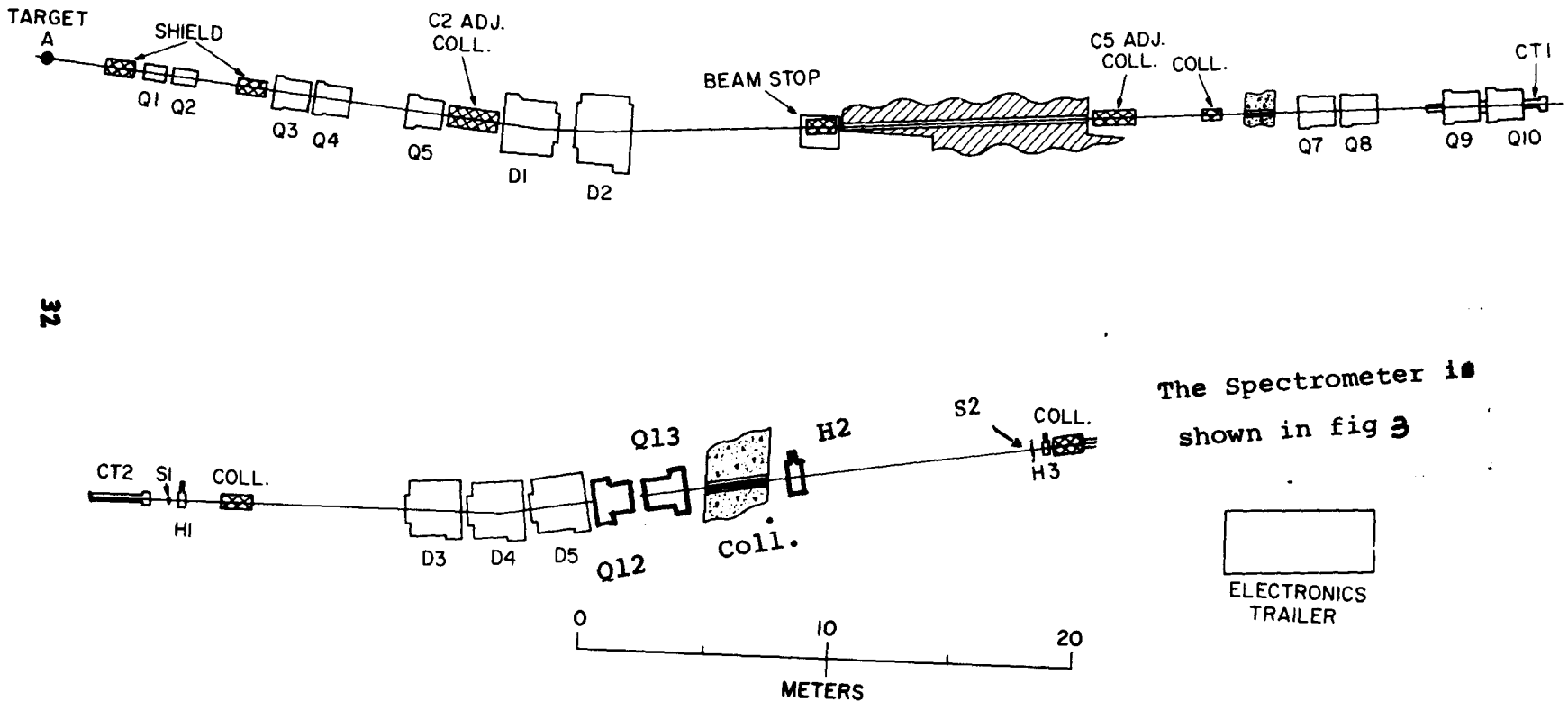

The Spectrometer is shown in fig 3

Figure 2

were detected by two threshold Cerenkov counters (CT1, CT2). Sufficient Cerenkov light for full efficiency on pions was obtained with air at a pressure of 1/2 atm. ABS.

B. Incident Beam Spectrometer

The incident beam spectrometer was set up to measure accurately the position, angle, and momentum of the individual incident particles on the liquid hydrogen target. Each of the three incident beam hodoscopes (H1-H3) consisted of an x-plane and a y-plane of scintillation counters. There were 18 scintillators per plane; of these 16 were in use. Each scintillator element (2-1/2" long x 1/8" wide x 1/16" thick) was epoxy-bonded to a lucite light pipe; the light pipes were in turn epoxy-bonded to RCA 4516 phototubes. Each scintillator assembly was then wrapped in aluminum foil to prevent any light leakage into adjacent counters.

The electronics associated with each of the hodoscopes was located as close as possible to the individual hodoscopes to minimize long cables and time slewing. The phototube signal was first amplified, discriminated (NIM level outputs whenever the input signal was above 200 mv), and then fed into a linear adder matrix circuit. The linear adder output currents were proportional to the particle multiplicity in the hodoscope. This signal was then transmitted to the fast electronics trailer. If a second particle passed through any of the beam hodoscopes within $\pm$20 ns of a beam trigger, the trigger was vetoed. Since only one particle is present in any of the beam hodoscopes during this 40 ns interval, an unambiguous two-digit coding of which

scintillation element fired was possible. The pulses which corresponded to the element the particle traversed was fed into a gated buffer (EG&G units model C142/N) and then to our data-handling system.

Scintillation counter hodoscopes H2 and H3 and the beam spark chamber module were located downstream of all of the beam magnets. We were therefore able to make an accurate determination of the incident direction and position of the beam particle independent of the beam optics. The pattern recognition program reconstructed three-dimensional tracks in the beam chamber. Because of the large lever arm in the incident beam system, the position and angle of the incident beam particles at the target could be accurately measured. The position and angular resolution for beam particles at the target was $\sim$ .010" and $\sim$ .15 mrad respectively.[18]

We electronically determined an incident beam particle to be a pion by requiring a coincidence of the following: scintillation counters S1 and S2, threshold Cerenkov counters CT1 and CT2, hodoscopes H1, H2, and H3, no count in veto counters S and S4. S1 and S2 were scintillation counters each 2-1/2" long x 2-1/2" wide x 1/16" thick located slightly upstream of H1 and H3 respectively (see Fig. 2). S and S4 were annular scintillation counters which were used to veto any stray beam particles. Counter S was 6" high x 6" wide with a 2-1/4" x 2-1/4" hole. It was placed slightly upstream of H1. Counter S4 was 8" high x 14" wide with a 2-1/2" x 2-1/2" hole, and it was placed slightly upstream of the beam spark chamber module. The incident π^- beam was defined to be

$(\pi^-) = (CT1 \cdot CT2) \cdot (S1 \cdot S2) \cdot \overline{S} \cdot \overline{S4} \cdot H1X \cdot H2X \cdot H2Y \cdot H3X \cdot H3Y \cdot (\overline{HM1}$ or $\overline{HM2}$ or $\overline{HM3})$

where HM1, HM2, and HM3 represent the OR of the multiple veto and the annular veto counters for hodoscopes H1, H2, and H3 respectively. We typically had 100,000 incident pions every AGS pulse.

Calibrated Hall probes mounted in dipoles D3-D5 provided a monitor of the magnetic fields of the dipoles. Knowing the position of the incident pion in H2, H3 and the beam chamber, we projected the beam track to the center of dipole D4; this, in conjunction with the position measurement of the pion in H1, enabled us to determine the bending angle and the corresponding momentum of the incident pions. The incident beam system had an estimated momentum resolution $\Delta P/P \sim .1\%$.

C. Target

A top view of our spectrometer is shown in Fig. 3. The target was liquid hydrogen encapsuled in a cylindrical cell two feet long and four inches in diameter. The cylinder had .007" thick mylar walls and was capped with .005" thick mylar domes. Forty layers of aluminized mylar superinsulation, total thickness .010", were used to insulate the cell. The cell was placed in a vacuum box with .014" thick mylar windows in the forward direction and on the sides.

D. Target Veto Counter

The particles emerging from the target were minimum ionizing.* The target veto counter, scintillation counter "A", was placed with its

---

* A 1-GeV/c pion would be considered minimum ionizing.

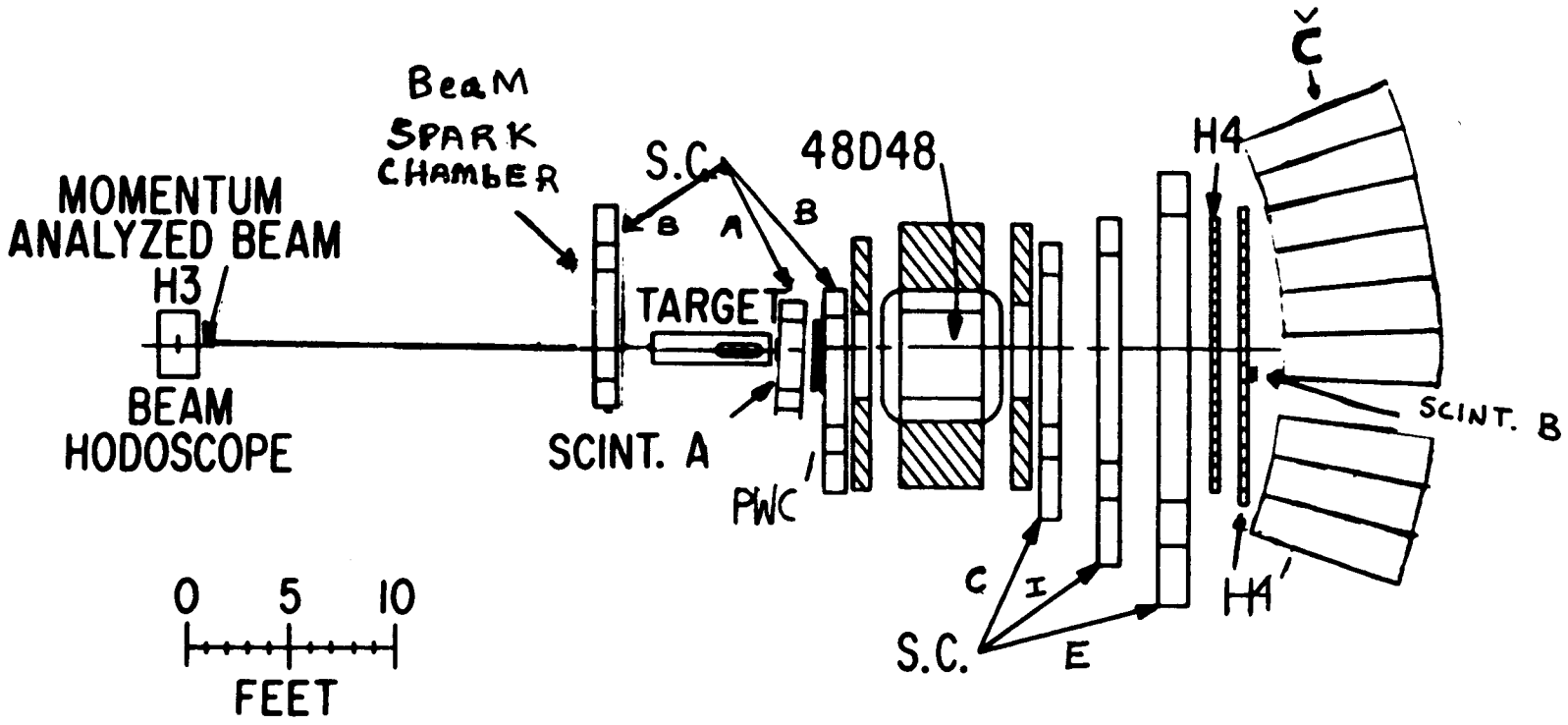
MOMENTUM
ANALYZED BEAM
H3
BEAM
HODOSCOPE
Beam
SPARK
CHAMBER
S.C.
B
A
B
TARGET
SCINT. A
PWC
48D48
H4
Č
SCINT. B
H4'
C
I
E
S.C.
0
5
10
FEET

Figure 3

center at beam height 13.8" downstream of the center of the target. The counter was 4-1/2" high x 8" wide x 1/8" thick. A light pipe and an RCA 8575 phototube were mounted at each end of the counter. The high voltage for each phototube was adjusted to produce equal gain in the tubes. The pulses from each tube were fed into a linear adder. The output of the linear adder was sent to several discriminators. Since the pulse heights associated with the particles traversing the scintillator were proportional to the energy loss in the scintillator, a minimum pulse height could be associated with the multiplicity of charged particles traversing the target veto counter. A set of discriminators could then be set up such that their discrimination levels corresponded to the multiplicities of charged particles traversing the counter. To pick up singles passing through the counter, we required a coincidence between the output of the discriminator corresponding to one or more particles passing through the counter and the output in veto from the discriminator set on doubles.

To assist in the monitoring of the performance of the counter, the signals from the linear adder were also sent to a multichannel pulse height analyzer (PHA). Periodically a pulse height spectrum was generated during the monitoring of the experiment, which displayed peaks corresponding to pulse heights from singles, doubles and triples traversing the counter.

Various tests were performed on the system. A narrow scintillation counter 3" high x 1/2" wide was placed slightly downstream of the target veto counter. A coincidence circuit was set up which required a count

in the target veto counter and in the narrow scintillation counter. We looked for a shift in the peak of the singles pulse height spectrum as a function of the horizontal position of the narrow scintillation counter. No shift was observed. We tested the linearity of the target veto system by attenuating the input signal to the linear adder and observing the shift in the pulse height spectrum. There was a linear relationship between the position of the peak of the pulse height spectrum and the attenuation of the signal.

The pulse heights corresponding to the energy loss of charged particles traversing the scintillator will, for the most part, be confined to a narrow region. However, some of the incident particles will interact in the scintillator and produce delta rays; these events are associated with large energy losses in the scintillator and will appear on the tail of the pulse height spectrum (i.e. Landau tail). In triggering the counter on singles we also required a veto from the discriminator set on doubles. Some events on the Landau tail in the singles spectrum will overlap the pulse height region for doubles. Figure 4 depicts the theoretical, normalized energy loss probability distribution function $\phi(\lambda)$ for a single 10-GeV/c pion, traversing 1.0 cm of Pilot B scintillator.* The function is plotted as a function of the Landau parameter[19] λ. One can make a one-to-one correspondence between the Landau parameter λ and the energy loss Δ in MeV. The most probable energy loss

---

* The actual thickness of the target veto counter was .32 cm. However, the error in the estimate of the misidentification of singles as doubles due to the thickness difference is small compared to the uncertainties involved.

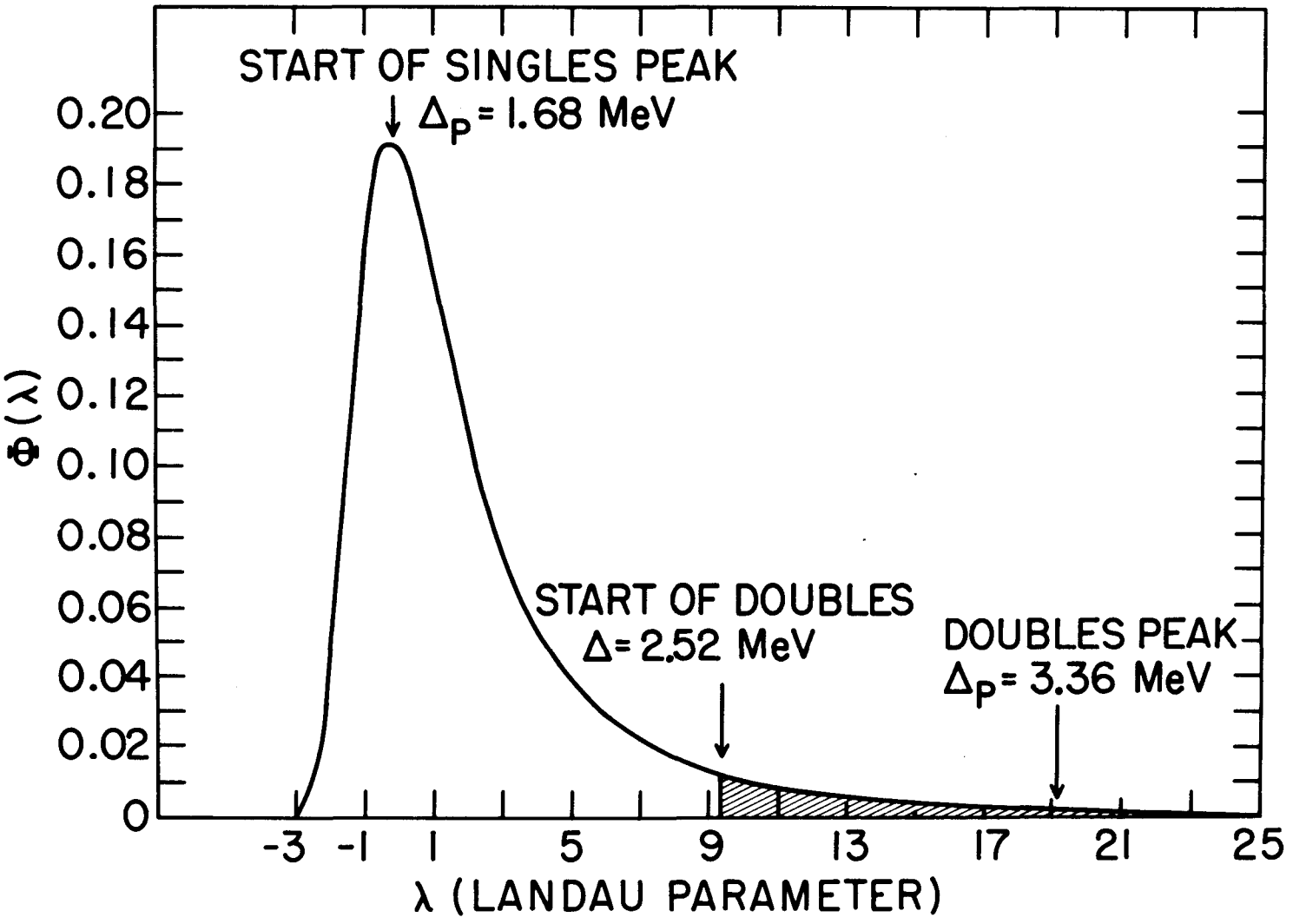
START OF SINGLES PEAK
↓ Δ_p = 1.68 MeV
START OF DOUBLES
Δ = 2.52 MeV
DOUBLES PEAK
Δ_p = 3.36 MeV
Φ(λ)
0.20
0.18
0.16
0.14
0.12
0.10
0.08
0.06
0.04
0.02
0
-3
-1
1
5
9
13
17
21
25
λ (LANDAU PARAMETER)

Figure 4

occurs at Δ_p = 1.68 MeV. The corresponding theoretical peak for doubles is $\Delta_{p(\text{doubles})} = 2\Delta_{p(\text{singles})}$ = 3.36 MeV. Experimentally the discrimination level for the start of the doubles was taken to be halfway between these two peaks at an energy loss Δ = 2.52 MeV.

The shaded area in Fig. 4 represents the theoretically expected fraction of events we would expect to veto, due to misidentifying singles as doubles. We graphically estimate this fraction to be $8 \pm 2\%$ of the real single events. We corrected for this effect in the cross section calculation. (See Chapter VI, Sec. G.)

E. Spectrometer Magnet

The momentum analyzing (48D48) magnet was positioned with its center 115" downstream of the center of the liquid hydrogen target. The magnet gap was 48" wide by 18.44" high by 48" long. The magnet center was displaced 9" in the horizontal direction with respect to the incident beam line to increase our acceptance for events with higher t' (4-momentum transfer squared). Iron shields were placed on the magnet to reduce the fringing field in the region surrounding the magnet. We wanted to be especially careful to avoid fringing fields in the vicinity of the magnetostrictive readout wires which were mounted on adjacent spark chambers. The iron shields helped reduce the fringing fields such that the residual fields on magnetostrictive wires placed adjacent to the shield was less than 10 Gauss. To minimize the multiple scattering from air molecules in the gap of the magnet, a helium container (at 1 atmosphere pressure) with mylar windows was placed in the gap.

Scintillation counters were placed inside the vertical walls and the front face of the magnet. These counters served to reduce our false trigger rate by allowing us to veto any events which had particles hitting the walls of the magnet. These counters are referred to in the text as magnet veto counters (MC).

During the course of the experiment the central magnetic field of our 48D48 magnet was set at 16.7 kg. The magnetic field of the 48D48 magnet was accurately mapped with an automated flip coil apparatus developed at Brookhaven. The point-to-point measuring accuracy of this device was .02%. The absolute calibration of the field was determined with a nuclear magnetic resonance probe. During the course of the experiment a fast-cycling DVM monitored a Hall probe so as to assure the stability of the magnetic field. A multiparameter Fourier fit to the field at various points was made for use in evaluating the field integral $\int B \cdot dL$ as a function of various particle trajectories.

Once the entrance and exit angles of the track and its position in space are determined, an approximate momentum is calculated assuming a uniform magnetic field. Then a more accurate value of the momentum that takes into account the nonuniformity of the magnetic field and the true particle trajector is obtained. This is done by evaluating a polynomial as a function of the entrance positions and angles and the approximate momentum assuming a uniform magnetic field. The 216 coefficients of this correction polynomial have been previously obtained by integrating a series of

trajectories with differing momenta, starting angles and positions through the fitted magnetic field. This technique of evaluating the polynomial gives rapid determination of momenta to about 1/4%.

F. Spark Chamber System

A more detailed description of the construction, electronics and the associated magnetostrictive readouts of the spark chambers has been published.[18] The spark chamber design was motivated by certain basic considerations. We required a system with good spatial resolution, low mass to reduce multiple scattering, and high multiple spark efficiency. The chambers also had to be large enough to encompass the solid angle of the particles exiting from the 48D48 magnet.

All of the spark chambers have the same basic construction. Each sparking gap consists of two G11 epoxy glass frames 1/2" thick, which support the wires (.005" aluminum wires) separated by a 1/2" thick spacer. The chambers were built with the wires (22 wires per inch) running in the same direction on the two planes defining the sparking gap. Adjacent gaps in a module are produced by stacking sets of single gaps together with additional spacers in between. A module of four to seven such gaps is then clamped together and enclosed in a single gas volume with a mylar window at each end.

Each gap had the wire planes running in one of three possible orientations. In order to make an x-measurement the wires ran parallel to the y-axis; to make a y-measurement the wires ran parallel to the x-axis. We also had w-planes (inclined 45° to both x and y) to

resolve ambiguities in track reconstruction. From Fig. 3 one can see that six separate spark chamber modules were incorporated in the spectrometer. The spark chamber module upstream of the target was utilized to improve the position and angle measurements of the particles entering the liquid hydrogen target. The measurements from the two spark chamber modules upstream of the 48D48 magnet and the three spark chamber modules downstream of the magnet permitted a measurement of the momentum and angles of the particles emanating from the target. Table 2 gives some of the dimensions for the appropriate spark chamber modules involved.

To maximize high multiple track efficiencies, the chambers were driven with charge line pulses which delivered a square pulse of about 180 ns duration. The pulsers used hydrogen thyratrons as switches to discharge several 4Ω impedance lines into the spark chambers. The high voltage came from a 20 kv 100 ma power supply. Typically the power supplies were run at 10 kv. One pulser was used to drive all the gaps of a single module.

The gas inside the spark chambers was a mixture of neon and helium with a small amount of ethyl alcohol as a quenching agent (89% neon, 10% helium, 1% ethyl alcohol). The Ne-He gas was purified and recirculated through the spark chamber system. A purifier circulated the gas through the spark chambers, and a prepurifier maintained a vacuum in the spark chamber frames and recovered Ne-He gas that leaked into this cavity. The purifier cleaned contaminants, mostly air, in the return flow from the spark chambers and added the appropriate amount of

Table 2

Spark Chamber Information

Nomen-clature	Y(ft)	X(ft)	Number of X gaps	Number of Y gaps	Number of W gaps
A	1	3	3	3	1
B	2	5	3	3	1
C	3	7	2	2	1
I	3	9.5	2	2	1
E	4	13	2	2	1

ethyl-alcohol to the gas flowing into the chambers. The spark chambers also had dc and pulsed clearing fields applied to eliminate the effects of residual ionizations. The dc clearing field was typically 180v and the pulsed clearing field an additional 600v, both of opposite polarity to the high-voltage pulse.

We employed a magnetostrictive readout system for the spark chambers. When the current associated with a particular spark in the chamber is in the vicinity of a magnetostrictive (Remendur-P) wire it produces a magnetic stress (Joule effect)[20] wave which propagates along the wire with the speed of sound.

Each gap contained planes of wires that were parallel. A magnetostrictive readout wire with one pickup coil was attached to each of the two planes forming a gap. The pickup coils transformed the magnetic stress wave into an electrical pulse. The position of a spark in a particular gap was obtained by averaging the readouts of both planes forming the gap. By reading out both planes and averaging the recorded numbers, one reduces the spark position error due to the uncertainty in the spark angle as a function of track angle. One would also expect that variations in the velocity of sound due to magnetostrictive wire nonuniformities would be reduced. The above technique also cancels the effect of spark generation time.

The sound pulses were detected by a 200 turn pickup coil. The voltage from this coil was linearly amplified and transmitted on a 93Ω cable to the time-to-digital encoding electronics several hundred feet away. If one integrates this voltage pulse, the zero crossing of the

resulting waveform in time corresponds to the peak in the field versus distance of the original fiducial or spark current.[18] The signal was thus fed into an integrating discriminator which delivered a logic output pulse when the pickup coil voltage exceeded a predetermined threshold and the integral of this voltage crossed zero.[18] The system could handle 8 sparks per gap. The logic pulses from the integrating discriminators drove sets of 8 scalers. Each scaler had 15 binary bits plus a flag bit. The first sound pulse (first fiducial) caused all 8 scalers connected to the integrating discriminator to start counting the pulses of a 20 MHZ clock. Subsequent pulses stopped the scalers in sequence, thus leaving binary numbers corresponding to the time difference between the arrival of the first fiducial and the remaining sparks and fiducials. Knowing this time and the distance between any two fiducials we could calculate the spark coordinates.

The spark chambers had a memory time of one microsecond. The dead time associated with the spark chambers was approximately 20 milliseconds. The AGS beam spill was 750 milliseconds long. With the 20-millisecond dead time for each trigger we could still trigger our apparatus many times every beam spill. Typically, during the data-taking phase of the experiment we would trigger approximately 15 times every AGS pulse. Once the system had been triggered, a 20-millisecond dead time was electronically generated so that the apparatus could no longer accept more beam particles or further triggers during this time.

G. Proportional Wire Chamber

A proportional wire chamber (PWC) was placed 31" downstream of scintillation counter "A". The PWC had 320 individual wires; each wire had a separate set of electronics associated with it. The physical separation between individual wires was .10". The signal from an individual wire was fed into a discriminator whose threshold was fixed at 5 mv. The formed pulse, typically 70 ns wide, was then transmitted to a linear adder circuit located in the fast electronics trailer.

We operated the PWC in the "cluster mode" which meant that, if two or more adjacent wires fired, we would consider that to be a single cluster and associated it with one track.

H. Trigger Hodoscopes

Scintillation counter hodoscopes H4 and H4' enabled us to trigger on charged multiparticle final states. Both hodoscopes were located downstream of the last spark chamber. H4 had 63 scintillator elements, each 44.9" high by 2.5" wide by 1/2" thick. At the ends of each scintillator was an RCA 4517 phototube. Immediately downstream of H4 was a second large scintillation counter hodoscope H4' of similar overall size. H4' consisted of 17 scintillation counters, each 54" long by 10" wide by 1/2" thick. By requiring a coincidence between overlapping counters in H4 and H4' we could reduce the number of false triggers caused by neutral particles interacting in the scintillating material of H4. The two phototube signals from the ends of each counter were separately amplified, then OR'd, and then discriminated. The output

stage of the discriminator included a simple summing and coincidence network where the coincidence with H4' was made. The output signals from these discriminators were then fed into a linear ADD circuit. The pulse heights from the outputs of the linear ADD were thus proportional to the number of charged particles traversing the hodoscope. In addition, a second signal is taken from each discriminator and sent to fast gated buffers in the data-handling system so that a record was kept of all counters included in the trigger. The H4 signals were used by the track reconstruction program to determine in-time tracks (i.e. tracks associated with real events that arrived within 40 ns of each other). The Cerenkov counter hodoscope ($\check{C}$) behind the spectrometer was used for other reactions which were being investigated in parallel.

I. Event Trigger

Our trigger topology was motivated by the requirement that we see a clean A_2 signal with minimal background. The topology of the A_2^- decaying into a $K_s^o K^-$ allowed us to do this. A simple requirement of three forward-going charged particles would be dominated by nonresonant $\rho^o\pi^-$ background events. In order to avoid this we incorporated a $1 \rightarrow 3$ trigger, where the $K_s^o K^-$ decay of the A_2^- resulted in one charged particle (K^-) leaving the interaction point plus a neutral vee (the $\pi^+\pi^-$ decay of the K_s^o) materializing downstream. This trigger was accomplished by requiring the following: (1) A single track in the incident beam hodoscope system (π^-); (2) A single charged particle emerging from the hydrogen target as defined by pulse-height analysis on the

target veto counter "A"; (3) Three wire-clusters in a proportional wire chamber (PWC) located 31" downstream of counter "A"; (4) No count in the scintillation counters (MC) lining the 48D48 magnet, thus vetoing events where the particles entered the walls of the magnet; (5) Three or more in-time tracks in the scintillation counter hodoscope H4, and two or more in the scintillation counter hodoscope H4'; (6) No count in a small scintillation counter "B" (5.2 x 5.2 x 1/8") located behind H4'. We used this counter to reduce false triggers in scintillation counter hodoscopes H4 and H4' by vetoing any beam particles which had not interacted.

Symbolically the event trigger required the following coincidences:

$$(\text{event trigger}) = (\pi^-) \cdot A(1) \cdot PWC(\geq 3) \cdot \overline{MC} \cdot H4(\geq 3) \cdot H4'(\geq 2) \cdot \overline{B}$$

where H4' $\geq$ 2 means counts in two or more H4' counters which overlap those counters struck in H4. The resultant trigger rate was approximately one trigger for every 20,000 incident beam particles. During the course of this experiment a total of 1.78 million triggers were taken which satisfied the above event trigger topology. Of the total triggers taken, 3.1% satisfied the topology of one negative prong plus a neutral vee in the mass region 0.485-0.510 GeV coming from a common point in the target.

CHAPTER III

DATA PROCESSING

A. Data Handling

A 4096-word, 108 bits/word buffer memory was used to store data during the AGS pulse. Normally six 18-bit bytes were stacked serially into each 108-bit word. The data were organized into groups, and these groups were separated from each other by special bytes called group words. The group words were characterized by four leading zero bits and contained two numbers, the group number and a word count which showed how far it was from the beginning of the event.

The data associated with a triggered event arrived into the buffer memory in an ordered sequence. The hodoscope bit pattern from scintillation counter hodoscopes H1-H3 and H4 and H4' arrived first. It was in the form of two 108-bit words that contained the outputs of a collection of fast gated buffers (models C142/N built by EG&G). This was followed by the (PWC) data which came in 18-bit bytes. The 18-bit byte of data contained a cluster code, a plane number, and ten bits for encoding the wire number. This was then followed by spark chamber data which was also loaded into 18-bit bytes, the first three bits of which were partial addresses for each spark chamber plane. Each set of seven planes was identified by an accompanying group word. Both the hodoscope data and the spark chamber data had to begin at a 108-bit word boundary sometimes necessitating the use of all zero bytes as fill. A tag bit was used to separate successive events in the buffer.

At the end of the AGS spill, information from scalers and DVMS was put into the buffer in the form of sixteen 108-bit words. These were referred to as a special word subblock as opposed to an event subblock. Each of the buffers was referred to as a block and was labeled with a block number.

B. Data Transmission and On-Line Monitoring

At the end of an AGS cycle the contents of the data handler memory were recorded on magnetic tape and simultaneously transmitted to a PDP-10 computer which was part of the Brookhaven On-Line Data Facility. Each event was recorded as a separate record on the magnetic tape. Only a small sample of events were sent to the on-line computer; approximately 10% of the events were completely reconstructed on-line. This gave us an extremely powerful handle for detecting any serious problems with the apparatus. All the data were completely analyzed off-line with a CDC-6600 at the Brookhaven Central Scientific Computer Facility.

A fast-cycling Hewlett Packard Model 2402 DVM system gave a continuous monitoring of magnet shunt voltages, Hall probe voltages and currents, and power supply voltages. Sixteen such readings were recorded after every AGS spill. The most critical voltages monitored by the DVM were the Hall probe voltages in the dipole magnets. If these readings fluctuated by more than .1%, the computer typed out a corresponding warning and indicated which power supply was malfunctioning.

At the end of each run an on-line printout was obtained. It contained all the relevant information pertaining to that run, including:

(a) run number, date, time of data-taking, etc.

(b) all parameters and constants used in the analysis.

(c) spark chamber and hodoscope efficiencies.

(d) settings on each of the monitored voltages, including maximum and minimum deviations.

(e) a profile of the incident screen hodoscopes (H1-H3) and H4 and H4'.

(f) number and types of triggers taken.

(g) all relevant kinematic quantities were binned, such as: momentum of the beam, effective mass without any kinematic cuts, effective mass with kinematic cuts, missing mass spectra, etc.

(h) final readings of all scalers.

C. Pattern Recognition and Event Analysis

Before an event could be considered a candidate for analysis, we required that there be one and only one count in each of the x planes of scintillation counter hodoscopes (H1-H3). A major task of the analysis program was to convert spark coordinates into 3-dimensional track segments. The pattern recognition subroutine BEADS treated each two-dimensional "view" of the event separately and looked for straight line segments containing at least four sparks in the x and y views of both the downstream and upstream arms of the spectrometer. The search for these line segments was initiated by forming "roads" using a pair of sparks from chambers in two different modules. If more than one spark in a

gap was found on the road, the spark closest to the center of the road was picked. If four or more sparks were found to lie in the road, a least-squares fit to the straight line segment was performed, and an rms error of the fit was computed. We considered a combination of sparks to form a track if the rms error fell below .035". If the error was larger than the preset limit, then one spark at a time was thrown away until either the error fell below the limit or the number of remaining sparks was less than four. Tracks were first reconstructed in the x-view (xz plane) behind the 48D48 magnet. In this view we checked to see whether the counter in scintillation counter hodoscope H4, which this track intersects, was triggered (i.e. in-time). The tracks in the other three views (x and y before the magnet, y after the magnet) were similarly reconstructed only if enough in-time tracks that satisfy the trigger requirement were present in the back x-view. In the case of the A_2 trigger we required at least three in-time tracks in H4.

Once we had the straight line segments in all the views, subroutine THREED tried with the aid of the W gaps (wires running 45° to both the x and y wires) to reconstruct three-dimensional tracks in front of and behind the 48D48 magnet. A weight was calculated for each xy track combination depending upon the closest distance between the projected xy intersection and the nearest w-spark. Only the combinations which have a weight above a preset limit are accepted.

Subroutine (MOM) connected the three-dimensional track segments in front of and behind the 48D48 magnet. This was done by requiring that the three-dimensional tracks, when projected back to the magnet center along the particle trajectory, have some preset minimum distance

of closest approach ($\sim$ 2"). If the above criteria were satisfied the momentum was calculated using the method outlined earlier in the section on the spectrometer magnet. The sign associated with the track was determined by the direction of curvature of the associated particle in the magnetic field. After the momentum and angles of the particles were determined, various kinematic routines (DOVKIN and DOVDEK) calculated relevant quantities like effective mass, missing mass, decay angles, etc. The program also checked for the interaction point to be in the target, and that all decay volume cuts be satisfied.

D. Data Reduction

Once an event corresponding to a particular trigger satisfying certain topological and kinematic cuts was found, the relevant information corresponding to that event was written onto a summary tape. In the case of the A_2^- trigger an event was written onto the data summary tape if the event fitted the topology of one negative prong plus a neutral vee in the mass region .485-.510 GeV (assuming that the neutral vee decayed into a $\pi^+\pi^-$) coming from a common point in the target. The summary tapes contained the important kinematic quantities such as the target interaction points, momenta and momenta components, decay points of the neutral vees, a point and direction cosines of a particular track, etc. Once the data were reduced to summary tape form, all subsequent analysis was performed by programs written to analyze these summary tapes. Once all the topological and kinematic cuts were applied, the data could be fit onto two magnetic tapes. One could then analyze the data under different hypotheses in about 1/2 hour of real time on the PDP-10.

CHAPTER IV

RESOLUTIONS

A. The Effect of Resolution on Fine Structure

We were interested in studying the shape of the A_2 mass spectrum, and in particular to investigate the possibility that the mass spectrum exhibits a split. The effective mass resolution would be crucial in detecting any structure (if it exists) in the mass spectrum; since the effect of poor mass resolution is to smear out fine structure.

If a signal $I_o(E)$ is detected through an instrument whose resolution function may be represented by a Gaussian:

$$D(E) = \frac{e^{-E^2/2\sigma^2}}{\sqrt{2\pi}\,\sigma}$$

(where σ is the resolution), then the observed signal is the convolution of the two functions:[21]

$$I(E) = \int I_o(E')\, D(E - E')\, dE'$$

We attempted to fit our mass spectra with the CERN dipole form described in Chapter V. In performing the fits we folded into the functional form of the dipole, a Gaussian resolution function with a σ corresponding to our A_2 effective mass resolution (Section G). The factors that determine the effective mass resolution σ will be described below.

B. Position Resolution of Spark Chambers

The spark chamber system incorporated parallel .005" aluminum wires with a spacing of 22 wires to the inch. The observed position

resolution of the chambers was approximately .010" rms. This excellent position resolution was possible because of the following factors:

a) The use of zero crossing integrating discriminators which enabled us to locate the center of a readout pulse with high precision.

b) Reading out both planes of wires forming a gap.

c) Precise alignment of spark chambers.

Fig. 5 indicates the frequencies of deviations from a straight line fit as determined by $\sqrt{\frac{\Sigma_i (x_i - X_i)^2}{N - 2}}$ where N is the number of sparks along the track, x_i are the measured points and X_i are the results of the fit. The most common deviation from a straight line is in the .006" to .008" bin. The tail of the distribution is due to nearby beam tracks, fake fits, etc.

A combination of sparks was accepted as a track if the rms error of the fit was less than .035". If the error was larger than this limit, then one spark at a time was thrown away until either the error fell below this limit or the number of remaining sparks was less than four.

The position resolution of the chambers ($\sim$.010" rms) required that the spark chambers be accurately aligned, and that the spatial separation of the two fiducials on each spark chamber plane be accurately known. Special alignment runs with the 48D48 magnet off allowed us to measure the x and y coordinates of the chambers to an accuracy of $\pm$ .004". The spatial separation of the two fiducials on each spark chamber plane were measured in advance to $\sim$.004". The z positions of the chambers were obtained by optical surveying. We

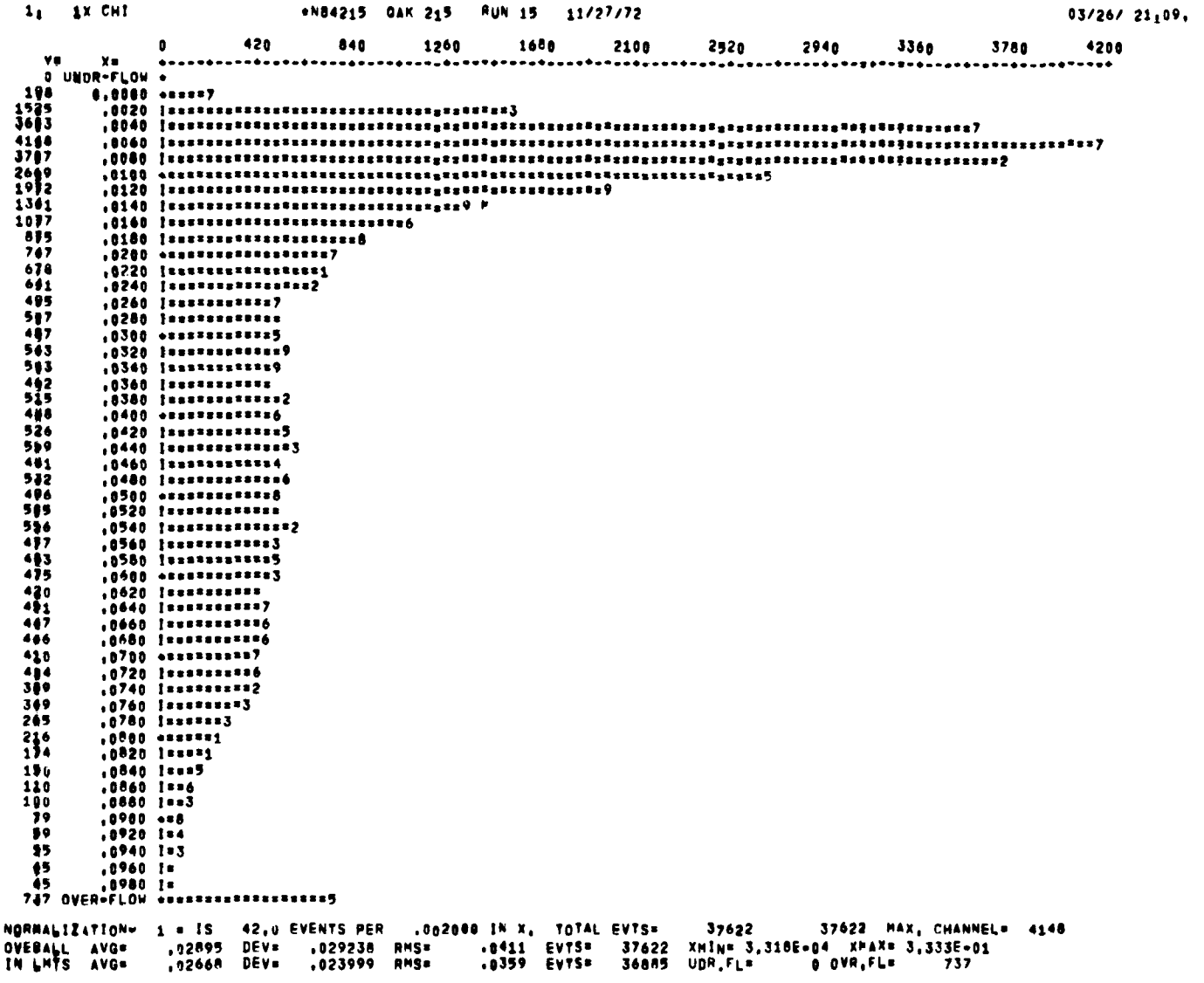
1X CHI *N84215 OAK 215 RUN 15 11/27/72 03/26/ 21.09.
0 420 840 1260 1680 2100 2520 2940 3360 3780 4200
Y= X=
0 UNDR-FLOW
198 0.0000
1525 .0020
3683 .0040
4188 .0060
3787 .0080
2699 .0100
1972 .0120
1361 .0140
1077 .0160
875 .0180
707 .0200
678 .0220
691 .0240
495 .0260
587 .0280
487 .0300
563 .0320
503 .0340
492 .0360
515 .0380
488 .0400
526 .0420
589 .0440
481 .0460
532 .0480
496 .0500
585 .0520
536 .0540
477 .0560
483 .0580
475 .0600
420 .0620
491 .0640
467 .0660
486 .0680
410 .0700
484 .0720
389 .0740
369 .0760
265 .0780
216 .0800
174 .0820
190 .0840
120 .0860
100 .0880
79 .0900
89 .0920
95 .0940
65 .0960
45 .0980
747 OVER-FLOW
NORMALIZATION= 1 = IS 42.0 EVENTS PER .002000 IN X, TOTAL EVTS= 37622 37622 MAX, CHANNEL= 4148
OVERALL AVG= .02895 DEV= .029238 RMS= .0411 EVTS= 37622 XMIN= 3.318E-04 XMAX= 3.333E-01
IN LMTS AVG= .02668 DEV= .023999 RMS= .0359 EVTS= 36885 UDR.FL= 0 OVR.FL= 737

Figure 5

also adjusted the position of the chambers on the AGS floor to eliminate any roll, pitch and yaw. We note that the position resolution of the downstream arm of the forward spectrometer is somewhat worse than the upstream arm. This may be attributable to the larger chambers (I and E) having a tendency to warp. The position resolution of the downstream chambers was approximately .012" rms.

C. Multiple Scattering

We can estimate the effect of multiple scattering on our angular resolution knowing the amount and the distribution of the scattering material present. For the $\pi^+\pi^-$ decay products of the K_s^o, the calculation is based on the assumption that the charged particles originate downstream of the target veto counter and upstream of the first spark chamber. For a K^- associated with the decay of an A_2^- in the target we include in our calculation the effect of multiple scattering in the target and in the target veto counter.

Tables 4a, 4b indicate the type and amount of material present in both the upstream and downstream arm of the forward spectrometer. We neglect any multiple scattering downstream of the first x-gap in the E spark chamber since the angle measurement has already been made and any further multiple scattering downstream will have a negligible effect on the angular resolution.

We calculated the equivalent amount of aluminum present for the aluminum wires in our spark chambers. Each wire was .005" thick with a spacing of 22/inch. The amount of material available for scattering is approximately (22)(.005)/1 inch or $\sim$1/10 of what we would have if we had a plane sheet of aluminum.

Table 4a

Material in Upstream Arm of Forward Spectrometer

Material	ρ (gm/cm^3)	X (CM)	L (gm/cm^2)	$L_{rad}^{(14)}$ (gm/cm^2)	$R=L/L_{rad}$
Stainless Steel*	7.87	.0035	.027	13.9	.0020
Aluminum	2.70	.0350	.094	24.3	.0038
Ne-He	.001205	84.90	.102	36.5	.0028
Aclar	1.38	.030	.041	39.6	.0010
		$\Sigma R = .0096$			

Table 4b

Material in Downstream Arm of Forward Spectrometer until End of First x-Gap in Spark Chamber Module (E)

Material	ρ (gm/cm^3)	X (CM)	L (gm/cm^2)	L_{rad} (gm/cm^2)	$R=L/L_{rad}$
Helium	.000178	121.92	.0217	85.4	.0002
Air	.001205	272.46	.3283	36.5	.0089
Ne-He	.001205	43.92	.053	36.5	.0014
Aclar	1.38	.0355	.049	39.6	.0012
Aluminum	2.70	.0279	.075	24.3	.0031
		$\Sigma R = .014$			

* The PWC cathodes consisted of two sheets, each of .0007" thick stainless steel.

If a charged particle traverses a block of thickness d which has a uniform distribution of material of total radiation length L, then the rms error in the x-position is given by[14]

$$\Delta X_{rms} = \frac{d}{\sqrt{3}} \frac{.015}{P} \sqrt{\frac{L}{L_{Rad}}}$$

The error in the measurement of the incident angle will be

$$\sigma(\theta)_{rms} = \frac{\Delta X_{rms}}{d} = \frac{.015}{P\sqrt{3}} \sqrt{\frac{L}{L_{Rad}}}$$

where P is the momentum of the incident particle, L is the thickness of the scatter in gM/cM^2, L_{Rad} is a radiation length of material in gM/cM^2 and $\sigma(\theta)_{rms}$ is the error in the measured angle due to multiple scattering.

From the above we calculate the contribution to the angular resolution due to multiple scattering in the front and back legs of the spectrometer.

$$\sigma^2_{rms}(\theta_{xz})_{(front)} = \left[\frac{.015}{P\sqrt{3}} \sqrt{\Sigma R_{front}}\right]^2 = \frac{.72}{P^2}$$

and

$$\sigma^2_{rms}(\theta_{xz})_{(back)} = \left[\frac{.015}{P\sqrt{3}} \sqrt{\Sigma R_{back}}\right]^2 = \frac{1.05}{P^2}$$

where ΣR_{front} and ΣR_{back} are the fractions of a radiation length of material in the front and back legs of the spectrometer respectively.

D. Angular Resolution

The angular resolution of the upstream arm of the forward spectrometer is determined by the accuracy in the measurement of the angles that the particles emerging from the target make with some fixed axis. The angular resolution in the xz plane of the forward spectrometer was measured with the 48D48 magnet turned off using beam particles at various momenta. We calculated the difference in the projected angle in the xz plane measured by the front leg and back leg of the spectrometer.

$$(1) \qquad \theta_{xz(\text{measured})} = \theta_{xz(\text{back})} - \theta_{xz(\text{front})}$$

Figure 6 indicates the number of counts versus $\theta_{xz(\text{measured})}$ as defined above for 24 GeV/c pions.

We folded in the errors in quadrature thus:

$$(2) \qquad \underset{\downarrow}{\sigma^2_{rms}(\theta_{xz})} = \underset{\downarrow}{\sigma^2_{rms}(\theta_{xz})_{back}} + \underset{\downarrow}{\sigma^2_{rms}(\theta_{xz})_{front}}$$

measured calculated calculated

The $\theta_{xz(\text{measured})}$ distribution is not exactly Gaussian which can be partially attributed to a small fraction of the total events undergoing large-angle Coulomb scattering. We fitted the distribution with a functional form consisting of the sum of two Gaussians, and then calculated a root mean square deviation for the distribution.

We calculated $\sigma_{rms}(\theta_{xz})$ for the front and back leg (upstream and downstream of the 48D48 magnet, respectively) separately, by inserting the appropriate contributions to the angular resolutions for each leg due to: a) multiple scattering and b) finite position resolution of the spark chambers. We then added these contributions in quadrature:

$$(3) \qquad \sigma(\theta_{xz}) = \sqrt{\frac{A}{P^2} + B}$$

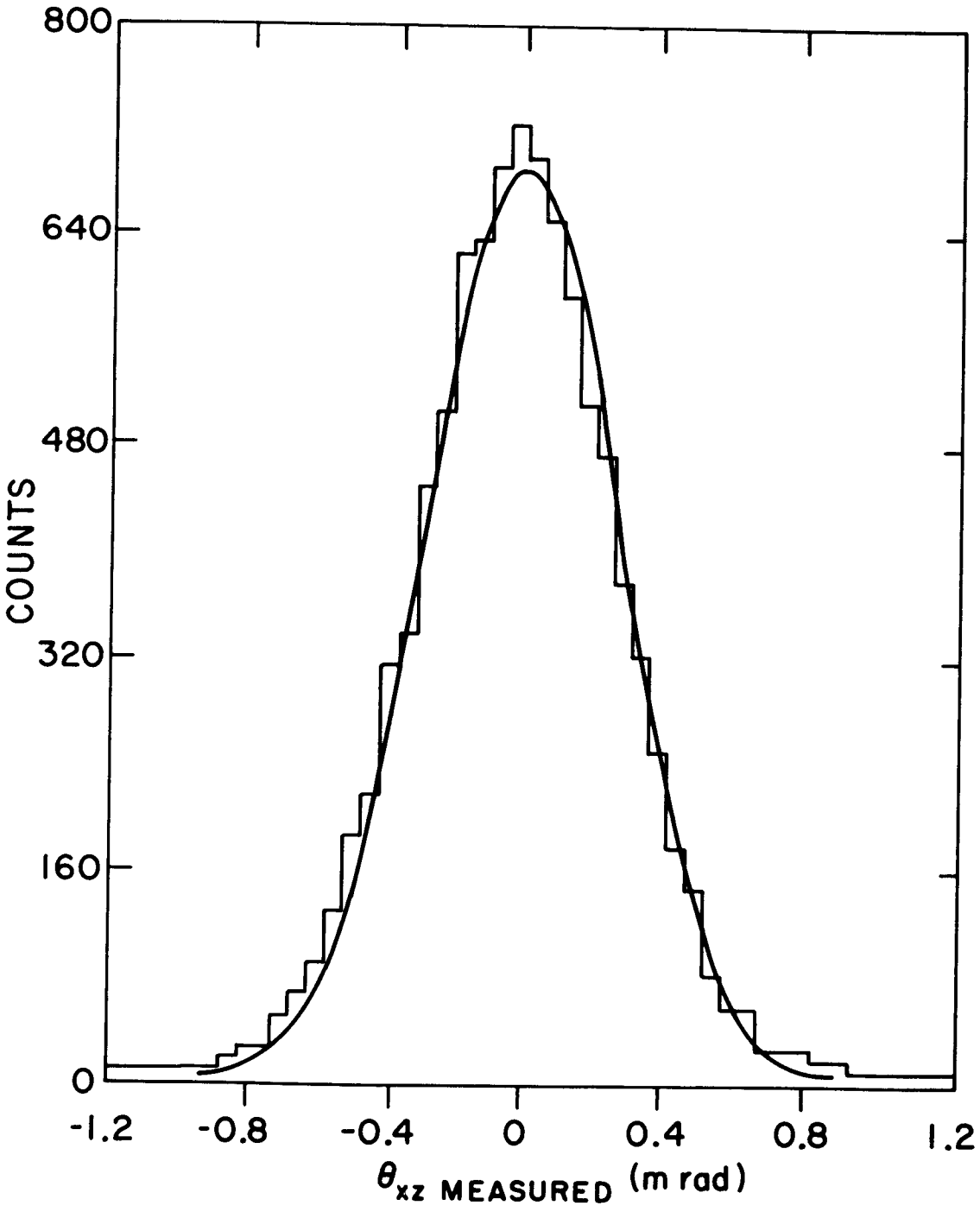
800
640
480
320
160
0
COUNTS
-1.2
-0.8
-0.4
0
0.4
0.8
1.2
θxz MEASURED (m rad)

Figure 6

where the parameter A is related to the contribution from multiple scattering (see section C on multiple scattering), and the parameter B is related to the finite position resolution of the spark chambers, the length of the lever arm (i.e. distance between initial and final position measurements), and the number of position measurements (see Appendix B). The results of a calculation for the above parameters for the front and back leg are:

$$(4) \qquad \sigma_{front}(\theta_{xz}) = \sqrt{\frac{.72}{P^2} + .077} \qquad \text{(calculated)}$$

$$(5) \qquad \sigma_{back}(\theta_{xz}) = \sqrt{\frac{1.05}{P^2} + .012} \qquad \text{(calculated)}$$

It is clear from the above forms that at high momentum the angular resolution is dominated by the position resolution component, and that at low momentum the dominant term is multiple scattering. Figure 7 is a graph of the calculated rms angular resolution in the xz plane of the front leg of the spectrometer.

Table 4c lists the angular resolutions both measured and calculated as a function of momenta. From Table 4c one can see that there is excellent agreement between the rms measured value for the difference in the angles between the front and back leg, and the calculated rms value. This excellent agreement prompts us to believe that we understand the contributions to the angular resolution from multiple scattering and finite position resolution in both the front and back leg.

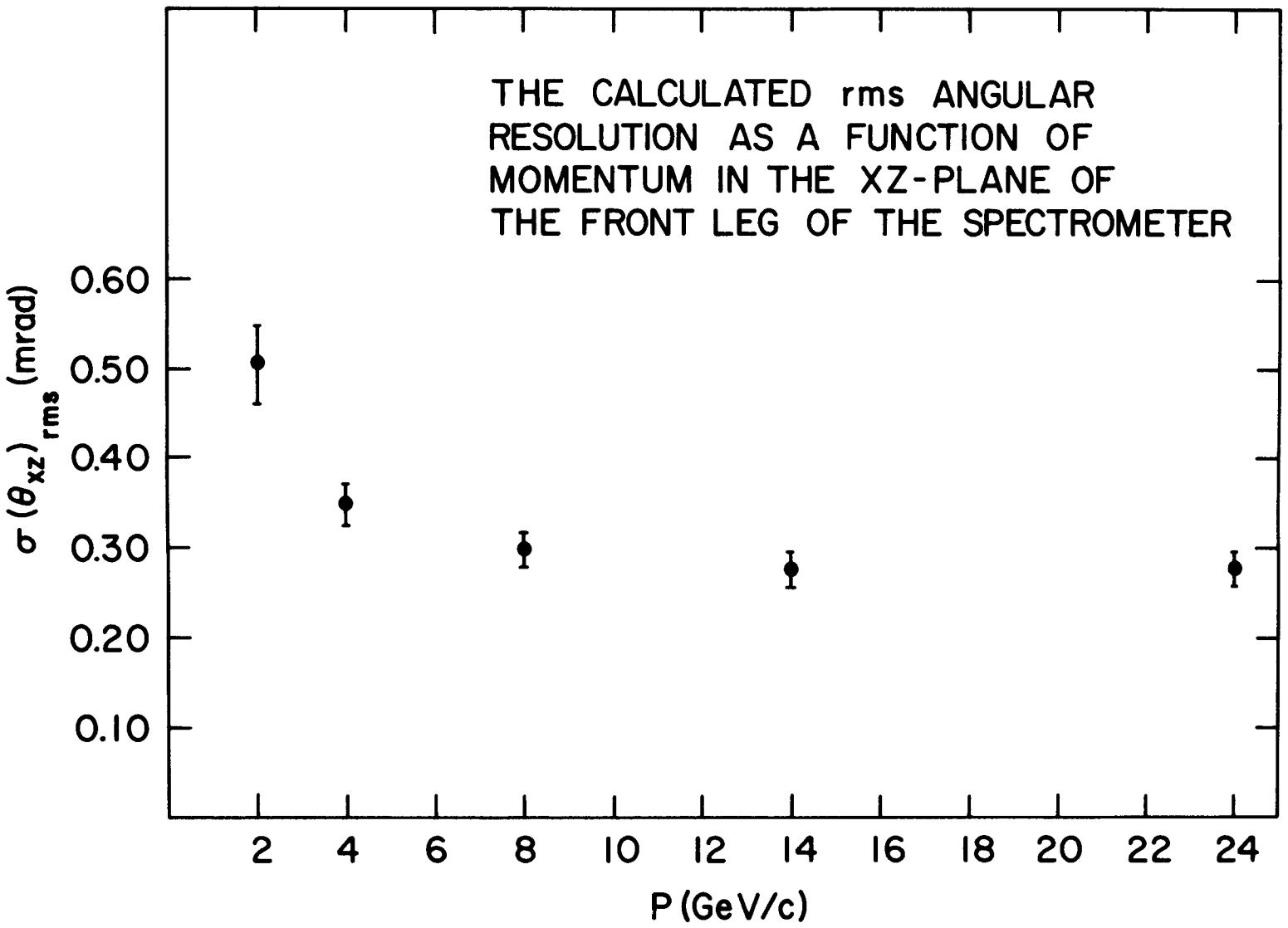
THE CALCULATED rms ANGULAR
RESOLUTION AS A FUNCTION OF
MOMENTUM IN THE XZ-PLANE OF
THE FRONT LEG OF THE SPECTROMETER
σ (θxz) rms (mrad)
0.60
0.50
0.40
0.30
0.20
0.10
2
4
6
8
10
12
14
16
18
20
22
24
P (GeV/c)

Figure 7

Table 4c

Angular Resolution Calculations

P (GeV/c)	$\sigma_{rms}(\theta_{xz})_{back}$ calculated (mrad)	$\sigma_{rms}(\theta_{xz})_{front}$ calculated (mrad)	$\sigma_{rms}(\theta_{xz})$ measured (mrad)	$\sigma_{rms}(\theta_{xz}) = \sqrt{\sigma^2_{rms}(\theta_{xz})_{back} + \sigma^2_{rms}(\theta_{xz})_{front}}$ calculated (mrad)
2	.52 ± .04	.51 ± .04	.71 ± .03	.73 ± .05
4	.28 ± .03	.35 ± .02	.42 ± .01	.44 ± .04
8	.17 ± .02	.30 ± .02	.33 ± .01	.34 ± .03
14	.13 ± .02	.28 ± .02	.31 ± .01	.31 ± .03
24	.11 ± .01	.28 ± .02	.29 ± .01	.30 ± .02

The errors in the calculated values for $\sigma(\theta_{xz})$ reflect the uncertainties in the calculated multiple scattering and position resolution contributions to the angular resolutions, whereas the error on $\sigma_{rms}(\theta_{xz})_{measured}$ is due to finite statistics.

E. Momentum Resolution

We measured the momentum resolution of the forward* spectrometer using beam particles at various momenta and compared the momentum measured by the incident beam spectrometer with that of the forward spectrometer. We measured a quantity

$$\Delta P = P \text{ (forward spectrometer)} - P \text{ (beam spectrometer)}.$$

(Figure 8 indicates the number of events versus ΔP for 14-GeV/c pions.) Folding in the errors in quadrature we get

$$\sigma^2_{(\Delta P)_{(\text{measured})}} = \sigma^2(P)_{\text{forward spectrometer}} + \sigma^2(P)_{\text{beam}}.$$

We unfolded the contribution to the above measured quantity due to the momentum resolution of the incident beam spectrometer.

Due to the large lever arms in the incident beam system (see Fig. 2) the main contributions to the beam momentum resolution arose from the uncertainty in the incident and exit angles through dipoles D3-D5 (see Chapter II, Sec. B) from multiple scattering of pions between H1 and D4, and between H2 and the beam spark chamber. We calculated the rms error in the bending angle $\theta_{\text{bend}} = \theta_{\text{exit}} + \theta_{\text{incident}}$ due to: (a) finite position resolution in H1, H2, H3 (i.e. $\sim$ .020") and the beam spark chamber $\sim$ .010", and (b) multiple scattering in the beam system.

Folding in the errors in quadrature we get

$$\sigma_{\text{rms}}(\theta_{\text{bend}}) = \sqrt{\frac{2.25}{p^2} + .022} \quad \text{(mrad)}.$$

The momentum resolution $\sigma_{\text{beam}}(P)$ is related to the uncertainty in the bending angle by

---

* The forward spectrometer is the particle momentum measuring spectrometer downstream of the hydrogen target.

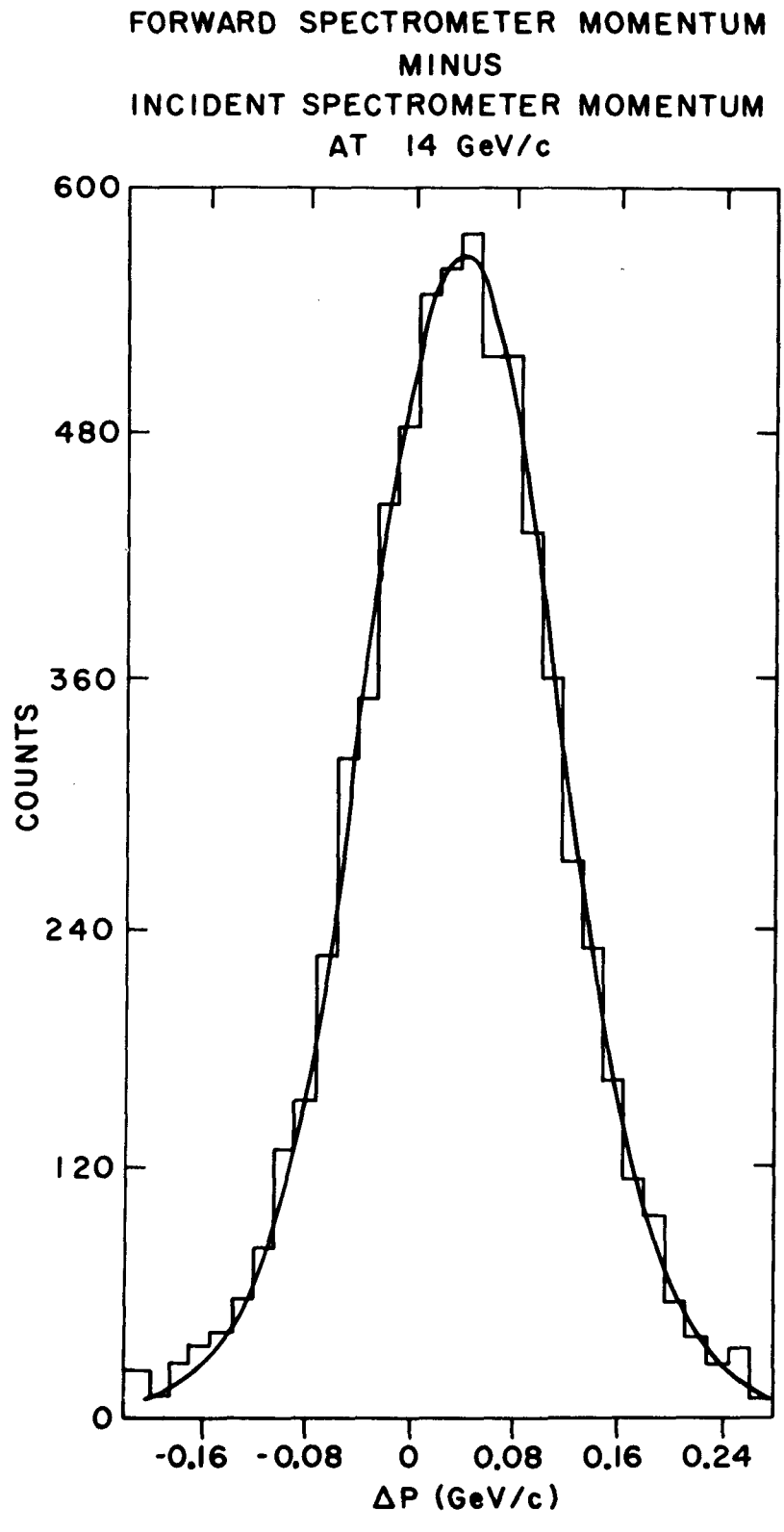
FORWARD SPECTROMETER MOMENTUM
MINUS
INCIDENT SPECTROMETER MOMENTUM
AT 14 GeV/c
600
480
360
240
120
0
COUNTS
-0.16
-0.08
0
0.08
0.16
0.24
ΔP (GeV/c)

Figure 8

$$\frac{\sigma_{beam}(P)}{P} \propto \frac{\sigma(\theta_{bend})}{\theta_{bend}}$$

where $\theta_B = 8.7° = 151.38$ mrad. We can therefore unfold the contribution to the measured momentum resolution due to the incident beam momentum resolution.

Table 4d is a list of $\sigma_{rms}(P)_{(beam)}$, $\sigma_{rms}(\Delta P)_{(measured)}$, $\sigma_{rms}(P)_{forward\ spectrometer}$ and $\sigma_{rms}(P)_{forward\ spectrometer}/P$ in %, as a function of momentum. Figure 9 is a plot of

$$\frac{\sigma_{rms}(P)_{forward\ spectrometer}}{P}$$

in % as a function of momentum.

F. The K^o_s Effective Mass Resolution

The K^o_s decays weakly into 2 π's with essentially no inherent width. We can thus check the accuracy of our resolution calculations by comparing the calculated K^o_s effective mass resolution with the experimentally determined resolution.

Figure 10 shows the effective 2π mass spectrum in the K^o mass region for the reaction $\pi^- P \rightarrow K^o_s K^- + P$ where $1.1 < M(K^o_s K^-) < 1.5$ GeV. Due to multiple scattering, production of delta rays, merging tracks in the spark chambers and decays of the pions in the spectrometer, the overall resolution function is poorly fitted by a single Gaussian. The data was well fitted ($x^2 = 49.9$ for 44 D.O.F.) by using a functional form consisting of the sum of two Gaussian terms plus a small linear background. The fitted widths of the Gaussian parameters were $2.18 \pm .16$ and $4.27 \pm .21$ MeV with the wider Gaussian having 58 ± 18% of the amplitude of the narrower. The linear background comprised 5% of the total

Table 4d

P(GeV/c)	$\sigma_{rms}(\Delta P)$ (MeV) (measured)*	$\sigma_{rms(Beam)}$ MeV†	$\sigma_{rms}(P)$ (MeV) (forward spectrometer)	$\sigma_{rms}(P)/P$ % (forward spectrometer)
2	16.3 ± .6	10.1 ± 1.0	12.9 ± 2.0	.65 ± .10
4	20.4 ± .2	10.7 ± 1.0	17.4 ± 2.0	.44 ± .05
8	36.9 ± 1.5	12.6 ± 1.5	34.7 ± 1.5	.43 ± .02
14	81.4 ± .7	16.9 ± 1.5	79.6 ± 1.0	.57 ± .01
24	224 ± 2	25.5 ± 2.0	222 ± 1.0	.93 ± .01

* Errors due to statistics

† Errors due to uncertainty in the contribution to $\sigma_{rms(Beam)}$ from multiple scattering and position resolution in incident beam system.

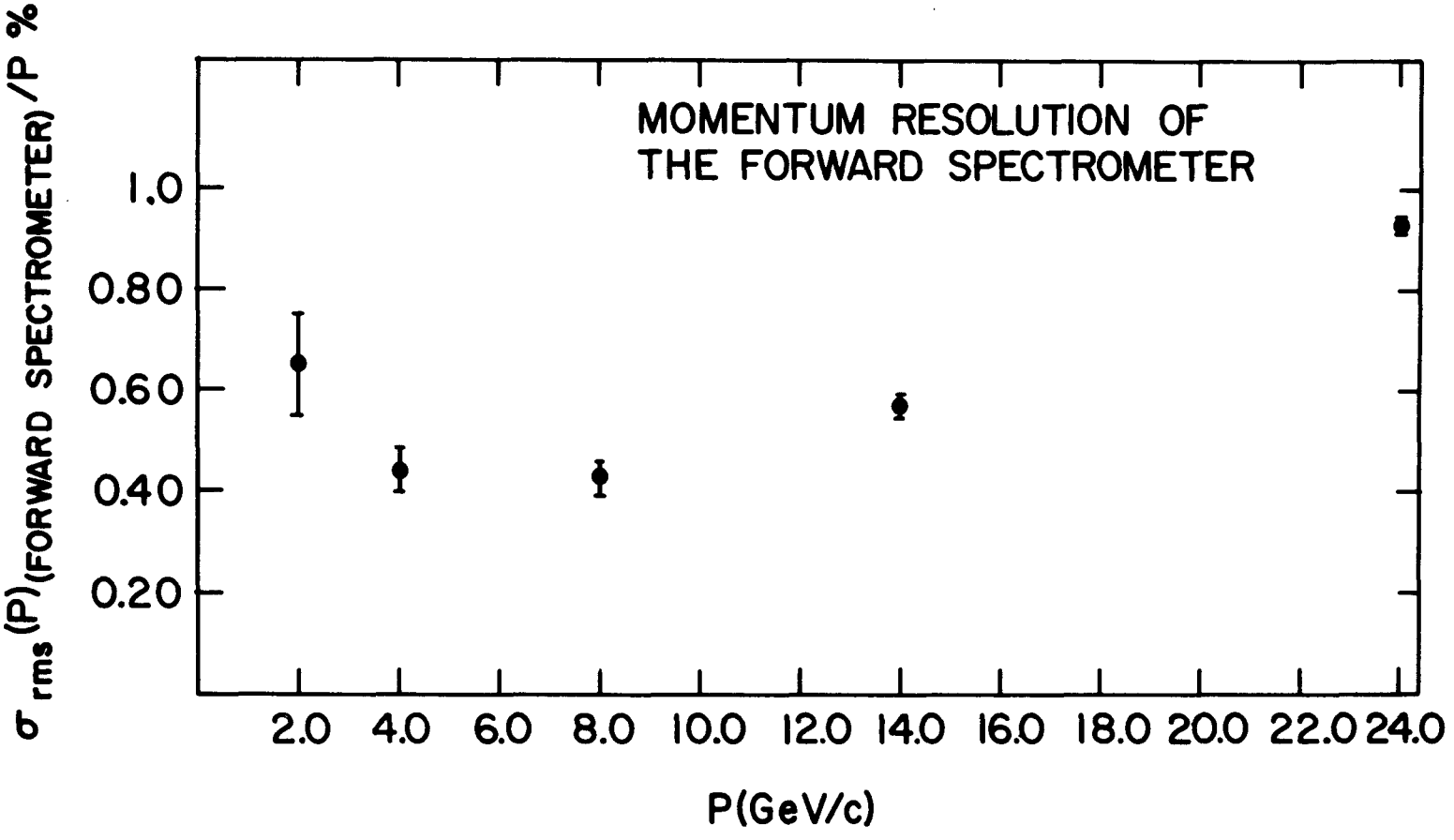
MOMENTUM RESOLUTION OF
THE FORWARD SPECTROMETER
$\sigma_{rms}(P)_{(FORWARD\ SPECTROMETER)}/P$ %
1.0
0.80
0.60
0.40
0.20
2.0
4.0
6.0
8.0
10.0
12.0
14.0
16.0
18.0
20.0
22.0
24.0
P(GeV/c)

Figure 9

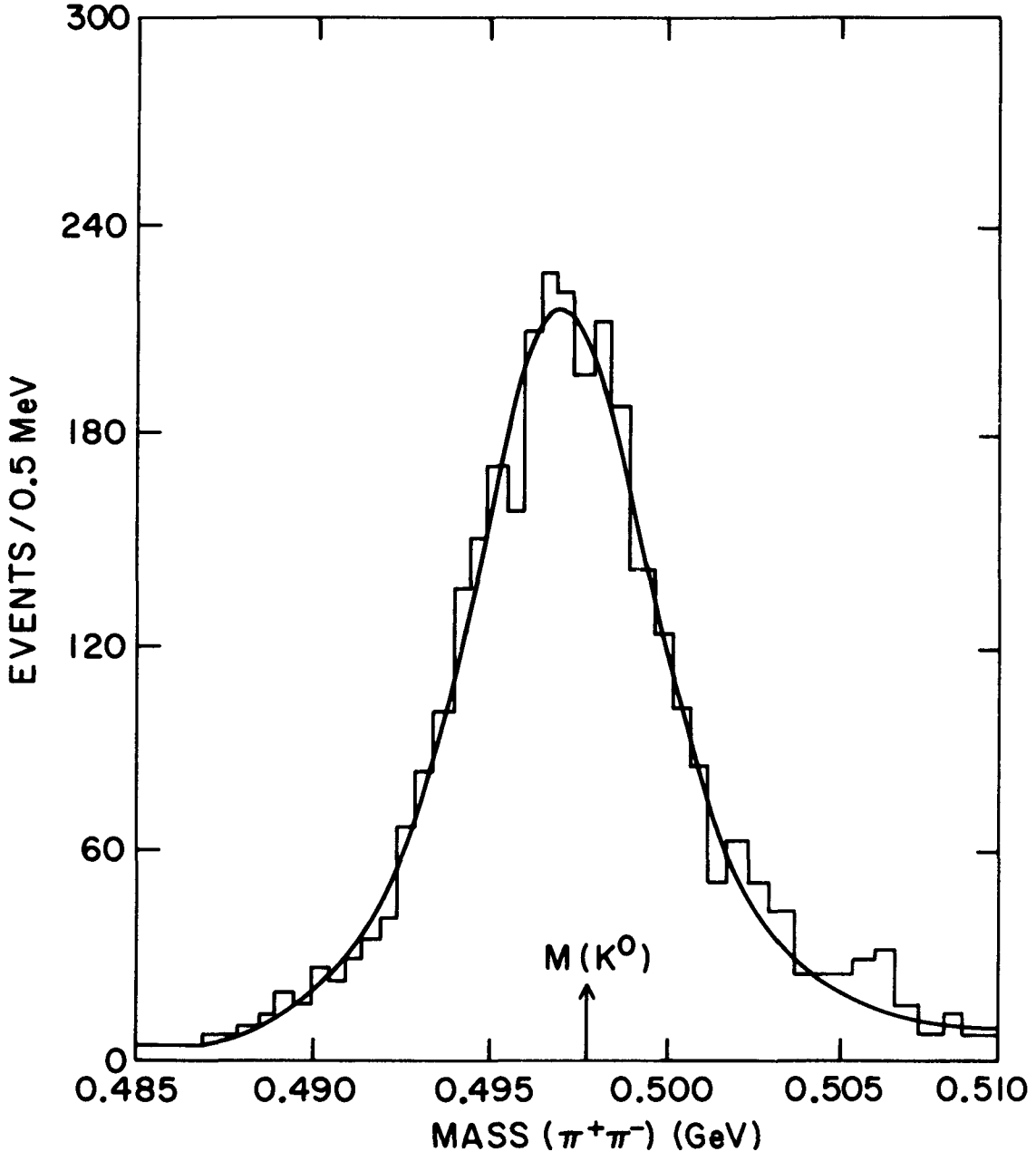
300
240
180
120
60
0
EVENTS / 0.5 MeV
M(K⁰)
0.485
0.490
0.495
0.500
0.505
0.510
MASS (π⁺π⁻) (GeV)

Figure 10

number of events. The experimentally observed rms value of the resolution for these parameters is 3.45 ± .20 MeV. The fit gives a value for the K^o mass of 497.26 ± .06 MeV which agrees with the accepted value for the K^o mass to better than .5 MeV.

Using energy and momentum conservation we can write an expression for the effective mass squared of the K^o_s, assuming that it decays into a $\pi^+\pi^-$ pair. We can then proceed to calculate the effective mass resolution for the K^o_s if we know the momentum and angular resolution of its decay products.

$$(1)\quad M^2_{K^o_s} = M^2_{\pi+} + M^2_{\pi-} + 2\sqrt{P^2_{\pi+} + M^2_{\pi+}}\cdot\sqrt{P^2_{\pi-} + M^2_{\pi-}} - 2P_{\pi+}P_{\pi-}\,\mathrm{Cos}\theta_o$$

where θ_o is the opening angle between the π^+ and π^- as seen in the lab frame, and $P_{\pi+}$, $P_{\pi-}$ are the lab momentum for the π^+ and π^- respectively.

We will first calculate the effective mass resolution for a 14 GeV/c K^o decaying into two ≃ 7-GeV/c pions. We can make some approximations in Eq. (1):

$$\sqrt{P^2_\pi + M^2_\pi} \sim P_\pi \qquad (M^2_\pi = .0019 << 49[\mathrm{GeV/c}]^2)$$

If we make the small angle approximation

$$\mathrm{Cos}\theta_o \approx 1 - \theta^2_o/2 \qquad \text{where } \theta_o \sim .070 \text{ radians}$$

Eq. (1) then becomes

$$M^2_{K^o_s} = 2M^2_\pi + (P_{\pi+}P_{\pi-})\theta^2_o$$

folding in the errors in quadrature we get

$$(2)\quad \sigma^2(M^2_{K^o_s}) = [P_{\pi+}\theta^2_o\sigma(P_{\pi-})]^2 + [P_{\pi-}\theta^2_o\sigma(P_{\pi+})]^2 + [2P_{\pi+}P_{\pi-}\theta_o\sigma(\theta_o)]^2$$

(it can be shown that $\sigma(\theta_o) \simeq \sqrt{2}\,\sigma(\theta_{xz})$). From the momentum and angular resolution associated with a 7 GeV/c pion (see Figs. 7 and 9) and from the relationship in the uncertainty in the mass squared to the uncertainty in the mass we get

$$(3)\quad \sigma_{rms}(M_{K_s^o}) \simeq \frac{\sigma_{rms}(M^2_{K_s^o})}{2M_{K_s^o}} = 3.26 \pm .30 \text{ MeV}^{*} \quad \text{(calculated)}$$

In this experiment the K^o momentum spectrum from the A_2^- decay varied over the range 3.5 - 19.5 GeV/c peaking at 15.0 GeV/c. The pion momentum spectrum associated with a K^o decay varied from 1.5 to 17.0 GeV/c peaking at 5.0 GeV/c. It is clear from Figs. 7 and 9 that the angular and momentum resolutions which are used to determine the effective mass resolution are momentum dependent.

We incorporated in our analysis program a technique for calculating $\sigma^2(M^2_{K_s^o})$ (see Eq. (2) above) based on the calculated momentum and angular resolution of the spectrometer (described in Sections D and E) on an event-by-event basis, which incorporated the momentum and angular resolutions as a function of momentum. We then evaluated the mean effective mass resolution for all K_s^o's associated with an A_2^- event. The result of the analysis yielded:

$$\sigma_{rms}(M_{K_s^o})_{(mean)} = 2.9 \pm .20 \text{ MeV}^{*} \quad \text{(calculated)}$$

as compared to an experimentally observed resolution

$$\sigma_{rms}(M_{K_s^o}) = 3.45 \pm .20 \text{ MeV} \quad \text{(experimental)}$$

---

* Errors due to uncertainty in the angular and momentum resolution contributions to the effective mass resolution.

G. The A_2^- Effective Mass Resolution

As discussed earlier (Section A) the effective mass resolution of the spectrometer is crucial for detecting fine structure (if it exists) in the A_2 effective mass spectrum. In our experiment we studied the following reaction:

$$\pi^- p \rightarrow A_2^- P$$
$$\downarrow$$
$$K^o + K^-$$
$$\downarrow$$
$$\pi^+ \pi^-$$

We determined the effective mass of the A_2^- from the momenta and angles of the final decay products of the A_2, namely the K^o and K^-.

Using energy and momentum conservation we can write an expression for the effective mass of the A_2^- squared.

$$(1) \quad M^2_{A_2^-} = M^2_{K^o} + M^2_{K^-} + 2\sqrt{P^2_{K^o} + M^2_{K^o}}\sqrt{P^2_{K^-} + M^2_{K^-}}$$
$$- 2 P_{K^o} P_{K^-} \cos\theta_{K^o K^-}$$

where $\theta_{K^o K^-}$ is the opening angle between the K^o and the K^- in the laboratory frame, and P_{K^o}, P_{K^-} are the laboratory momenta of the K^o and K^- respectively. It is clear that the effective mass resolution of the A_2 is determined by the accuracy of measurement of the angles and momenta of its decay products.

If we make the small angle approximation for $\cos\theta_{K^oK^-}$ and expand $\sqrt{P^2+M^2}$ using the binomial expansion, Eq. (1) takes the form

$$(2)\quad M^2_{A_2^-} = M^2_{K_o} + M^2_{K^-} + \frac{P_{K^o}M^2_{K^-}}{P_{K^-}} + \frac{P_{K^-}M^2_{K^o}}{P_{K^o}} + P_{K^o}P_{K^-}\theta^2_{K^oK^-}$$

where $\theta^2_{K^oK^-} \approx (\theta_{xzK^-} - \theta_{xzK^o})^2 + (\theta_{yzK^-} - \theta_{yzK^o})^2$.

We then proceed to fold in the contributions to the resolution of the effective mass squared:

$$(3)\quad \sigma^2(M^2_{A_2^-}) = \left[\frac{\partial(M^2_{A_2^-})}{\partial P_{K^o}}\sigma(P_{K^o})\right]^2 + \left[\frac{\partial(M^2_{A_2^-})}{\partial P_{K^-}}\sigma(P_{K^-})\right]^2 + \left[\frac{\partial(M^2_{A_2^-})}{\partial\theta_{K^oK^-}}\sigma(\theta_{K^oK^-})\right]^2$$

From the relationship in the uncertainty in the mass squared to the uncertainty in the mass, we evaluate the A_2 mass resolution:

$$(4)\quad \sigma(M_{A_2}) \approx \frac{\sigma(M^2_{A_2})}{2\cdot M_{A_2}}\,.$$

Since the momentum and angular resolutions are momentum dependent, we incorporated in our analysis program a technique for evaluating Eq. (4) on an event-by-event basis. We folded into the effective mass resolution the contributions from the momentum and angular resolutions as a function of the momentum of the particles, and in addition we included the contribution to the angular resolution from multiple scattering of the K^- in the liquid hydrogen as a function of the decay point of the A_2^- (i.e. the amount of liquid hydrogen that the K^- traversed).

The calculated effective mass resolution of the A_2^- from the above analysis was

$$\sigma_{rms}(M_{A_2^-}) = 4.25 \pm .20 \text{ MeV}. \tag{5}$$

The largest contribution was the angular resolution of the spectrometer which contributed approximately 40% to the square of the A_2 mass resolution. The momentum resolution, and the multiple scattering of the K^- in the hydrogen target and the target veto counter each contributed approximately 30%. All of the accepted events had the K^o decay point downstream of the target counter. The calculated A_2 mass resolution $\sigma_{rms} = 4.25 \pm .20$ MeV would clearly be sufficient in studying the possibility of a dip in the A_2 mass spectrum. In attempting the fits to the mass spectra with the CERN dipole form (see Chapter V, Sec. f) we used a Gaussian resolution function with $\sigma_{rms}(M_{A_2^-}) = 5$ MeV.

CHAPTER V

EFFECTIVE MASS DATA

A. Introduction

We have studied the reaction

$$\pi^- P \rightarrow K_s^o K^- + P$$

at 22.4 and 23.9 GeV/c incident beam momenta. In this chapter we will basically concern ourselves with the question of the shape and mass of the A_2^- resonance produced in the above reaction. A total of 3346 events were obtained (2370 at 23.9 GeV/c and 976 at 22.4 GeV/c compared to 721 in the previous experiment[10]) in the effective mass range $1.1 < M(K_s^o K^-) < 1.5$ GeV. Because of the high statistics, low background, and good mass resolution, we were able to study the shape of the A_2 mass spectrum and also to investigate the possibility that the mass spectrum exhibits a split in limited t' regions.

B. The Effective Mass Data

The effective 2π mass spectrum in the K^o mass region for the reaction $\pi^- P \rightarrow K_s^o K^- + P$ is shown in Fig. 11. We required that the effective $K_s^o K^-$ mass be between 1.1 and 1.5 GeV. The smooth curve in Fig. 11 is the result of a maximum likelihood fit to the data assuming a functional form constructed by summing two Gaussian terms with different widths (see Chapter IV, Sec. F for further details). The fit gives a value for the K^o mass of $497.26 \pm .06$ MeV which agrees with the accepted value for the K^o mass to better than .5 MeV.[14]

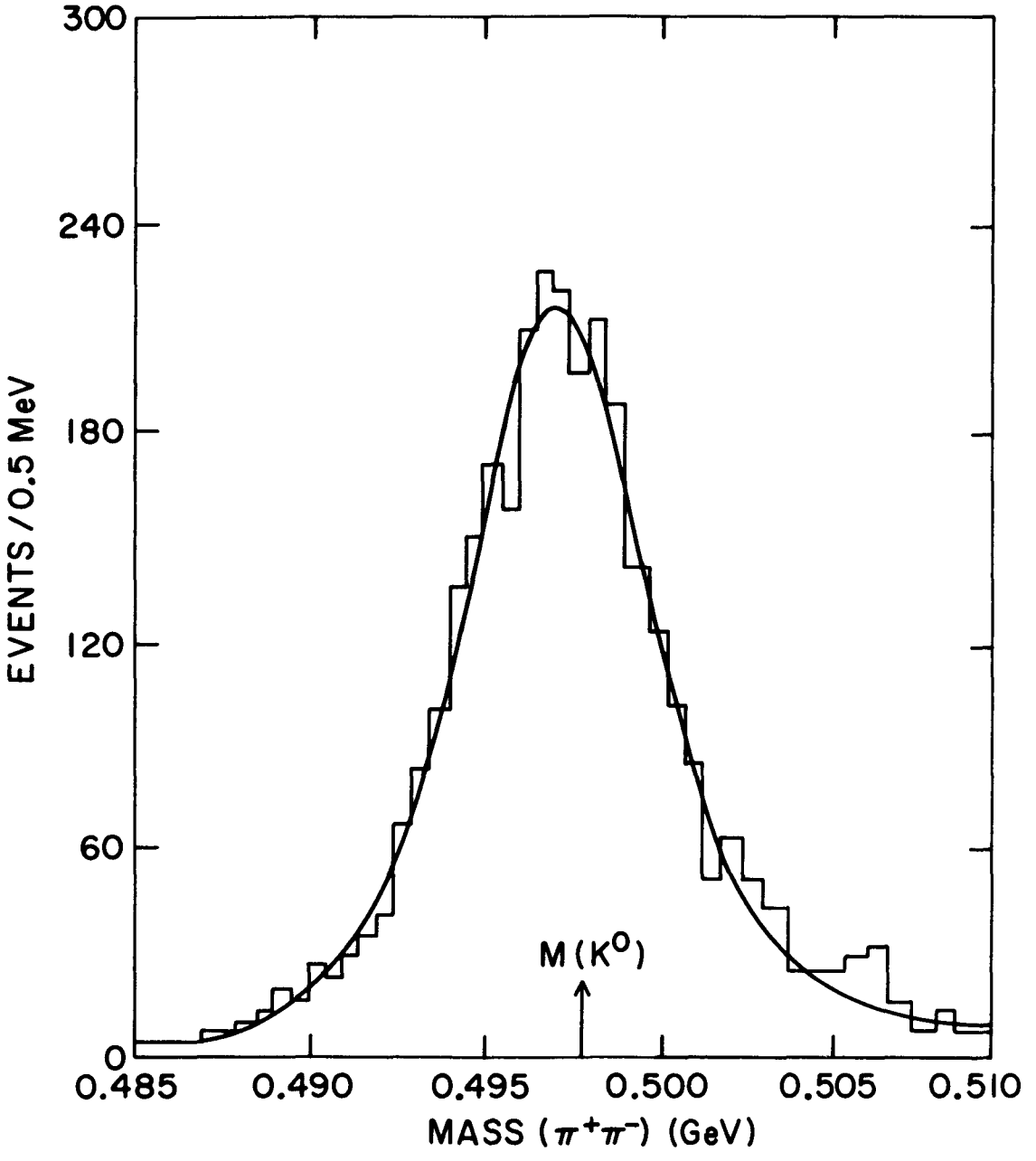
300
240
180
120
60
0
EVENTS / 0.5 MeV
M(K⁰)
0.485
0.490
0.495
0.500
0.505
0.510
MASS (π⁺π⁻) (GeV)

Figure 11

We selected events that had a topology consisting of a neutral vee (K^o) and a negative track whose projections intersected a common point in the target. The effective mass of the vee (assuming the vee decayed into a $\pi^+\pi^-$) was required to be between .485 and .510 GeV. These events could then be analyzed as either K^oK^- or $K^o\pi^-$.

The effective mass spectrum for all the events analyzed on the basis of the K^oK^- hypothesis uncorrected for the acceptance of the spectrometer is shown in Fig. 12. The A_2 signal at $\sim$ 1.3 GeV on top of a rather large background can be seen. The effective mass spectrum is shown in Fig. 13 for the events analyzed on the basis of the $K^o\pi^-$ hypothesis (the negative prong is assumed to be a π^-) uncorrected for the acceptance of the spectrometer. A clear peak corresponding to the $K^*(890)$ can be seen in this spectrum.

The missing mass spectrum of the events for the $K^o_sK^-$ hypothesis uncorrected for the acceptance of the apparatus is shown in Fig. 14 There is a peak at the proton mass with a finite width commensurate with our missing mass resolution. The full width at half maximum (FWHM) is $\sim$ 195 MeV.

The $K^o_sK^-$ effective mass spectrum between 1.1 and 1.5 GeV for those events with a missing mass between .7 and 1.1 GeV (i.e. proton recoil) is shown in Fig. 15. The spectrum is uncorrected for the acceptance of the spectrometer. One can see a clean A_2 signal at $\simeq$ 1.3 GeV on top of a rather small background. Figure 16 shows the $K^o_sK^-$ effective mass spectrum for those events having a missing mass between .7 and 1.1 GeV corrected for the acceptance of our apparatus.

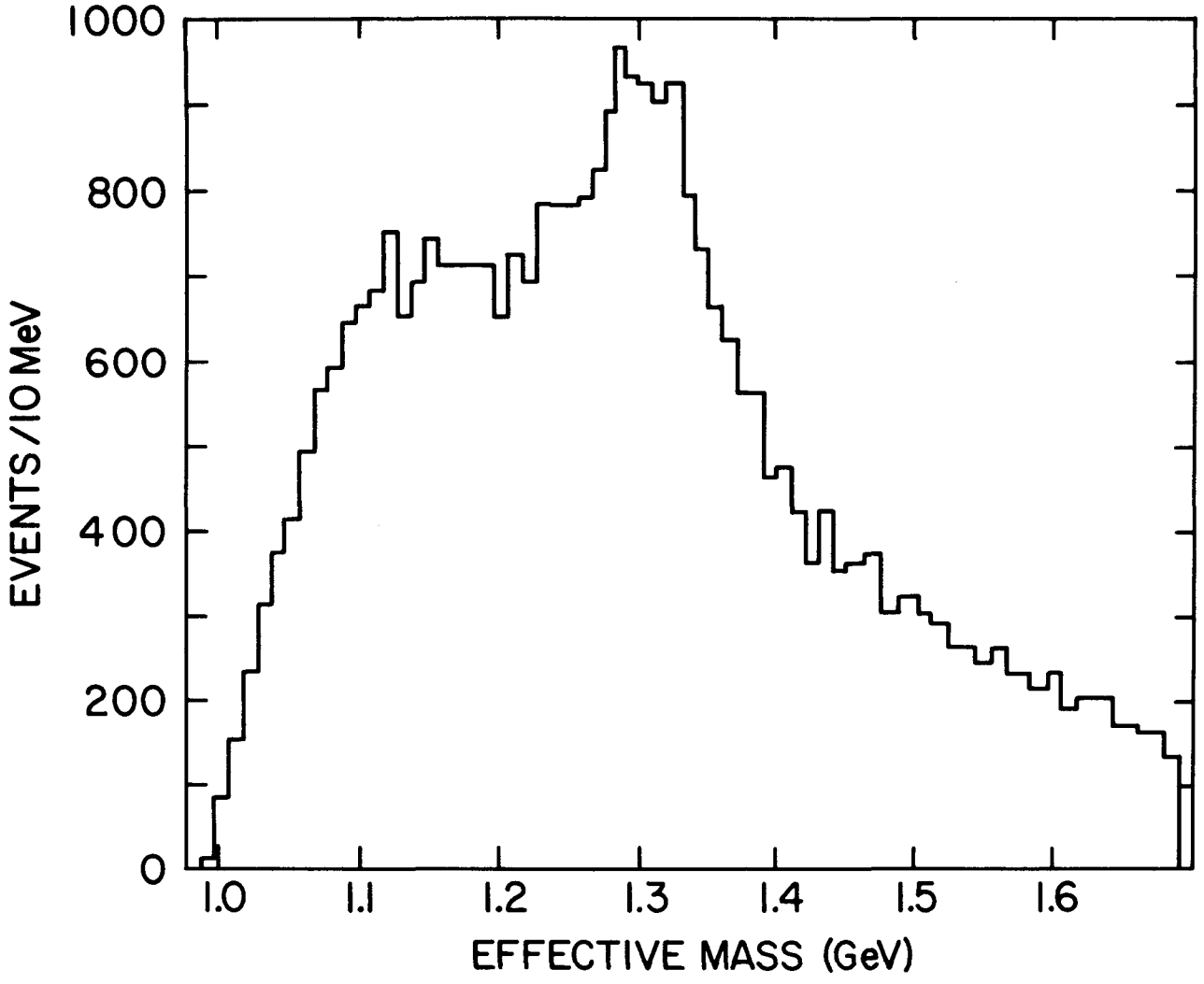
1000
800
600
400
200
0
EVENTS/10 MeV
1.0
1.1
1.2
1.3
1.4
1.5
1.6
EFFECTIVE MASS (GeV)

Figure 12

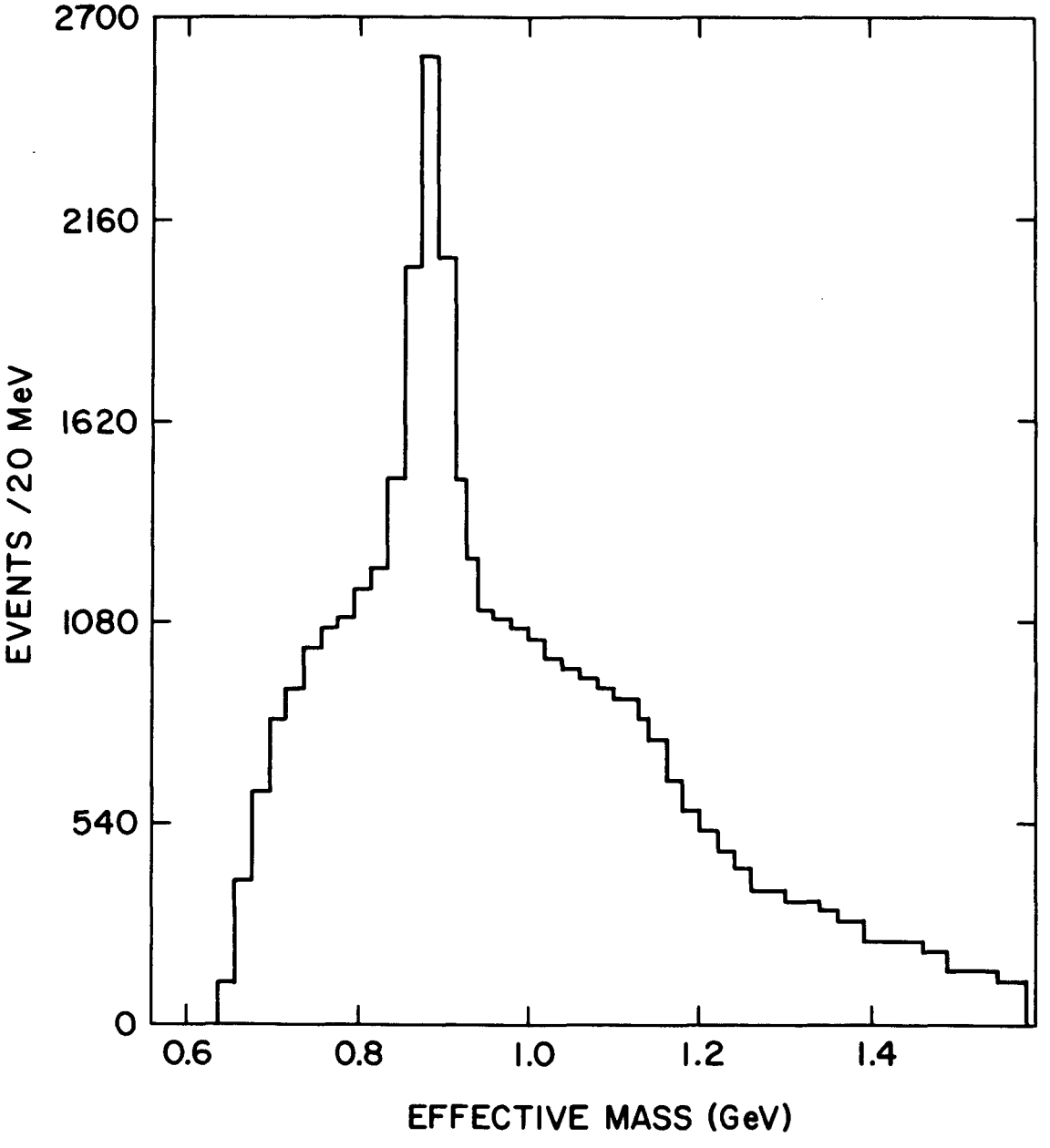
2700
2160
1620
1080
540
0
EVENTS /20 MeV
0.6
0.8
1.0
1.2
1.4
EFFECTIVE MASS (GeV)

Figure 13

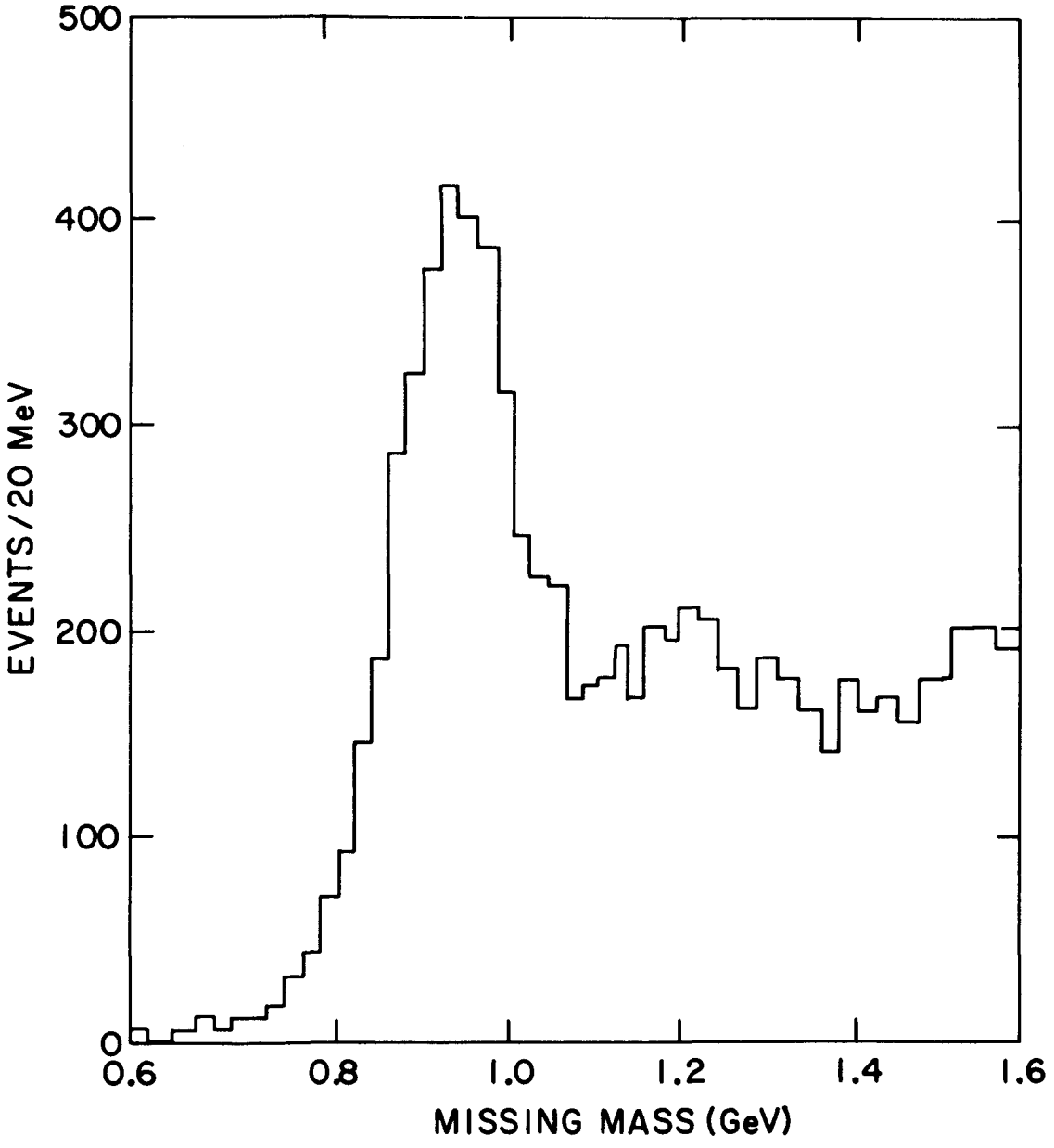
500
400
300
200
100
0
EVENTS/20 MeV
0.6
0.8
1.0
1.2
1.4
1.6
MISSING MASS (GeV)

Figure 14

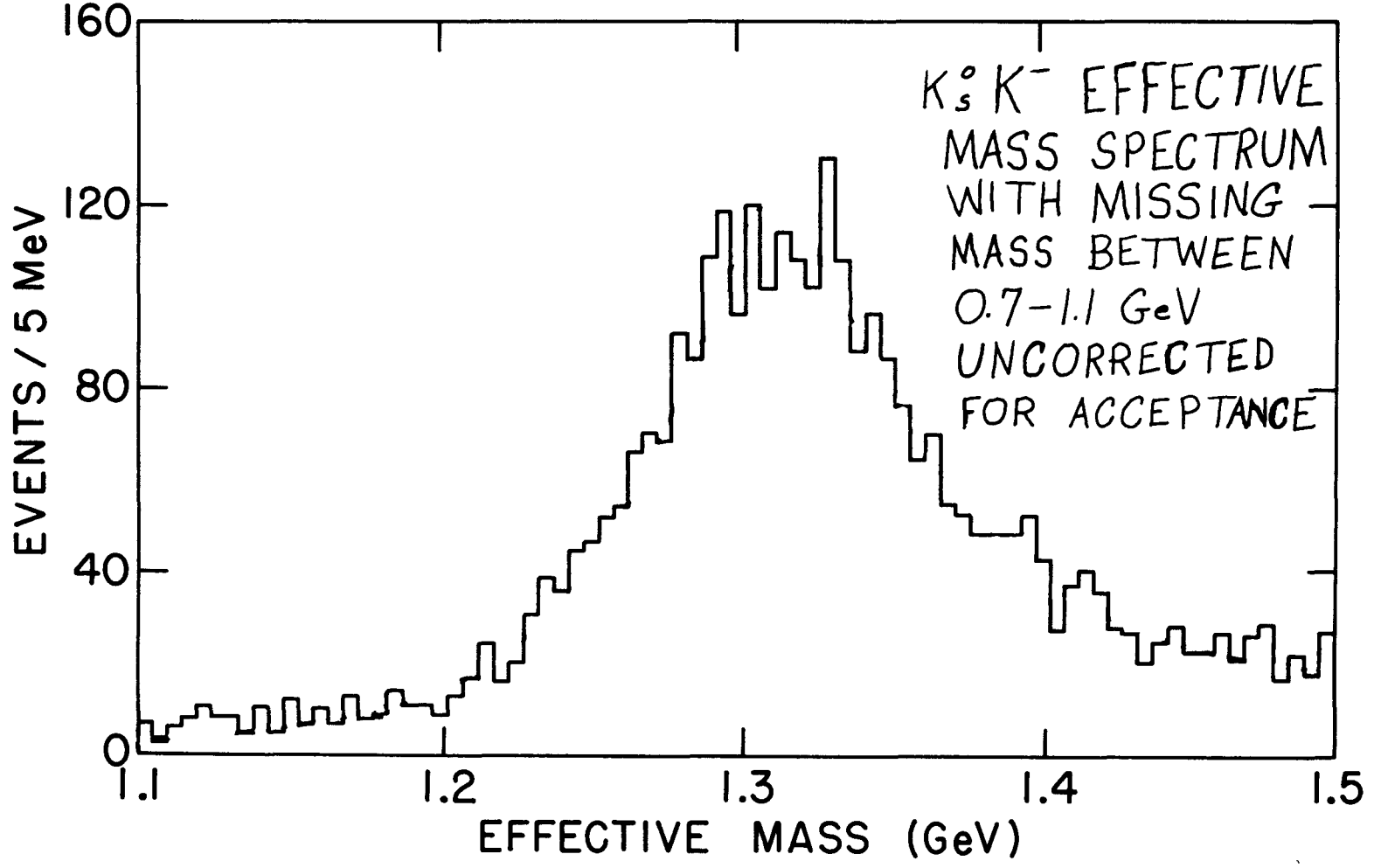
160
120
80
40
0
EVENTS / 5 MeV
1.1
1.2
1.3
1.4
1.5
EFFECTIVE MASS (GeV)
$K_s^o K^-$ EFFECTIVE MASS SPECTRUM WITH MISSING MASS BETWEEN 0.7–1.1 GeV UNCORRECTED FOR ACCEPTANCE

Figure 15

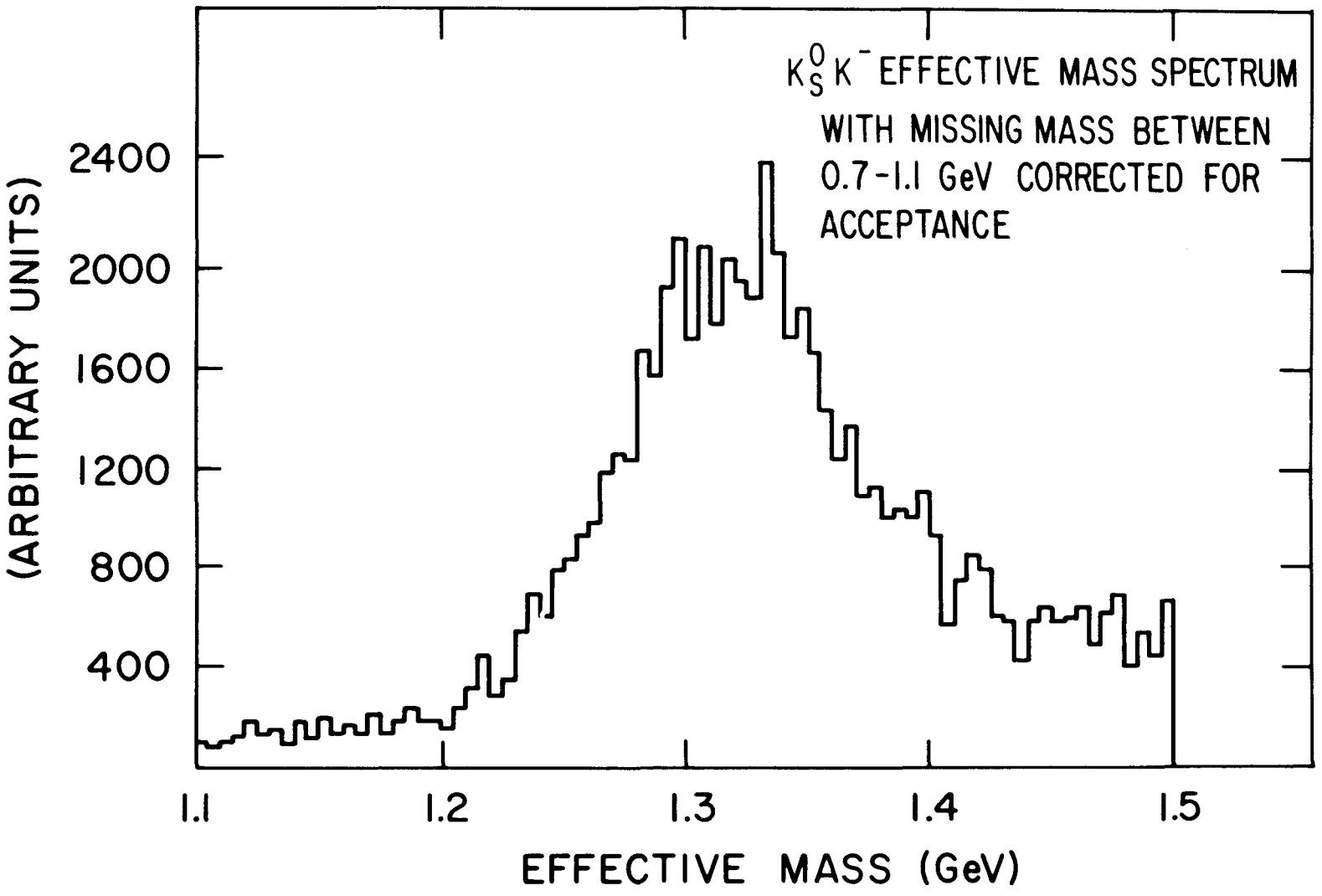
$K_S^0 K^-$ EFFECTIVE MASS SPECTRUM
WITH MISSING MASS BETWEEN
0.7-1.1 GeV CORRECTED FOR
ACCEPTANCE
(ARBITRARY UNITS)
2400
2000
1600
1200
800
400
1.1
1.2
1.3
1.4
1.5
EFFECTIVE MASS (GeV)

Figure 16

We note that this was an effective mass experiment where we determined the A_2^- mass from a direct measurement of the angles and momenta of the final decay products of the resonance as opposed to a missing mass experiment (see Chapter I, Sec. B) where one reconstructs the mass of the resonance without measuring the momenta and angles of the decay products of the resonance.

C. The Proton Cut

It is clear from the comparison of the $K_s^0K^-$ effective mass spectra with and without the proton recoil (Figs. 15 and 12 respectively) that the proton cut is crucial to our experiment. In this analysis we did not directly identify the negative prong associated with the K^o to be a K^-. By requiring the recoil particle to be a proton we insured that the negative prong must be a K^- since there is no strange charged baryon with mass less than 1.189 GeV. Strangeness and baryon conservation would thus require that the resonance we are investigating be a meson of zero strangeness. Thus the proton recoil cut would almost entirely eliminate from our K^oK^- effective mass spectrum the $K^o\pi^-$ decays of the $K^{*-}(890)$, which is a meson of strangeness -1. Furthermore it allows us to study the single reaction $\pi^-P \to A_2^-P$ with a minimum of background.

D. Background Contamination of the $K_s^oK^-$ Effective Mass Spectrum

Below is a list of the possible reactions which might contribute to the background in the $K_s^oK^-$ effective mass spectrum:

(1) $\pi^-P \to \underbrace{K^o + \pi^-}_{\text{nonresonant}} + \Sigma^+$

(2) $\pi^- P \rightarrow \underbrace{K^o + K^-}_{\text{nonresonant}} + P$

(3) $\pi^- P \rightarrow A_2^- + \Delta^+(1236)$

(4) $\pi^- P \rightarrow A_2^- + P + N\pi$'s

(where N is an integer).

The contributions to the background from reactions (1), (3), and (4) are due to the finite missing mass resolution of the recoiling nucleon ($\sigma \simeq 85$ MeV). The predominant contribution to the background in reaction (4) would occur with N = 1 and to a lesser extent N = 2.

E. D-Wave Breit-Wigner Fits to the $K_s^o K^-$ Effective Mass Spectra

Since the A_2^- is assumed to be a resonance with spin 2 (see Chapter VII), it is reasonable to fit the mass spectrum with a D-wave Breit-Wigner shape.[23]

Figure 17 shows the $K_s^o K^-$ effective mass spectrum over all t'. In order to show the statistical significance of the data, the spectrum has not been corrected for the acceptance of the apparatus. We have instead corrected the theoretically expected distribution (the smooth curve in Fig. 17) by the acceptance of the spectrometer. Figure 18 indicates the acceptance of the apparatus as a function of mass.

The mass spectrum is dominated by the A_2 peak. We have performed a maximum likelihood[22] fit to the data with a D-wave Breit-Wigner[23] and a linear background starting at threshold over the mass region

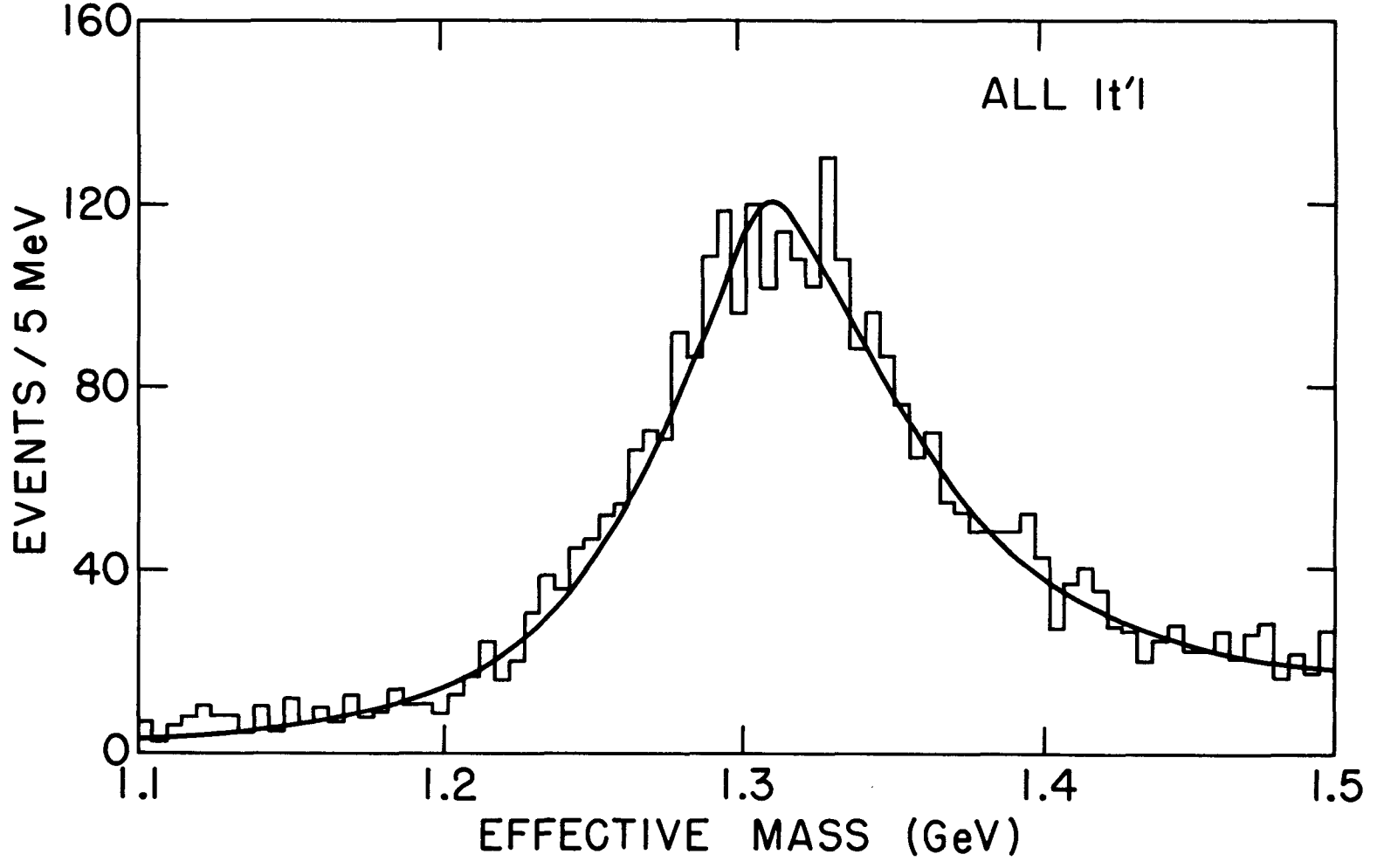
160
120
80
40
0
EVENTS / 5 MeV
ALL |t'|
1.1
1.2
1.3
1.4
1.5
EFFECTIVE MASS (GeV)

Figure 17

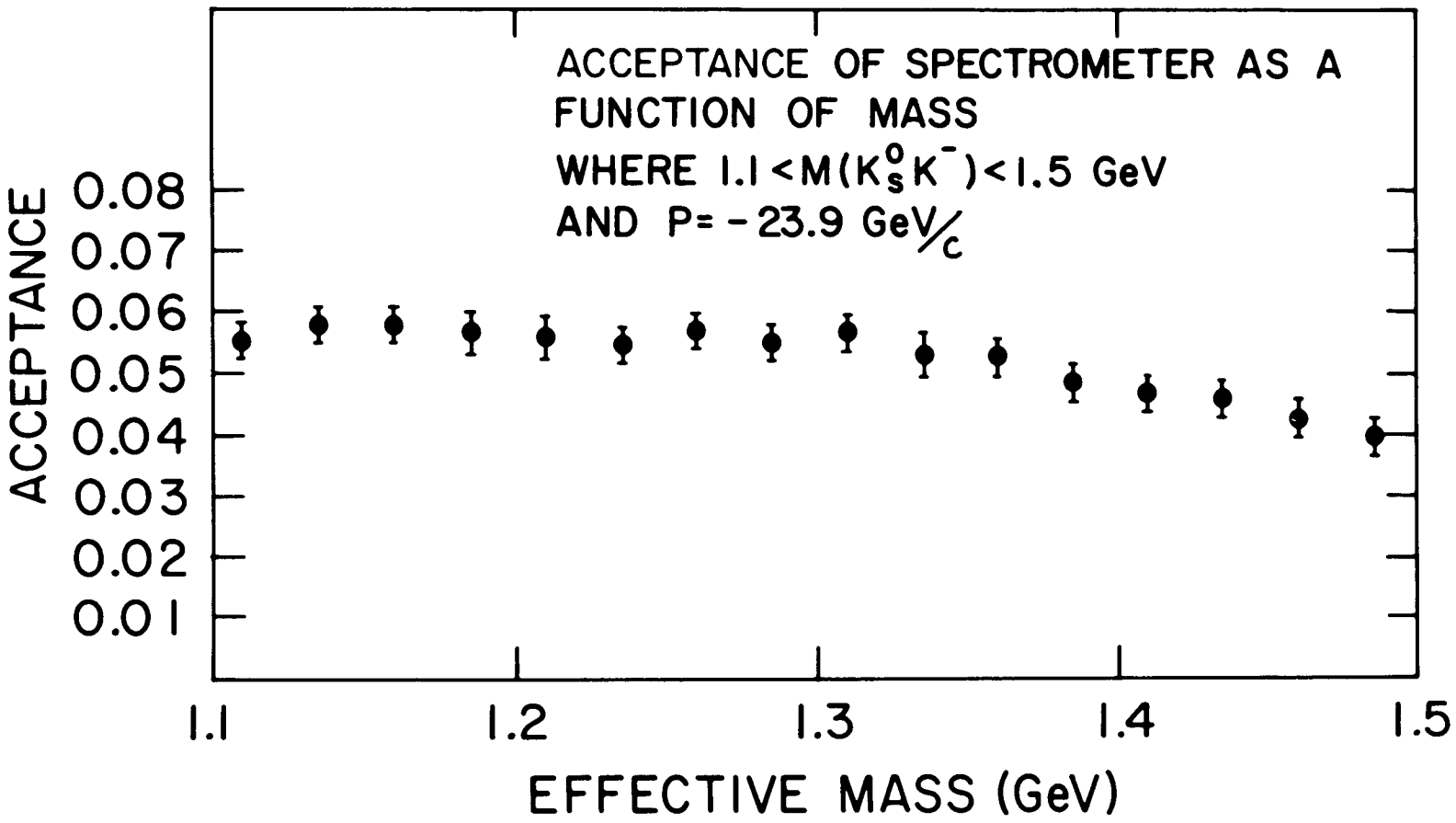
ACCEPTANCE OF SPECTROMETER AS A
FUNCTION OF MASS
WHERE 1.1 < M($K^0_s K^-$) < 1.5 GeV
AND P = -23.9 GeV/c
ACCEPTANCE
0.08
0.07
0.06
0.05
0.04
0.03
0.02
0.01
1.1
1.2
1.3
1.4
1.5
EFFECTIVE MASS (GeV)

Figure 18

1.1-1.5 GeV. The Breit-Wigner form used was as follows:

$$N(M) = \frac{MM_o\Gamma(M)}{(M^2-M_o^2)^2 + [M_o\Gamma(M)]^2}$$

and $$\Gamma(M) = \Gamma_o\left(\frac{q}{q_o}\right)^5 \frac{\rho(q)}{\rho(q_o)}$$

where $q_o = q(M_o)$ and q is the momentum of either the K^o or the K^- in the A_2 rest frame. $\rho(q)$ is a slowly varying factor correcting for angular momentum barrier effects. We have used[24]

$$\rho(q) = (9 + 3R^2q^2 + R^4q^4)^{-1},$$

where R is fitted as a free parameter. For all of the fits listed in Table 5a we have allowed the mass, width, R and the slope of the background to be free parameters.

The data in all t' regions investigated are well fitted by a D-wave Breit-Wigner and a linear background starting at threshold (0.99 GeV). In all of the fits we have folded in a mass resolution of 5 MeV and corrected for the acceptance of the spectrometer by reducing the theoretically expected distribution (D-wave Breit-Wigner) for the acceptance of the apparatus.

The results of a maximum likelihood fit to the overall $K_s^oK^-$ effective mass spectrum in the mass region 1.1-1.5 GeV are $m_o = 1.320 \pm .002$ GeV, $\Gamma_o = .105 \pm .006$ GeV, $R = 4.4 \pm .7$ GeV^{-1} and $\chi^2 = 69$ for 76

degrees of freedom (DOF). Other details of the fit are listed as fit (1) in Table 5a.

Fits were also made for the t' regions:

$$0.0 < -t' < 0.2$$

$$0.2 < -t' < 0.29$$

and $$.29 < -t'$$

The results of these fits in the mass interval 1.1-1.5 GeV are given in Table 5a. (fits 2-4) and are shown in Figs. 19 through 21. The errors on the fit parameters were calculated by changing the value of that parameter until the logarithm of the likelihood function decreased by .5 from its maximum value.† We estimate that the mass scale is uncertain by ≃ 1 MeV from our knowledge of the reconstructed K^o mass (Chapter V, Sec. B) which is within .5 MeV of the accepted value for the K^o mass.[14] We note that the D-wave Γ_o is strongly correlated with the D-wave R parameter and that systematic uncertainties in the mass acceptance would produce tradeoffs between these two parameters.

We conclude that a single D-wave Breit-Wigner of the same width and mean mass (plus a background level ∿ 10-20%) fits the data very well (chi-square per degree of freedom ≃ 1) in all t' regions investigated.

---

† This is equivalent to changing the parameter by one standard deviation.

Table 5a

Results of D-Wave Breit-Wigner Fits to the K^oK^- Mass Spectra from 1.1 to 1.5 GeV

Fit No.	$-t'$ $(GeV/c)^2$	M_o(GeV)	Γ_o(GeV)	$R(GeV)^{-1}$	χ^2	DOF	Total Events	Fitted Background
(1)	All t'	$1.320 \pm .002$	$.105 \pm .006$	$4.4 \pm .7$	69	76	3346	622
(2)	0.0-0.2	$1.320 \pm .002$	$.094 \pm .008$	8.7 ± 4.3	63	76	1539	370
(3)	0.2-0.29	$1.323 \pm .004$	$.122 \pm .014$	4.5 ± 1.4	53	76	633	63
(4)	> .29	$1.319 \pm .003$	$.105 \pm .010$	2.8 ± 1.0	81	76	1174	161

The errors shown are statistical only.

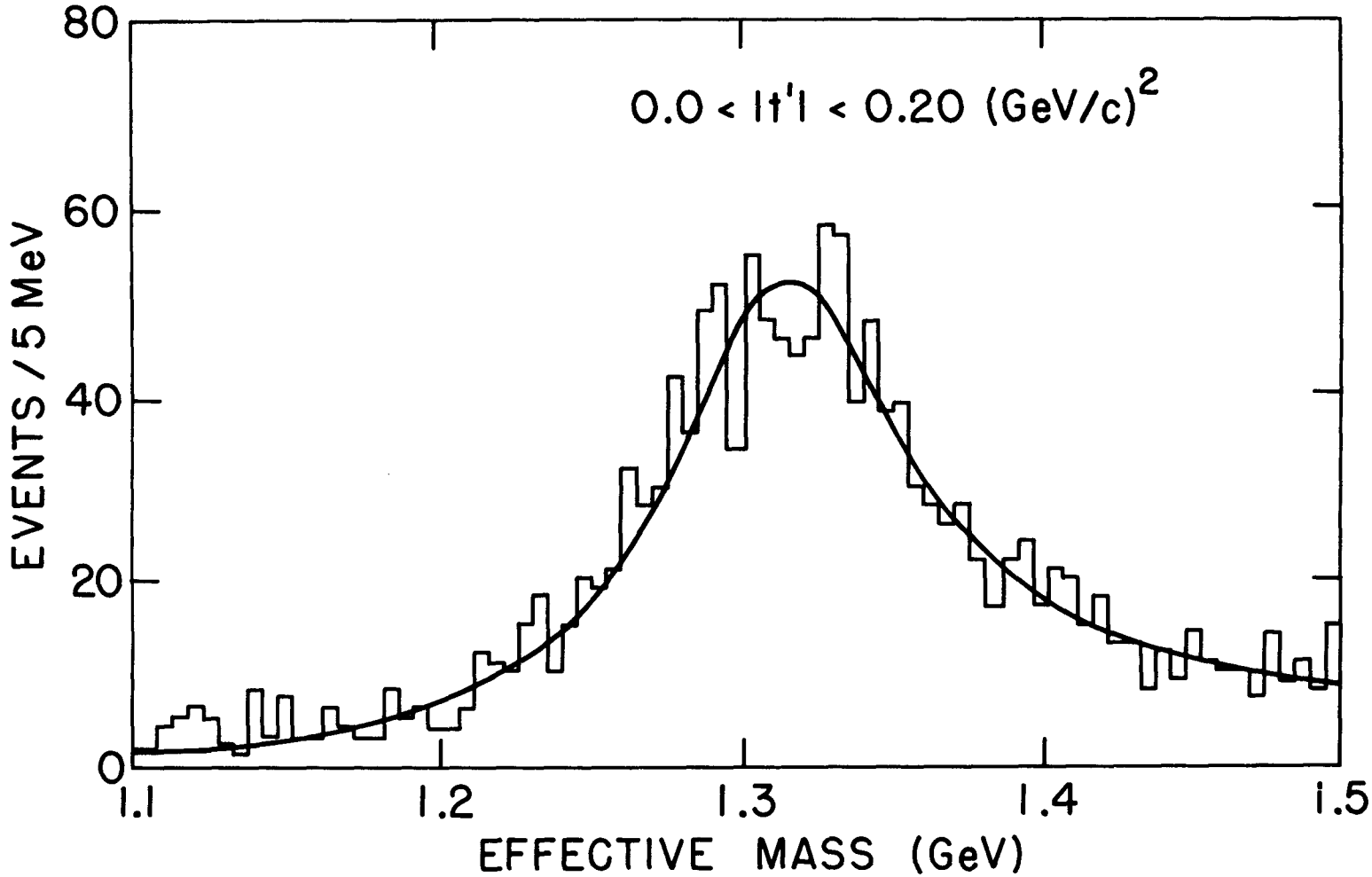
80
60
40
20
0
EVENTS / 5 MeV
0.0 < |t'| < 0.20 (GeV/c)^2
1.1
1.2
1.3
1.4
1.5
EFFECTIVE MASS (GeV)

Figure 19

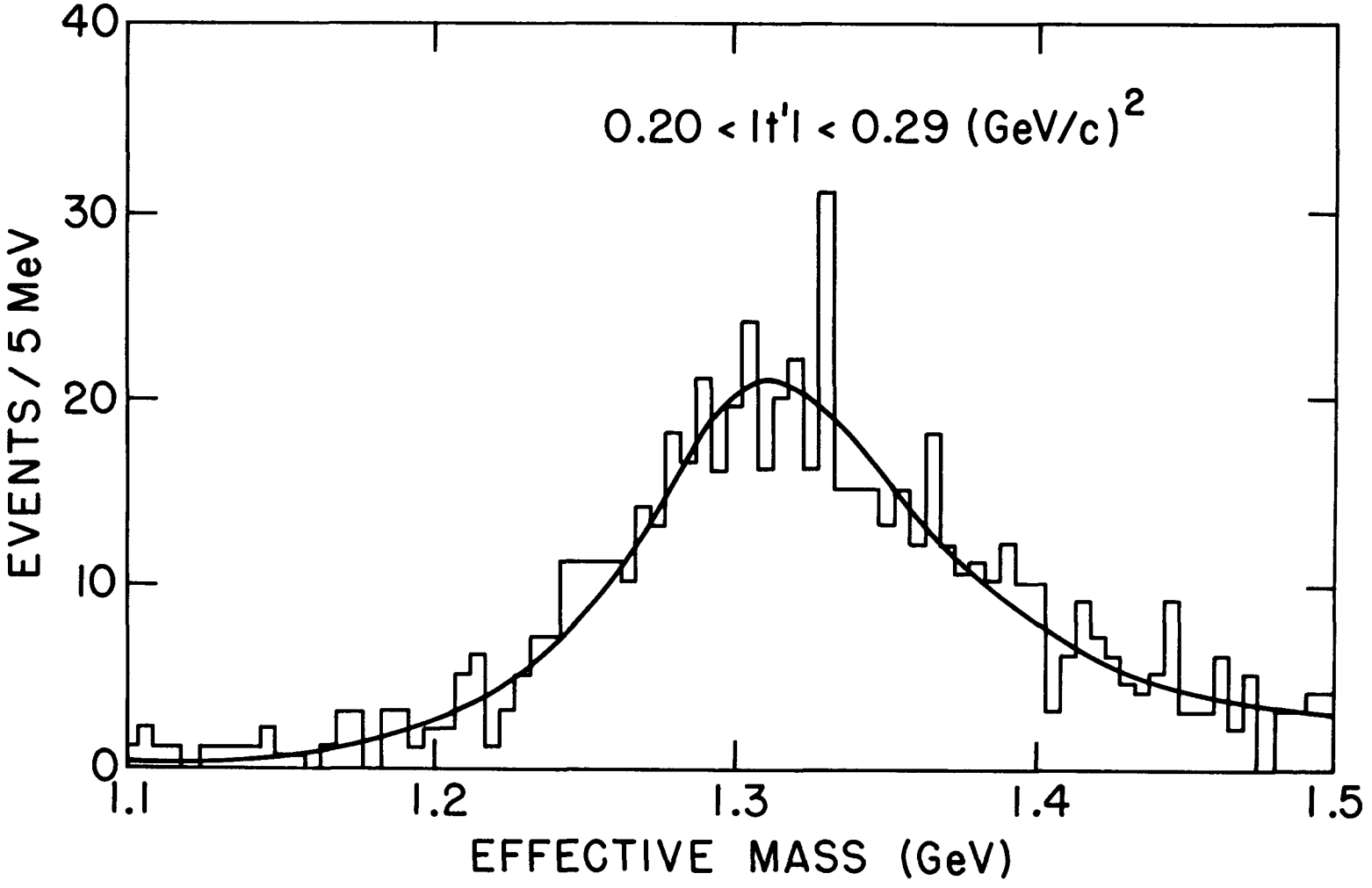
40
30
20
10
0
EVENTS / 5 MeV
0.20 < |t'| < 0.29 (GeV/c)^2
1.1
1.2
1.3
1.4
1.5
EFFECTIVE MASS (GeV)

Figure 20

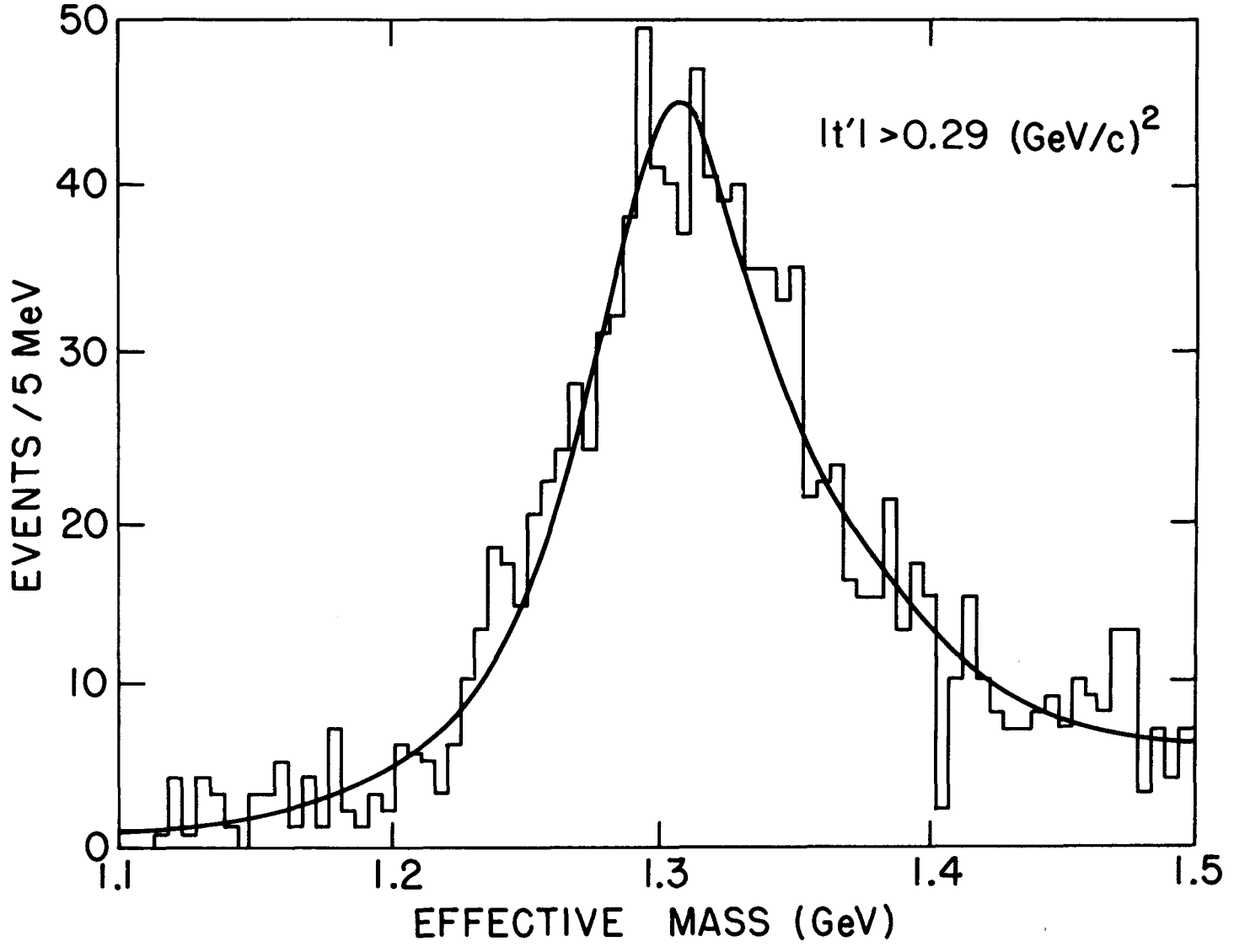
50
40
30
20
10
0
EVENTS / 5 MeV
|t'| >0.29 (GeV/c)^2
1.1
1.2
1.3
1.4
1.5
EFFECTIVE MASS (GeV)

Figure 21

F. Dipole Fits to the $K_s^o K^-$ Effective Mass Spectra

We have also attempted to fit the data with the dipole shape used in the analysis of the CERN missing mass data[4]

where $$N(M) = \frac{\Gamma^2 (M-M_o)^2}{\left[(M-M_o)^2 + \frac{\Gamma^2}{4}\right]^2}$$

In doing these fits we folded into the functional form a mass resolution of 5 MeV and corrected for the spectrometer acceptance. Γ and M_o were free parameters. We attempted fitting the mass spectra with the above form and the best values for Γ and M_o were $\sim$ 28 and 1315 MeV respectively. Figure 22 is the best fit to the mass spectrum for $1.1 < M(K_s^o K^-) < 1.5$ GeV over all t' using the above dipole form and a linear background starting at threshold (.99 GeV). The slope of the background was allowed to be a free parameter. The best fit has a χ^2 of 205 for 77 degrees of freedom which corresponds to a rejection of 7.9 standard deviations * (See Table 5b, fit (5)).

The data were then broken into different t' bins as for the Breit-Wigner fits above, and each set was fitted to a dipole plus a linear background with the mass and width allowed to be free parameters. In attempting to fit the data with the above form, we first narrowed the mass region to $1.2 < M(K_s^o K^-) < 1.4$ GeV to emphasize the contribution of the dipole. This mass region was too narrow to determine the background adequately. We first fitted the data to a dipole plus a linear

* The rejection of the fit is determined by the expression $\sqrt{2\chi^2} - \sqrt{2N_D - 1}$ in units of standard deviations. (See Review of Particle Properties 1973, p. 48). N_D represents the number of degrees of freedom of the fit.

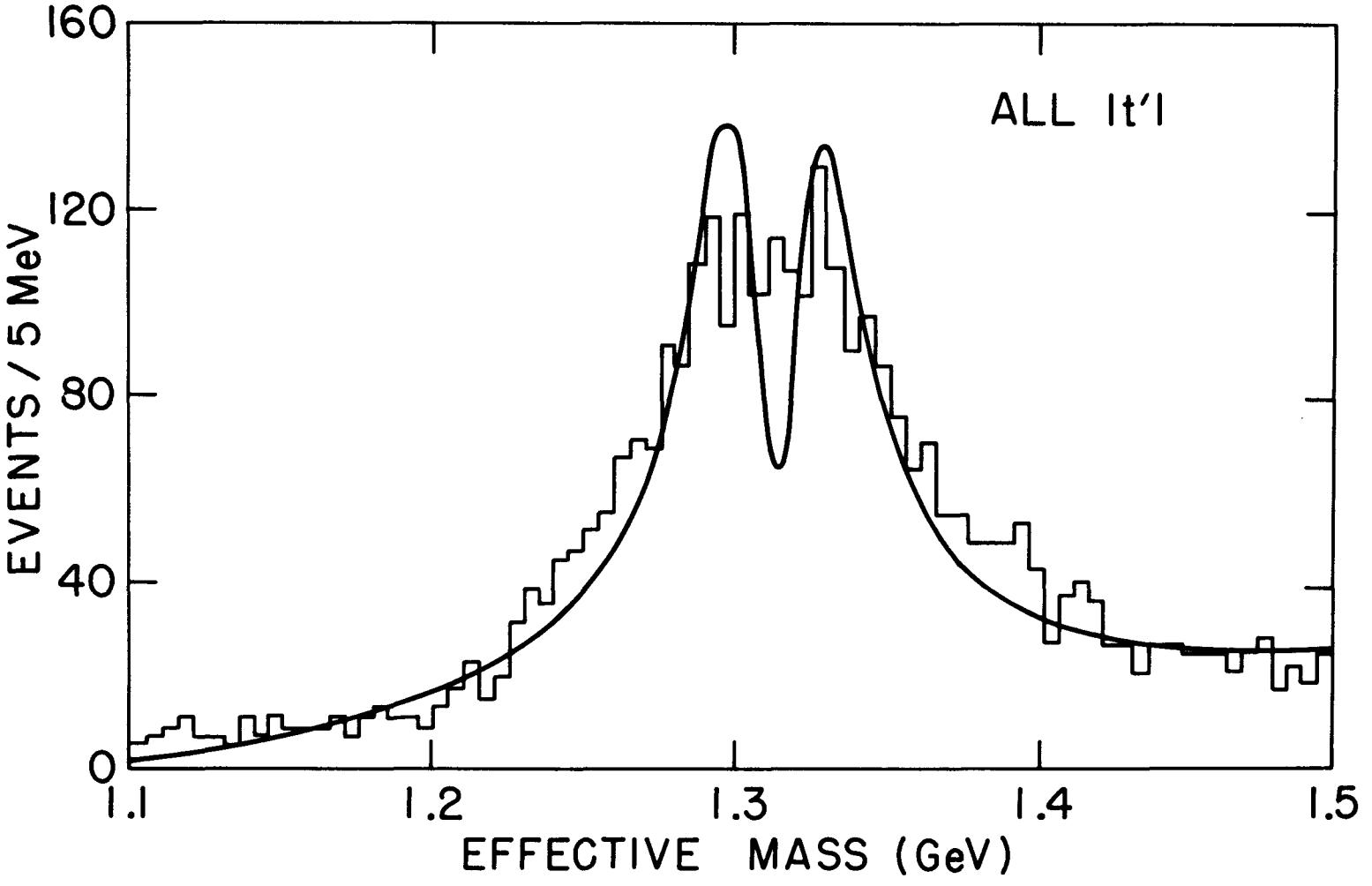
ALL |t'|
EVENTS / 5 MeV
0
40
80
120
160
1.1
1.2
1.3
1.4
1.5
EFFECTIVE MASS (GeV)

Figure 22

Table 5b

Results of Fitting the K^oK^- Effective Mass Spectra with the CERN Missing Mass Dipole Form and a Linear Background.

Fit No.	$-t'$ $(GeV/c)^2$	Mass Interval (GeV)	χ^2	Degrees of Freedom	Standard Deviations	Total Events	Fitted Background
(5)	All t'	1.1 -1.5	205	77	7.9σ	3346	1256
(6)	0.0-.20	1.2 -1.4	68	38	3.0σ	1187	245
(7)	.20-.29	1.2 -1.4	68	38	3.0σ	502	92.5
(8)	> .29	1.2 -1.4	77	38	3.8σ	956	182.2
(9)	All t'	1.25-1.35	71	18	6.0σ	1815	352.8

background in the mass range $1.1 < M(K^o_s K^-) < 1.7$ GeV. The background level so obtained (19 $\pm$ 1% of the total events) was then used as a fixed linear background in the fits for the 1.2 to 1.4 GeV interval Figures 23 - 25 show the best fits to the mass spectra in the above mass range (1.2-1.4 GeV) for the t' regions $-t' < 0.2$, $.20 < -t' < .29$, and $-t' > .29$ respectively. The improbability for the fits in the t' regions $-t' < .2$, $.20 < -t' < 0.29$ and $.29 < -t'$ corresponded to 3.0σ, 3.0σ, and 3.8σ respectively. Table 5b, fits (6-8) indicate the details of the fits to the CERN dipole form (in the mass interval of the $K^o_s K^-$ = 1.2-1.4 GeV) for the three t' regions mentioned above. For all of the fits indicated in Table 5b the mass and width were allowed to be free parameters.

In order to concentrate on the region where the functional form has a dip and to eliminate contributions to the χ^2 from the tails of the mass spectrum, we fitted the total data sample in the mass region $1.25 < M(K^o_s K^-) < 1.35$ GeV (see Fig. 26). The background level was fixed at that determined by a fit over the mass range $1.1 < M(K^o_s K^-) < 1.5$ GeV (the background was 19.4% of the total events). The best fit has a χ^2 of 71 for 18 DOF or a 6 standard deviation rejection. (See Table 5b, fit (9).)

G. Conclusions

In the reaction $\pi^- p \rightarrow K^o_s K^- + P$ using $\simeq$ 23 GeV/c incident pions and analyzing 3346 new events, we find that, in the effective mass range for the $K^o_s K^-$ = 1.1-1.5 GeV, all the data are well fitted (χ^2 of 69 for

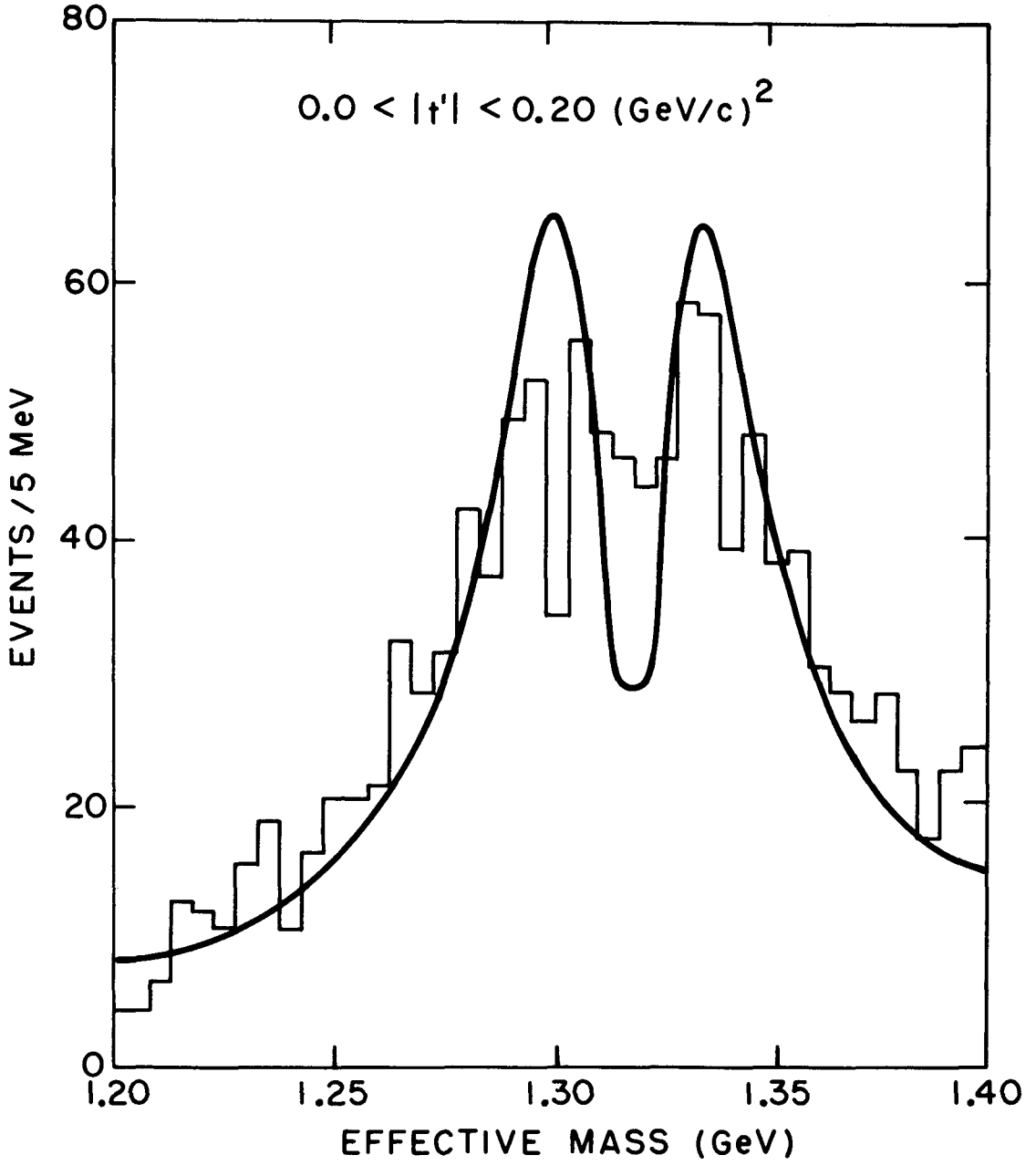
0.0 < |t'| < 0.20 (GeV/c)^2
EVENTS/5 MeV
0
20
40
60
80
1.20
1.25
1.30
1.35
1.40
EFFECTIVE MASS (GeV)

Figure 23

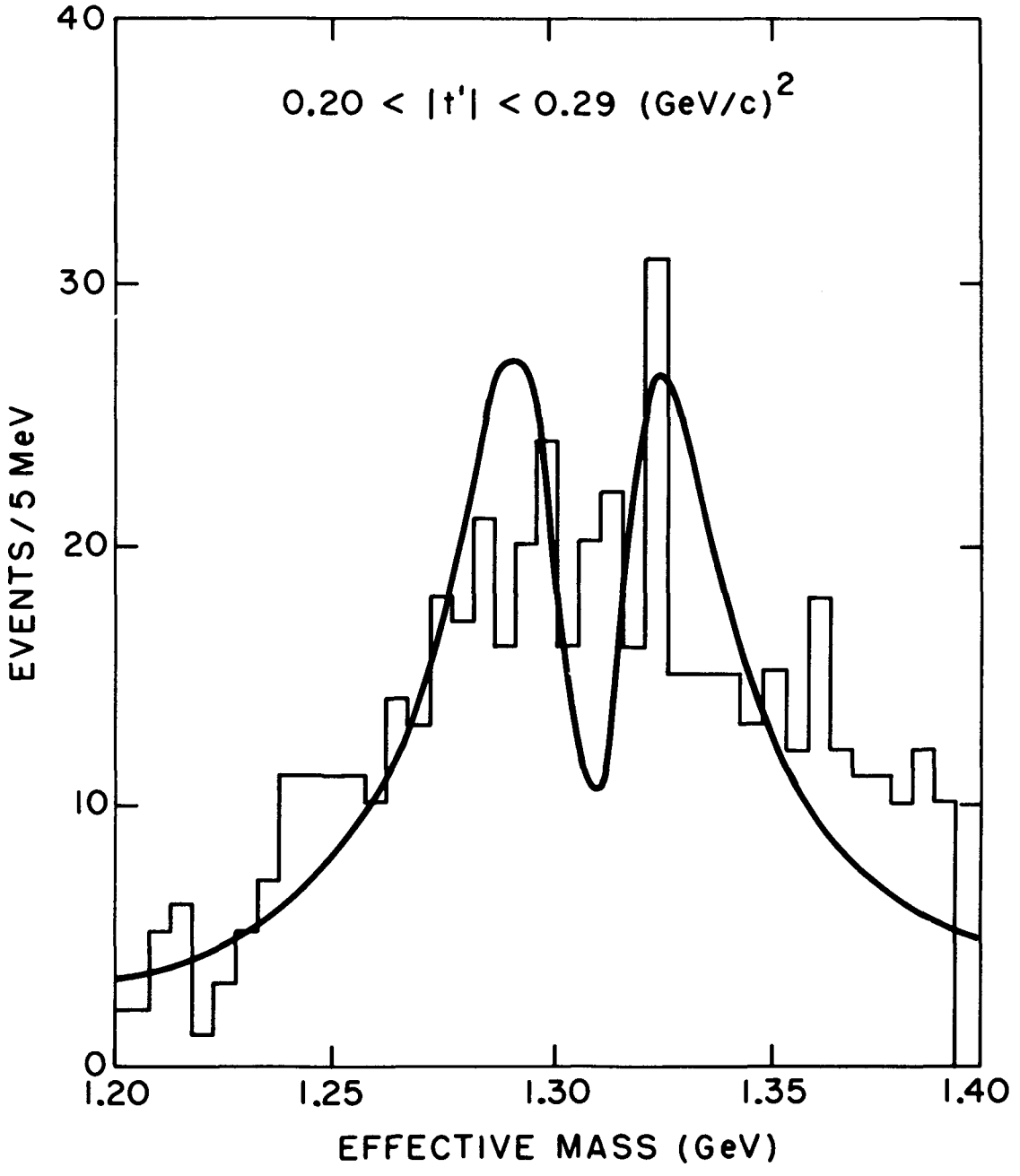
0.20 < |t'| < 0.29 (GeV/c)^2
EVENTS/5 MeV
0
10
20
30
40
1.20
1.25
1.30
1.35
1.40
EFFECTIVE MASS (GeV)

Figure 24

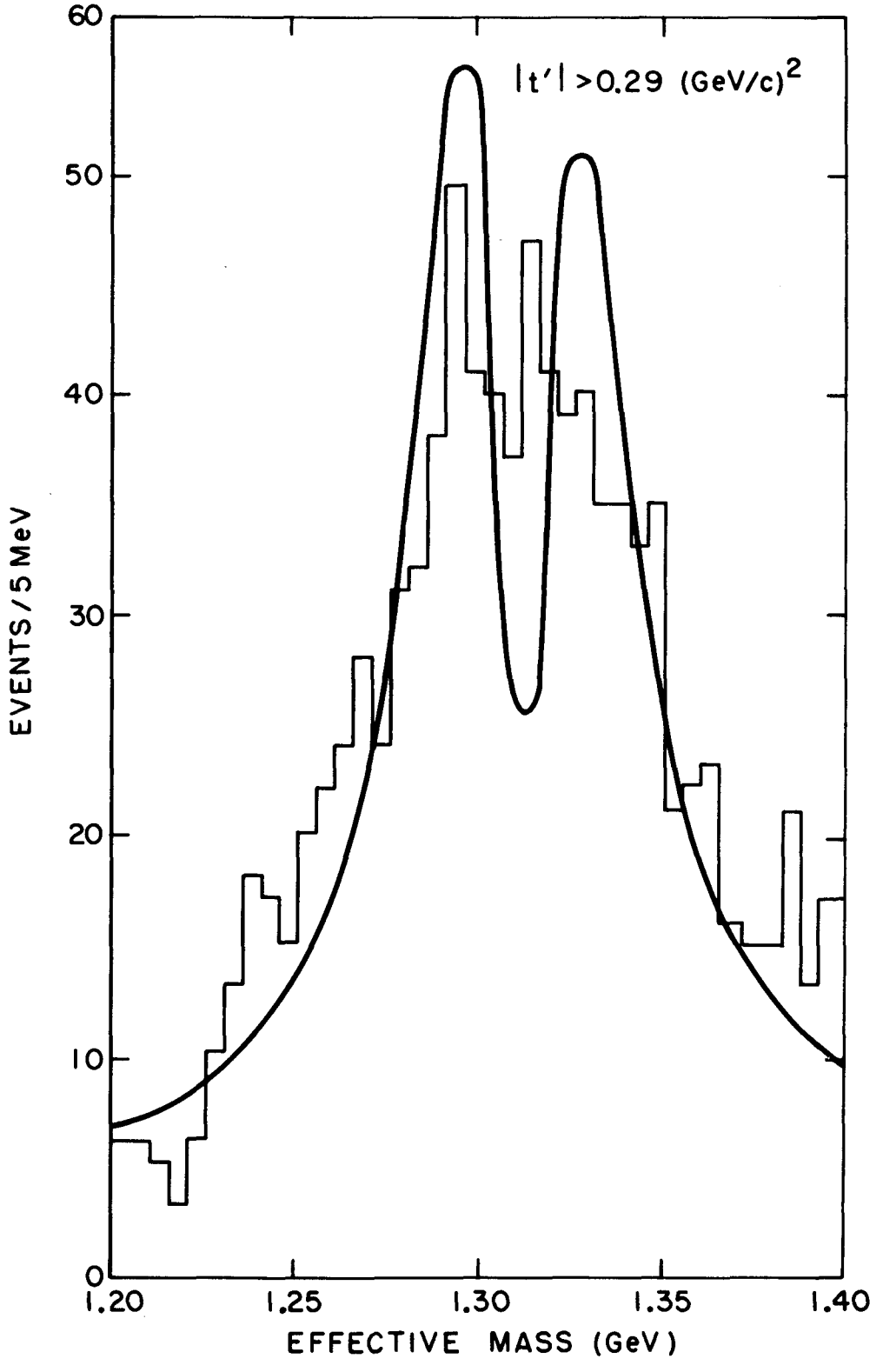
60
50
40
30
20
10
0
EVENTS / 5 MeV
|t'| >0.29 (GeV/c)²
1.20
1.25
1.30
1.35
1.40
EFFECTIVE MASS (GeV)

Figure 25

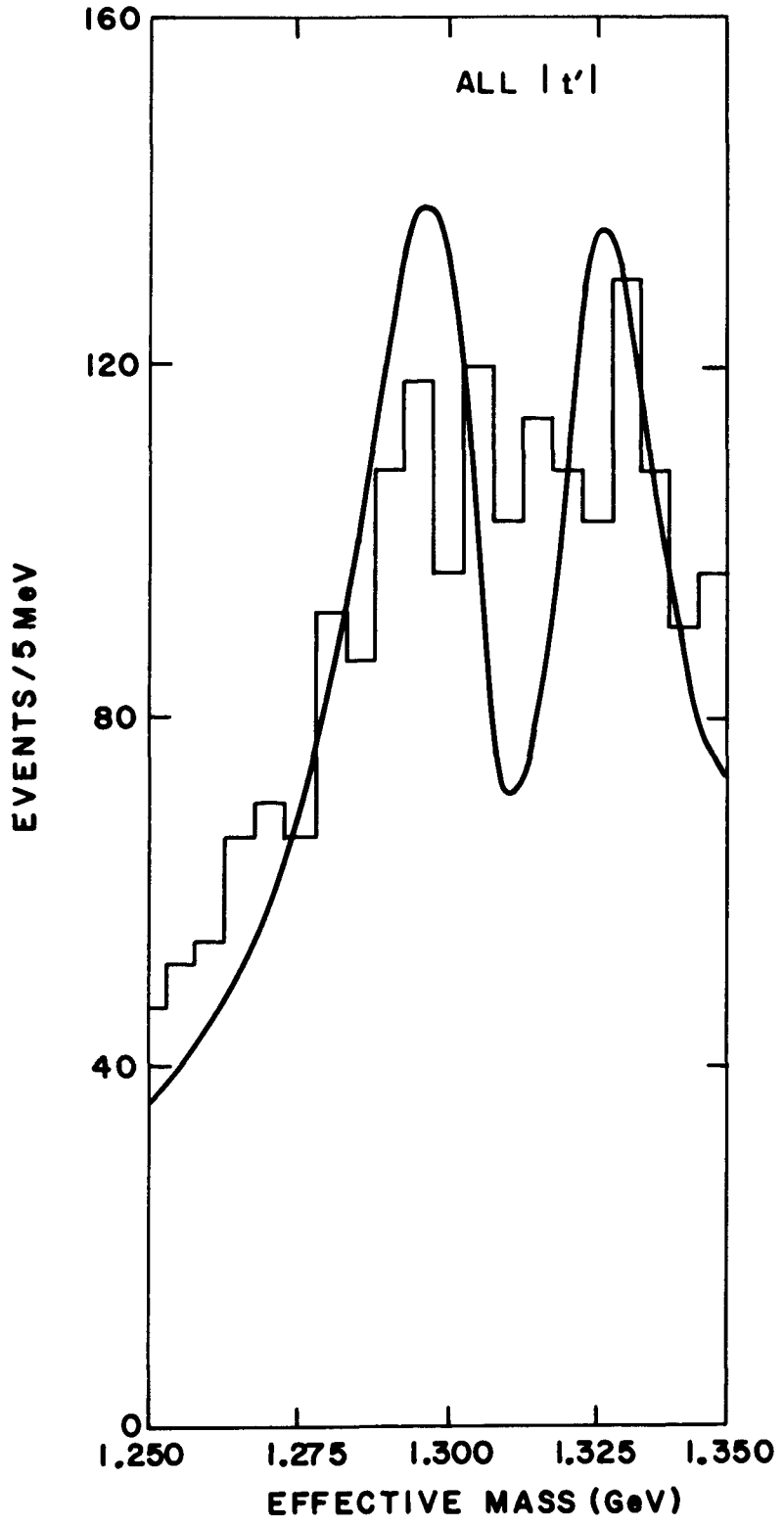
160
120
80
40
0
ALL |t'|
EVENTS/5 MeV
1.250
1.275
1.300
1.325
1.350
EFFECTIVE MASS (GeV)

Figure 26

76 degrees of freedom) by a single D-wave Breit-Wigner (and $\sim$ 10-20% background) and the previously reported CERN dipole type fit was rejected by 7.9 standard deviations.

Furthermore, we narrowed the mass region for all the data to the 1.25 to 1.35 GeV region in order to study the possibility of a dip in the A_2 mass spectrum independent of the exact dipole shape used. The results of the fit give a 6-standard-deviation rejection of the dipole form with the width and mass being free parameters.

Further analysis of the t' ranges $0 < -t' < 0.2$, $0.2 < -t' < 0.29$, $-t' > 0.29$ reveals that a similar D-wave Breit-Wigner is an excellent (χ^2 per degree of freedom $\simeq$ 1) fit to the data.

The dipole fits to the data in the t' regions $0. < -t' < .20$ and $-t' > .29$ in the $K_s^o K^-$ mass interval 1.2-1.4 GeV were improbable by 3.0 and 3.8 standard deviations respectively. The region $0.2 < -t' < 0.29$ has generated considerable interest. In the mass interval 1.2-1.4 GeV, the dipole fit was still improbable by 3 standard deviations, whereas the single D-wave Breit-Wigner gave an excellent fit.

CHAPTER VI

DIFFERENTIAL AND TOTAL CROSS SECTIONS

A. Introduction

Total and differential cross sections for the reaction

$$\pi^- P \rightarrow A_2^- \; P$$
$$\downarrow$$
$$K^o K^-$$

at 22.4 GeV/c and 23.9 GeV/c incident momenta are presented. We calculated the total and differential cross sections for the above momenta using the following effective mass cuts: (a) $1.2 < M(K_s^o K^-) < 1.4$ GeV, and (b) $1.1 < M(K_s^o K^-) < 1.5$ GeV. In Sections B through H we discuss the calculations and corrections which were used to derive the differential and total cross-sections. The dependence of the cross sections on momentum are discussed in Sections I and J. No corrections were made for the contributions to the cross section from events that fell outside the above mass intervals. The purpose of the cuts was to allow comparisons with other experiments[1,2] and also to minimize contributions which are very sensitive to the tails of the D-wave Breit-Wigner.

B. Determination of the Cross Sections

We determined the cross sections for the above reaction by calculating the differential cross sections $d\sigma/dt'$ (in units of $\mu b/(GeV/c)^2$) as a function of t', where

$$(1) \qquad \frac{d\sigma}{dt'} = \frac{N_{Events}(t')\ C.F.}{(\rho LN_o)(N_{\pi^-})\ Acceptance\ (t')\ (\Delta t')}$$

The various factors in the above expression for the differential cross section are defined below. We histogrammed the number of events as a function of t' and then determined the differential cross section by applying a series of corrections and normalizations to the data. We then proceeded to sum the differential cross section over t' to obtain the total cross section. Following is a list of the factors in Equation (1) which are used in the calculation of the differential cross sections:

(a) $N_{Events}(t')$ = the total number of events in a particular t' interval ($\Delta t'$) where the background events have been removed. (See Section C on background subtraction).

(b) ρLN_o = the number of scattering centers (target protons/cm^2) encountered by the incident beam expressed in terms of (1) the density of liquid hydrogen ρ = .0708 gm/cm^3, (2) the length of the hydrogen target L = 60.9 $\pm$ .2 cm, and (3) Avogadro's number $N_o = 6.023 \times 10^{23}$ atoms/gm atomic weight.

(c) N_{π^-} = the number of incident beam particles for the total running period. We note that the 22.4-GeV/c and 23.9-GeV/c runs had 8.885×10^9 and 24.691×10^9 incident beam particles respectively.

(d) Acceptance (t') = a correction for the acceptance of the spectrometer as a function of t'. (See Section D.)

(e) C.F. = an overall systematic correction to the data due to hardware and software inefficiencies and other losses in the spectrometer. Table 6a is a list of the systematic corrections to the data and their

Table 6a

Systematic Corrections to the Data and Their Associated Errors for the Reaction $\pi^- P \to A_2^- P$ at 22.4 and 23.9 GeV/c. (The overall correction factor C.F. is the product of the corrections listed below.)

$A_2^- \to K^0 K^-$

	P = 22.4 GeV/c	P = 23.9 GeV/c
Proton cut	1.03 ± .01	1.03 ± .01
Contamination of recoil proton peak	.97 ± .01	.96 ± .03
Program efficiency	1.20 ± .11	1.32 ± .13
Trigger efficiency††	1.21 ± .06	1.33 ± .07
Incident beam efficiency	1.022	1.022
Tape errors and other losses of data in the data-handling system	1.008	1.022
Empty target correction	.984 ± .013	.984 ± .013
e^- and μ^- beam contamination	1.036 ± .005	1.034 ± .005
Nuclear attenuation in the target	1.036 ± .01	1.036 ± .01
$K^0 K^-$ interactions in the target	1.05 ± .01	1.05 ± .01
$K^0 \to K_s^0$ branching ratio	2.0	2.0
Unseen K_s^0 branching ratio	1.452	1.452
Pion decay in spectrometer†	1.03 ± .01	1.03 ± .01
Events lost for $-t' > 1.0$ (GeV/c)^2*	1.02 ± .01	1.02 ± .01

† The acceptance correction includes the decay of the K^- in our spectrometer (see Sec. 6F, part b).

* Correction applied to total cross section, not differential cross section. This correction assumes the same exponential behavior of the differential cross section past $-t' = 1.0$ (GeV/c)^2.

††The correction factor arising from the misidentification of singles for doubles in the target veto system is incorporated in the correction for the trigger efficiency (See Sec. 6G).

associated errors. A detailed discussion as to the magnitude of the individual corrections and the errors is given in the text. The overall correction factor C.F. is the product of all the individual corrections.

(f) $\Delta t'$ = the t' interval in units of $(GeV/c)^2$ for which we calculate $d\sigma/dt'$.

B.1 Run Selection

Criteria were established to determine whether or not a particular run was to be incorporated in the data for the differential and total cross sections. The on-line monitoring of the experiment permitted us to detect hardware abnormalities such as: (a) problems with the magnet power supplies, (b) bad fast gates, (c) inefficient counters in any of the scintillation counter hodoscopes, (d) fluctuating trigger rates, etc. If these effects were significant, we would reject the run from any subsequent analysis. We also had a rigorous criterion for removing data which had inefficient spark chamber performance. As previously mentioned (Chapter III, Sec. C) the analysis program required at least four sparks to determine a track in both the X and Y views in both legs of the forward spectrometer. Ideally we would record six X and six Y position measurements in both legs. We adopted as a reasonable criterion for selecting usable cross-section data on the basis of spark chamber performance that any run which had two X or two Y gaps in the same leg of the spectrometer below 90% efficiency would be deleted from the data. Using this criterion, we deleted 11% (i.e. 98/873) of the data runs from the analysis of the differential and total cross sections.

C. Background Subtraction

In calculating the total and differential cross sections we attempted to remove background events from our A_2^- effective mass spectrum. We were interested in the background in the mass spectra as a function of very fine $-t'$ bins (where $t' = t - t_{min}$, and t is the negative of the four-momentum transfer squared). To accomplish this we first performed a maximum likelihood fit to the overall mass spectrum using a D-wave Breit-Wigner and a linear background. The parameters of the A_2 resonance found from that fit (listed below) were then used in doing a maximum likelihood fit to the effective mass spectra as a function of very fine t' bins (i.e. $|\Delta t'| = .02$ $(GeV/c)^2$). In doing the fits to the mass spectra in these narrow t' intervals, we assumed a linear background starting at threshold and allowed the slope of the background to be a free parameter. The following parameters were the results of a maximum likelihood fit to the overall mass spectrum (i.e. overall t'):

(a) effective mass peak = 1.320 GeV

(b) width = .105 GeV

(c) $R = 4.4$ $(GeV)^{-1}$

(d) threshold = .991 GeV.

It may be argued that the small number of events per t' bin (sometimes as few as 21 events, see Tables 6b-6e) are insufficient to determine the background accurately. To improve our statistics we proceeded to group together events from several t' bins. We then performed a maximum likelihood fit to the effective mass spectrum over this wider $|\Delta t'|$ range where the statistics were now several hundred events. The

Table 6b

Fitted events, fitted background, and fitted events and errors as a function of -t' for the reaction $\pi^- P \rightarrow A_2^- P$ at 22.4 GeV/c and $1.2 < M(K_s^o K^-) < 1.4$ GeV. ($A_2^- \rightarrow K^o K^-$)

$-t'$ $(GeV/c)^2$	Fitted Events	Fitted Background	Fitted Events and Error
.0 -.02	7.8	6.1	7.8 ± 3.7
.02-.04	19.0	7.5	19.0 ± 5.1
.04-.06	18.7	14.0	18.7 ± 5.7
.06-.08	25.4	7.3	25.4 ± 5.7
.08-.10	30.9	8.0	30.9 ± 6.2
.10-.12	36.4	3.9	36.4 ± 6.3
.12-.14	42.6	10.1	42.6 ± 7.3
.14-.16	40.1	2.5	40.1 ± 6.5
.16-.18	35.9	2.6	35.9 ± 6.2
.18-.20	28.8	6.4	28.8 ± 5.9
.20-.22	27.6	5.1	27.6 ± 5.7
.22-.24	24.2	2.6	24.2 ± 5.2
.24-.26	35.9	3.7	35.9 ± 6.3
.26-.28	14.8	11.5	14.8 ± 5.1
.28-.30	33.0	0.0	33.0 ± 5.7
.30-.35	60.9	0.0	60.9 ± 7.8
.35-.40	27.4	9.1	27.4 ± 6.0
.40-.45	29.6	0.0	29.6 ± 5.4
.45-.50	26.0	0.0	26.0 ± 5.1
.50-.60	25.6	7.8	25.6 ± 5.8
.60-.70	17.8	0.0	17.8 ± 4.2
.70-1.0	19.3	0.0	19.3 ± 4.4
	627.7	108.2	

Errors shown are statistical only.

Table 6c

Fitted events, fitted background, and fitted events and errors as a function of -t' for the reaction $\pi^- P \to A_2^- P$ at 22.4 GeV/c and 1.1 < $M(K_s^o K^-)$ < 1.5 GeV. ($A_2^- \downarrow K^o K^-$)

$-t'$ $(GeV/c)^2$	Fitted Events	Fitted Background	Fitted Events and Error
.0 -.02	9.2	11.8	9.2 ± 4.6
.02-.04	22.5	13.5	22.5 ± 6.0
.04-.06	22.2	25.8	22.2 ± 6.9
.06-.08	29.9	13.1	29.9 ± 6.6
.08-.10	36.6	15.4	36.6 ± 7.2
.10-.12	43.0	8.0	43.0 ± 7.1
.12-.14	50.2	18.8	50.2 ± 8.3
.14-.16	47.5	5.5	47.5 ± 7.3
.16-.18	42.4	5.6	42.4 ± 6.9
.18-.20	33.8	12.2	33.8 ± 6.8
.20-.22	32.5	9.5	32.5 ± 6.5
.22-.24	28.6	4.4	28.6 ± 5.7
.24-.26	42.3	6.7	42.3 ± 7.0
.26-.28	17.5	21.5	17.5 ± 6.2
.28-.30	39.0	0.0	39.0 ± 6.2
.30-.35	72.0	0.0	72.0 ± 8.5
.35-.40	32.4	16.6	32.4 ± 7.0
.40-.45	35.2	1.8	35.2 ± 6.1
.45-.50	30.7	1.3	30.7 ± 5.7
.50-.60	30.1	13.9	30.1 ± 6.6
.60-.70	21.0	0.0	21.0 ± 4.6
.70-1.0	22.8	0.2	22.8 ± 4.8
	741.4	205.6	

Errors shown are statistical only.

Table 6d

Fitted events, fitted background, and fitted events and errors as a function of -t' for the reaction $\pi^- P \rightarrow A_2^- P$ at 23.9 GeV/c and 1.2 < $M(K_S^0 K^-)$ < 1.4 GeV. ($A_2^- \rightarrow K^0 K^-$)

-t' $(GeV/c)^2$	Fitted Events	Fitted Background	Fitted Events and Error
.0 -.02	19.2	12.1	19.2 ± 5.6
.02-.04	28.6	17.3	28.6 ± 6.8
.04-.06	41.3	12.2	41.3 ± 7.3
.06-.08	36.3	18.3	36.3 ± 7.4
.08-.10	72.8	5.6	72.8 ± 8.8
.10-.12	66.4	11.8	66.4 ± 8.8
.12-.14	80.2	14.5	80.2 ± 9.7
.14-.16	70.3	8.8	70.3 ± 8.9
.16-.18	88.9	7.1	88.9 ± 9.8
.18-.20	87.2	1.8	87.2 ± 9.4
.20-.22	79.3	8.6	79.3 ± 9.4
.22-.24	79.9	1.7	79.9 ± 9.0
.24-.26	59.0	4.7	59.0 ± 7.9
.26-.28	60.2	7.8	60.2 ± 8.2
.28-.30	48.8	9.8	48.8 ± 7.6
.30-.35	116.6	6.4	116.6 ±11.1
.35-.40	103.2	18.9	103.2 ±11.0
.40-.45	60.9	2.3	60.9 ± 7.9
.45-.50	61.2	0.0	61.2 ± 7.8
.50-.60	77.3	6.9	77.3 ± 9.2
.60-.70	46.0	0.0	46.0 ± 6.8
.70-1.0	33.9	9.2	33.9 ± 6.6
	1417.5	185.8	

Errors shown are statistical only.

Table 6e

Fitted events, fitted background, and fitted events and errors as a function of -t' for the reaction $\pi^- P \to A_2^- P$ at 23.9 GeV/c and 1.1 < $M(K_s^0 K^-)$ < 1.5 GeV. ($A_2^- \downarrow K^0 K^-$)

-t' $(GeV/c)^2$	Fitted Events	Fitted Background	Fitted Events and Error
.0 -.02	22.7	22.3	22.7 ± 6.7
.02-.04	33.9	33.1	33.9 ± 8.2
.04-.06	47.8	22.2	47.8 ± 8.4
.06-.08	43.1	34.9	43.1 ± 8.8
.08-.10	86.7	12.3	86.7 ± 9.9
.10-.12	79.0	22.0	79.0 ± 10.0
.12-.14	95.5	27.5	95.5 ± 11.1
.14-.16	83.8	17.2	83.8 ± 10.0
.16-.18	105.9	14.1	105.9 ± 11.0
.18-.20	102.7	3.3	102.7 ± 10.3
.20-.22	94.5	16.5	94.5 ± 10.5
.22-.24	95.2	2.8	95.2 ± 9.9
.24-.26	70.0	9.0	70.0 ± 8.9
.26-.28	71.9	15.1	71.9 ± 9.3
.28-.30	58.3	18.7	58.3 ± 8.8
.30-.35	138.9	12.1	138.9 ± 12.3
.35-.40	122.9	36.1	122.9 ± 12.6
.40-.45	72.7	5.3	72.7 ± 8.8
.45-.50	73.0	0.0	73.0 ± 8.5
.50-.60	92.3	12.7	92.3 ± 10.2
.60-.70	54.7	1.3	54.7 ± 7.5
.70-1.0	40.3	17.7	40.3 ± 7.6
	1685.8	356.2	

Errors shown are statistical only.

number of fitted events and fitted background counts in the wider $|\Delta t'|$ range was equal to the sum of the fitted events and the sum of the fitted background events over the finer intervals. We conclude that the technique of maximum likelihood gives an accurate estimate of the background in the effective mass spectra corresponding to small t' intervals albeit the small statistics. We thus proceeded to remove the background events from our calculation of the differential cross sections.

From Tables 6b-6e we find that the ratio of fitted background to fitted events is high at small t' (i.e. $0.0 < |t'| < .08$) $\sim$ 48%. This is due partly to the fact that the signal in the differential cross section is small at low $|t'|$, and partially because the nonresonant background is highly diffractive and is consequently large at low $|t'|$. The statistical uncertainty associated with the number of fitted events per specific $|t'|$ bin was coupled with the statistical uncertainty in the number of fitted background events per bin. We estimated the statistical uncertainty in the number of fitted events per given $|t'|$ bin by taking the square root of the total number of events per bin as the statistical uncertainty in the number of fitted events.

We tested the sensitivity of the number of fitted events as a function of the fixed parameters previously obtained from a fit to the overall effective mass spectrum. We did this by varying the mass, width, and R parameters by one standard deviation respectively. The resultant change in the fitted events was of the order of 2%, which is small compared to a minimum statistical error of 8% associated with the bin that has the largest number of events.

D. Corrections to the Cross-Sections for the Acceptance of the Spectrometer

A Monte Carlo technique was used to generate a sample of A_2^- events. A generated event was traced through the system to determine whether it would survive the various predetermined geometric, aperture, trigger and kinematic requirements. Monte Carlo programs were run using the two different momenta (22.4 GeV/c and 23.9 GeV/c). The generated events were a function of the four kinematic variables t', m, cosθ, and φ, where $t' = t - t_{min}$, m is the effective mass of the resonance, and θ and φ are the decay angles of the A_2 as defined in the Gottfried-Jackson frame.[17] We corrected the differential cross sections for the acceptance of the apparatus by integrating the observed distributions in m, cosθ, and φ, and correcting for the acceptance of the spectrometer as a function of t'. From Fig. 27 we can see that the acceptance is a smooth function of -t', being almost flat at low t' (i.e. $0 < -t' < .30$ $(GeV/c)^2$), and falling off slowly for $.3 < -t' < 1.0$ $(GeV/c)^2$.

E. Details of the Monte Carlo Generation of an Event

The momentum of the incident pion was generated according to a Gaussian of a width $\sigma \approx .200$ GeV/c (equivalent to the incident beam width) and subsequently a target interaction point was generated. We used the differential cross section with a forward dip simulating the data at small four-momentum transfer squared, and an exponential falloff

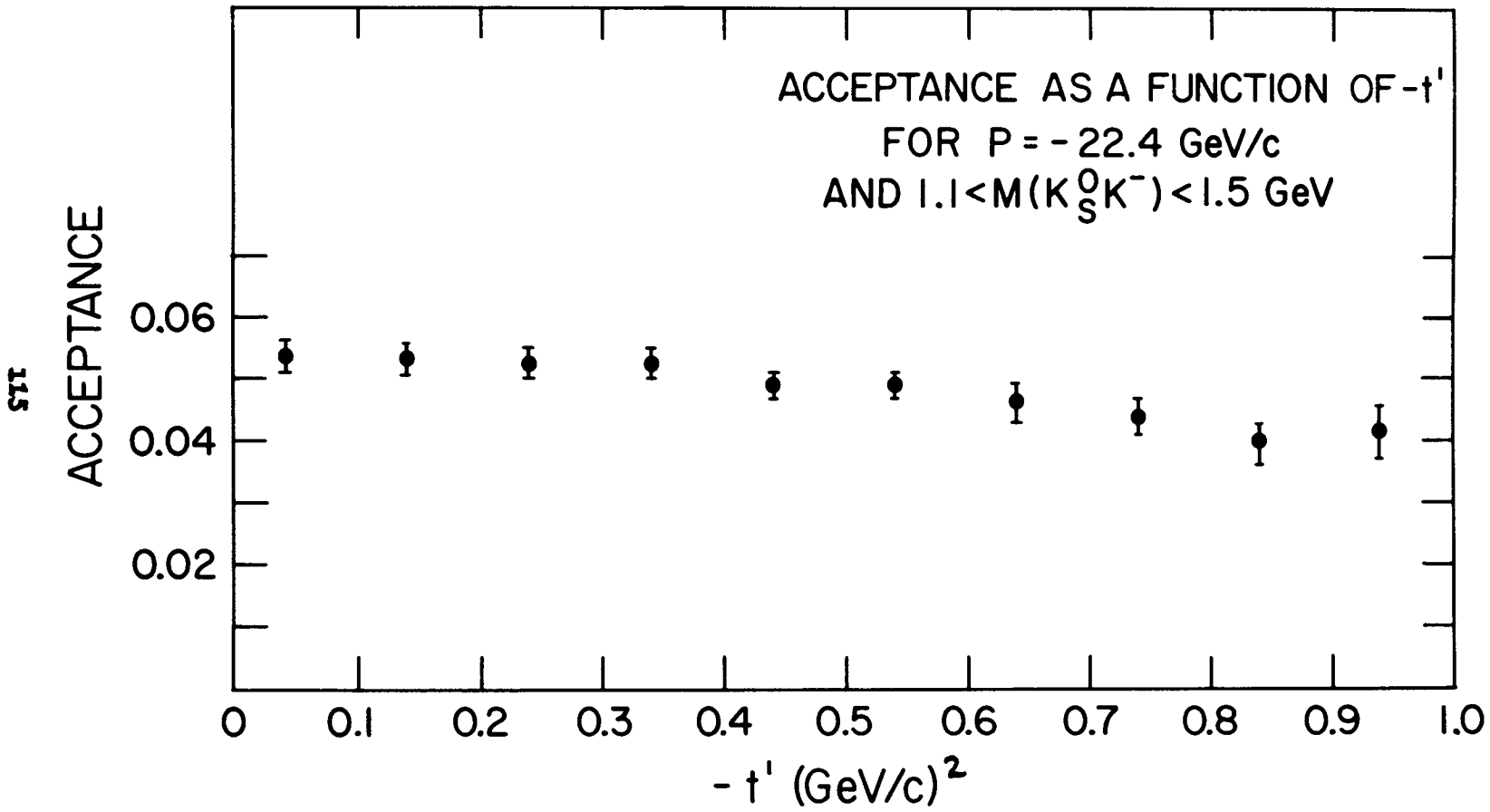
ACCEPTANCE AS A FUNCTION OF -t'
FOR P = -22.4 GeV/c
AND 1.1<M(K^0_SK$^-$)<1.5 GeV
ACCEPTANCE
0.06
0.04
0.02
0
0.1
0.2
0.3
0.4
0.5
0.6
0.7
0.8
0.9
1.0
- t' (GeV/c)^2

Figure 27

of approximately $e^{4.0t'}$ for $|t'| > .10$ $(GeV/c)^2$. The mass distribution of the A_2 was taken to be a Gaussian* with a width of 110 MeV. The angular distribution in the Gottfried-Jackson frame (see Chapter VII) used was:

$$I(\theta,\phi) \alpha \cos^2\theta \sin^2\theta \sin^2\phi .$$

To maximize our resolution, the Z†-decay region of the K_s^o was restricted to be (a) downstream of scintillation counter "A" (this was part of the 1→3 trigger requirement) and (b) upstream of the first spark chamber (Z = 26.0"). The decay region cuts on the K_s^o resulted in the largest single loss in acceptance. Of the generated events, 78% were eliminated because the K_s^o decayed either in the target or downstream of the first spark chamber.

The average acceptance at 22.4 and 23.9 GeV/c was 5.19 $\pm$ .03% and 5.39 $\pm$ .03% respectively. The errors on the acceptance are statistical only. We also estimate a 10%** systematic error on the overall acceptance. We note that these numbers indicate a rather small spectrometer acceptance for A_2 events. However, the acceptance for those events that survive the decay volume cut is $\approx$ 25%.

---

* We note that the Monte-Carlo acceptance does not depend critically on the assumed shape of the A_2 or its distribution. The choice of generating the mass distribution as a Gaussian was to match the statistics of the data and the Monte-Carlo in a particular mass interval.

† Coordinate along the beam line.

**See Section F.

The Monte Carlo program incorporated subroutine "BEND" which projected the final decay products of the A_2^-, namely the π^+, π^-, and K^-, through our spectrometer magnet. In the program we required that the projected decay products of the A_2^- intersect three separate scintillation counters in hodoscope H4 located at Z = 314.2" (each counter being 2.5" wide). We also vetoed any generated events whose tracks intersected scintillation counter "B", a small veto counter (5.2" wide x 5.2" high x 1/8" thick) which was installed downstream of scintillation counter hodoscope H4 to veto noninteracting beam particles.

Various aperture cuts corresponding to the appropriate dimensions of the apparatus were applied. Generated events which did not traverse the magnet aperture were killed. The cuts on the magnet aperture were made both at the magnet entrance and at the magnet exit. We further insisted that any projected track be within the upstream spark chambers and also within scintillation counter hodoscope H4.

F. Sensitivity of the Spectrometer Acceptance to Various Cuts

We investigated the sensitivity of the spectrometer acceptance to various geometric cuts. We varied the cuts to determine the effects on the overall acceptance and to estimate the magnitude of the systematic error associated with these cuts.

(a) Since the largest fraction of generated events are lost in the decay region cuts on the K_s^o, we proceeded to vary these cuts to see what effect they had on the overall acceptance. Table 6f shows the overall acceptance for different Z-decay region cuts on the K_s^o. We note

Table 6f	
Decay region for K_s^o *	Overall acceptance at 23.9 GeV/c
$14.0" \leq Z(K_s^o) \leq 26.0"$	5.3 ± .1%
$13.85" \leq Z(K_s^o) \leq 26.15"$	5.5 ± .1%
$14.15" \leq Z(K_s^o) \leq 25.85"$	5.2 ± .1%

Table 6g	
Z decay region for K^-	Overall acceptance at 23.9 GeV/c
$Z(K^-) \geq 238.0"$	5.3 ± .1%
$Z(K^-) \geq 190.0"$	5.4 ± .1%

Table 6h	
Y cuts on magnet aperture	Overall acceptance at 23.9 GeV/c
$-9.22" \leq Y \leq +9.22"$	5.30 ± .10%
$-9.0" \leq Y \leq +9.0"$	5.27 ± .10%

Table 6i	
X cuts on magnet aperture	Overall acceptance at 23.9 GeV/c
$-33.0" \leq X \leq 15.0"$	5.3 ± .1%
$-30.0" \leq X \leq 12.0"$	5.2 ± .1%

* The first entry on Tables 6f-6i denotes the cut used in the Monte Carlo program for determining the acceptance of the spectrometer.

that our resolution in Z (i.e. the uncertainty in the Z position of the K_s^o vertex) is approximately .30". We thus introduce ≈ a 4% systematic uncertainty in the acceptance due to our finite Z position resolution of the K_s^o vertex.

(b) In our Monte-Carlo program we demanded that any generated K^- (i.e. $A_2^- \rightarrow K^oK^-$) that decayed into a $\mu^- + \bar{\nu}_\mu$ pair* upstream of the last gap of spark chamber module I (Z = 238.0") be rejected. This criterion was chosen because the pattern recognition program would have sufficient x and y position measurements (i.e. four) to be able to reconstruct the track if the K^- had not decayed upstream of this point. If we had chosen a criterion that would reject any generated events where the K^- had decayed before the last gap in spark chamber module C (Z = 190.0"), the resulting acceptance would change. Table 6g indicates what the overall acceptance would be for the two different decay region cuts on the K^-. We note that the change in acceptance is ≃ 2%. We therefore introduce ≈ a 2% systematic error in the acceptance due to the uncertainty in the correction for a K^- decaying in our spectrometer.

(c) We demanded that the x and y positions of the generated tracks be within the gap of the 48D48 magnet. The vertical Y cuts on the magnet aperture were applied at the magnet shield (Z = 66.0") and at the magnet exit (Z = 140.55"). Table 6h indicates the acceptance for two different Y cuts on the magnet aperture. The X position cuts for the

---

* The decay length of a 10-GeV/c K^- is 2957". At Z = 238.0" we expect that 7.7% of the K^-'s that were produced in the target will have decayed into a $\mu^- + \bar{\nu}_\mu$ pair.

Monte-Carlo generated tracks were placed at: (1) the magnet shield, (2) the center of the 48D48 magnet, (3) at the magnet exit. Table 6i indicates the acceptance for two different x-position cuts placed at these three points. The systematic error in the acceptance due to the uncertainty in the correction for cuts on the magnet aperture is approximately 2%.

(d) We examined the sensitivity of the acceptance of the spectrometer to cuts placed in the Monte Carlo program on the separation of the decay products of the A_2^- at: (1) the proportional wire chamber positioned at Z = 44.5", and (2) the center of spark chamber module "A" located at Z = 33.0". We compared the separations of the decay products of the A_2^- at these two points between the Monte-Carlo generated events and the real data. We did this to: (1) gain insight into the effect of the cluster mode (see Chapter II, Sec. G) trigger of the PWC on our acceptance for real events, and (2) search for the possibility of the pattern recognition program running into difficulties in the reconstruction of tracks for events where the decay products of the A_2^- had not separated sufficiently in spark chamber module "A".

We empirically determined the minimum X separation of the decay products of the A_2^- at the PWC and the minimum X and Y separations of the decay products at the center of spark chamber module "A". This was done by adjusting the separation requirements of the π^+, π^- and K^- at the "A" chamber and the PWC such that the average separations of the particles looked the same both in the Monte-Carlo program and the data. The empirically determined X and Y minimum separations of the particles in the middle of spark chamber module "A" (Z = 33.0"), which were determined as suitable cuts, are given below:

(1) The minimum X-separation between the π^+ and K^- was .085".

(2) The minimum X-separation between the π^- and K^- was .085".

(3) The minimum X-separation between the π^+ and π^- was .150".

(4) The minimum Y-separation between the π^+ and K^- was .120".

(5) The minimum Y-separation between the π^- and K^- was .085".

(6) The minimum Y-separation between the π^+ and π^- was .120".

Removing the X-separation cuts in spark chamber module "A" results in a change in the overall acceptance of from 5.3 $\pm$ .1% to 5.6 $\pm$ .1%. Removing the Y-separation cuts in spark chamber module "A" results in a change in the overall acceptance from 5.3 $\pm$ .1% to 6.4 $\pm$ .1%. If these cuts are removed, then the separation of the particles in spark chamber module "A" looks considerably different for the Monte-Carlo generated events and the real data. To estimate the systematic error associated with the above separation requirements, we proceeded to decrease the minimum separation requirements on the particles in spark chamber module "A" by .025"; the resultant acceptance changed from 5.3% to 5.7%. We therefore introduce $\approx$ a 7% systematic error associated with the cuts on the separation of the particles in spark chamber module "A".

A similar analysis comparing the separation of the particles at the proportional wire chamber between the Monte Carlo and the data was performed. The systematic error associated with the empirically determined separations was $\approx$ 5%.

We folded in the individual systematic errors associated with the above effects in quadrature. The calculated overall systematic error associated with the acceptance of the spectrometer was $\approx$ 10%.

G. Overall Systematic Correction Factor C.F.

1. Proton Cut

Due to our finite resolution (σ = 85.4 $\pm$ 1.3 MeV) of the mass of the recoiling proton, we insisted that the missing mass for an A_2^- event fall between .70 and 1.1 GeV (i.e. $\pm 3\sigma$ from the center of the proton peak). We applied a correction to the cross sections for those events that are associated with recoiling protons that lie outside our missing mass interval (i.e. events that lie on the tails of the Gaussian fit to our missing mass spectrum). For both sets of data (i.e. P = 22.4 and 23.9 GeV/c) the fraction of events in the Gaussian fit to the missing mass spectra below .7 GeV and above 1.1 GeV was 3 $\pm$ 1%.

2. Contamination of Recoil Proton Peak

In determining the total and differential cross sections for

$$\pi^- P \rightarrow A_2^- + P$$
$$\downarrow$$
$$K^o K^-$$

we restricted ourselves to events with proton recoils. We looked at the $K_s^o K^-$ effective mass spectra ($1.1 < M(K_s^o K^-) < 1.5$ GeV) for those events which had a missing mass just above our proton cut (i.e. 1.1 < missing mass < 1.2 GeV). The effective mass spectra, although limited in statistics, looked like A_2^- events rather than background. Events associated with recoil masses just above our proton cut look like A_2's. This implies that events that are associated with recoils that leak into our missing mass cut will look like A_2's and not background, and therefore must be subtracted separately. We corrected for this effect by examining the background under our proton peak. A single Gaussian fit plus a linear

background was performed on the missing mass spectra for both running periods. The results of the fit are shown in Table 6j. The fitted background over events ratio was performed over our proton cut, .70 < missing mass < 1.1 GeV. We therefore reduced the cross sections by factors of .97 and .96 for the 22.4 and 23.9 GeV/c runs respectively. The errors in Table 6a associated with the contamination of the proton peak are the results of uncertainties in the fitting procedures.

3. Program Efficiency

To measure the program efficiency we asked the following: For A_2^-'s that are created in the target and successfully traverse the apparatus, how many of these events does our analysis program recognize and record? The pattern recognition program (BEADS) constructed tracks out of sparks, since this was often complicated by factors such as: (a) high beam rates giving rise to extra tracks, (b) lack of separation of sparks in the forward leg of the spectrometer upstream of the analyzing magnet, etc.; we found as expected that the program efficiency was less than 100%.

To determine the program efficiency we adopted the following procedure: We let the off-line program reconstruct A_2^- events from our summary (KOMP) tapes. These tapes had all the relevant raw data corresponding to events which satisfied the A_2^- topologies. In addition we required that the found A_2^- event satisfy certain geometric and kinematic cuts. These included: (1) a negative prong plus a neutral vee in the mass region .485-.510 GeV (assuming the neutral vee decayed into $\pi^+\pi^-$) coming from a common point in the target; (2) the Z-decay region of the neutral vee be between 14 and 26 inches (downstream of scintillation counter

Table 6j

	P = 22.4 GeV/c	P = 23.9 GeV/c
Mass	943.5 $\pm$ 3.8 MeV	950 $\pm$ 3.5 MeV
Resolution	σ = 81.2 $\pm$ 2.9 MeV	σ = 84.7 $\pm$ 1.8 MeV
Background cutoff	1034 $\pm$ 15 MeV	1005 $\pm$ 29 MeV
$\frac{\text{Background}}{\text{events}}$	$\frac{30.5}{961.8} \sim 3 \pm 1\%$	$\frac{101}{2378} \sim 4 \pm 3\%$
$\chi^2/\nu-k^{\dagger}$	30.5/25	22.5/25

† $\chi^2/\nu-k$ is the value of Chi-square per degree of freedom.

"A" and upstream of the first spark chamber); (3) the reconstructed effective mass of the $K_s^o K^-$ be between 1.1 and 1.5 GeV; (4) the missing mass be between .50 and 1.2 GeV.

We then proceeded to analyze the tapes and find A_2^- events. When an event was found that satisfied the above criteria, the coordinates of all the sparks associated with the tracks of that event were stored away. We then searched for the next event and, upon finding it, the coordinates of the sparks associated with the π^+, π^- and K^- for this event were stored in a table. In addition, these sparks were removed from the data and replaced by the stored sparks from the previous event. Then this data was reanalyzed to see if the program could find the previous event with the background associated with the current event.

The major losses were due to merging tracks, especially in the upstream arm of the spectrometer, and confusion in combining two-dimensional views into three-dimensional tracks. The results obtained for the program efficiencies using the two samples of data are shown in Table 6k. We note a factor of two increase in the beam rate for the higher momentum run. Since an increase in beam rate is associated with higher backgrounds, we would conclude that the program would have more difficulty in reconstructing events and correspondingly give rise to a lower program efficiency.

We have no quantitative way of calculating the systematic error associated with the program efficiency. However, we note that the program efficiency decreased by only 7% when the beam rate doubled. From the variation in the program efficiency as a function of beam rate, we

Table 6k

Momentum in GeV/c	Program Efficiency = $\frac{\text{number refound}}{\text{number found}}$
P = 22.4	$\frac{798}{961} = 83 \pm 1.2\%$
P = 23.9	$\frac{926}{1216} = 76 \pm 1.2\%$

(The above errors on the program efficiency are statistical only. We estimate an $\simeq$ 8% systematic error associated with the program efficiency.)

estimate that the systematic error associated with the program efficiency is approximately 8%.

4. Trigger Efficiency

Several factors were involved in determining the (1→3) trigger efficiency of our spectrometer. We discussed the effect of the target veto counter on our 1→3 trigger (see Chapter II, Sec. D). We calculated that we would fail to trigger on 8 $\pm$ 2% of the events due to the misidentification by the target veto system of singles (in the target veto counter) for doubles.

Another factor which contributed to our trigger efficiency was the trigger efficiency of the proportional wire chamber on three forward-going charged particles. During the course of the experiment we monitored the efficiency of the proportional wire chamber on beam particles traversing the system. The efficiencies of the proportional wire chamber on singles were $\approx$ 99 and 97% for the 22.4 and 23.9 GeV/c runs respectively. We note that the slightly lower efficiency in the higher momentum run was probably due to higher beam rates (i.e. dead time losses) in the higher momentum run. The above efficiencies are for singles whereas our trigger requirement demanded three clusters in the proportional wire chamber. It is likely that the efficiency of the proportional wire chamber per particle on triples is higher than the efficiency on singles, since dead time effects should be limited to wires that are directly in the beam. We estimate that the efficiency on singles for wires outside the beam region is 99.5 $\pm$ .5% and that the efficiency on triples is the cube of the singles efficiency. Under

these assumptions we estimate that the trigger efficiency of the proportional wire chamber on A_2 events is $\simeq 98 \pm 2\%$.

We calculated the trigger efficiency of scintillation counter hodoscope H4 on A_2 events. We established a special trigger to monitor the efficiency of the 62 counters in scintillation counter hodoscope H4. This trigger required the following: (a) a single track in the incident beam hodoscope system (π^-), (b) three wire clusters in the proportional wire chamber, (c) no count in the magnet veto counter (MC), and (3) three in-time tracks in scintillation counter hodoscope H4' located slightly downstream of H4. If the above trigger requirements were satisfied, the analysis program would project the tracks as determined by the spark chambers from the downstream leg of the spectrometer into the appropriate counter in H4 and check whether or not that counter detected the event. We thus had an efficiency measurement for each of the 62 counters in scintillation counter hodoscope H4. We used these efficiency numbers in conjunction with the spatial distribution (i.e. the distribution in X of the π^+, π^- and K^-) in H4 for A_2 events to establish a weighted efficiency for detecting one of the decay products of an A_2 (i.e. a π^+, π^- or K^-).

The weighted efficiency for detecting a single particle in H4 is defined to be:

$$\bar{E} = \frac{\sum_i N_i E_i}{\sum_i N_i}$$

where N_i is the number of counts in an individual counter (i.e. the weight), E_i is the efficiency of a particular counter as defined above, and $\bar{E}$ is the weighted efficiency. We recall (see Chapter II, Sec. I) that our trigger requirement demanded three or more charged particles in H4. To get an estimate of the trigger efficiency of scintillation counter hodoscope H4 on detecting three particles, we cubed the above weighted efficiency.

The calculated weighted efficiencies for detecting a single particle from an A_2 event in scintillation counter hodoscope H4 were 97.2 $\pm$ 1% and 94.1 $\pm$ 1% for the 22.4 and 23.9 GeV/c runs respectively. The resultant weighted efficiencies (obtained by cubing the weighted efficiency on singles) for detecting three charged particles from the decay of the A_2^- in H4 were 91.8 $\pm$ 3% and 83.3 $\pm$ 3% for the 22.4 and 23.9 GeV/c runs respectively. The errors associated with the H4 trigger efficiency are dominated by the uncertainty in the absolute efficiency of the individual counters due to:

(a) the statistical uncertainty in the efficiency of the counter. The maximum statistical uncertainty associated with the counter that had the fewest number of counts was $\pm$1.3%. A more typical number for the statistical error in the efficiency was $\pm$.3%.

(b) imprecise alignment of scintillation counter hodoscope H4.

We estimate that the effect on the weighted efficiency for single particles due to the uncertainty in the efficiency of the individual counters is $\simeq$ 1% and that the error associated with the trigger efficiency on triples is three times that or $\simeq$ 3%.

The overall trigger efficiency of our spectrometer on A_2 events is the product of the trigger efficiencies for (a) the target veto counter (92 $\pm$ 2%), (b) the proportional wire chamber (98 $\pm$ 2%), and (c) the H4 trigger efficiency (91.8 $\pm$ 3% and 83.3 $\pm$ 3% for the 22.4 and 23.9 GeV/c runs respectively). Since the errors in the trigger efficiencies for the above effects were uncorrelated, we added the errors in quadrature. The resultant trigger efficiency of the apparatus for A_2 events was 82.8 $\pm$ 4.1% and 75.1 $\pm$ 4.1% for the 22.4 and 23.9 GeV/c runs respectively. We have neglected the contribution to the overall trigger efficiency from scintillation counter hodoscope H4' since the individual counters in H4' were virtually 100% efficient.

5. Incident Beam Efficiency

Beam particles were permitted to trigger the apparatus at the rate of one per AGS pulse; these were referred to as profile triggers. The software labeled a beam particle to be "good incident" if a single, in-time beam track showed up in the X planes of scintillation counter hodoscopes H1-H3.

Due to possible rate and hardware effects in the incident beam system, we found the ratio of $\frac{\text{good incident}}{\text{triggers}}$ for profile triggers to be less than unity. This indicated that we sometimes triggered on events that were not good incident (i.e. multiplicities, or blanks). These should not have been counted as true incident beam particles. We therefore reduced the beam by the above ratio. Table 6a indicates this ratio for the two momenta.

6. Corrections due to Parity Errors on the Data Tapes, and Losses of Data in the Data-Handling System.

We examined the ratio of two relevant quantities: (a) the total number of 1→3 triggers that the analysis program found, and (b) the total number of 1→3 triggers that the scalers recorded. If there were no parity errors on the tapes or any other losses of data in the data-handling system, and the scalers shut off properly, the ratio of (a) to (b) would be unity. However, the results for the two different running periods were:

$$\frac{\text{Total \#(1→3) Triggers Program}}{\text{Total \#(1→3) Triggers Scaler}} = \frac{437573}{441360} = .992 \quad (P = 22.4 \text{ GeV/c})$$

$$\frac{\text{Total \#(1→3) Triggers Program}}{\text{Total \#(1→3) Triggers Scaler}} = \frac{1351036}{1381960} = .978 \quad (P = 23.9 \text{ GeV/c})$$

We therefore corrected for this loss. (See Table 6a.)

7. Empty Target

The experiment was performed using a target consisting of a cylindrical cell full of liquid hydrogen. Special runs were taken where the liquid hydrogen was removed. We analyzed events that were obtained with the target empty. An event qualified as a good "cut" event if the event fitted the topology of one negative prong plus a neutral vee in the mass region .485-.510 GeV (assuming that the neutral vee decayed into $\pi^+\pi^-$) coming from a common point in the target, and the missing mass associated with that event qualified as a proton. (See Chapter VI, Sec. G1.)

For the target empty runs we had:

$$\frac{\text{Number } A_2^- \text{ (cut events)}}{\text{beam}} = \frac{2}{510\text{x}10^6}$$

For some typical target full runs:

$$\frac{\text{Number } A_2^- \text{ (cut events)}}{\text{beam}} = \frac{97}{407\text{x}10^6}$$

Therefore the

$$\frac{\text{target empty rate}}{\text{target full rate}} = \frac{.00392}{.23833} \sim 1.6\%$$

$$\frac{\text{target empty rate}}{\text{target full rate}} = 1.6 \pm 1.4\%$$

We note that the target empty correction serves to decrease the total cross section. The error associated with the correction is statistical only.

8. e^- and μ^- Beam Contamination

The μ^-/π^- ratio of the negative beam measured using a beam stop of 2.1m of iron behind hodoscope H_4' varied from 4.5% at 8 GeV/c to 3.5% at 20 GeV/c. The e^-/π^- ratio, measured by a Columbia group using a lead glass Cerenkov counter, varied from 6% at 8 GeV/c to .15% at 20 GeV/c.[18] We therefore reduced the beam by a factor of $.965 \pm .005$.

9. Nuclear Attenuation in the Target

If a beam particle interacted in the target and did not create an A_2^-, then that beam particle could no longer contribute to the A_2 cross section. We therefore corrected the beam for this loss.

At 23 GeV/c incident momentum the total cross section for $\sigma_{total}(\pi^- p) \approx 25$ mb[25] and $\sigma_{elastic}(\pi^- p) \approx 4$ mb.[25] We estimate that approximately half the elastically scattered pions are still available for A_2 production. We can thus write $\sigma_{effective}(\pi^- p) \approx \sigma_{inelastic}(\pi^- p) + \frac{1}{2}\sigma_{elastic}(\pi^- p)$, and therefore $\sigma_{effective}(\pi^- p)$ is $\approx$ 23 mb at 23 GeV/c. Then the percentage of beam lost due to nuclear attenuation in the target is given below.

$$\frac{N_{events}}{N_{incident}(\pi^-)} \approx \rho L N_o \times \sigma_{effective}(\pi^- p) = .0597 = 5.97\%.$$

Therefore in traversing two feet of liquid hydrogen approximately 5.97% of the incident pions will have interacted. At the beginning of the target we have 100% of the beam; at the end of the target we have 94.03% of the beam.

The effective beam available decreases approximately linearly as we traverse the target. The detection efficiency for A_2's is also changing. The Monte-Carlo calculation of the detection efficiency did not include nuclear attenuation in the target. Thus to properly normalize the amount of beam available for creating an A_2, we calculated a weighted average of the available beam with the detection efficiency properly folded in. The calculated value for the weighted effective beam was $96.5 \pm 1\%$. We estimate a 1% error in this calculation due to the possible misinterpretation of the number of elastically scattered events contributing to the nuclear attenuation in the target.

10. K^oK^- Interaction in the Target

For our data sample the mean momenta for the K_s^o and K^- are $\simeq$ 13 GeV/c and $\simeq$ 10 GeV/c respectively. If we assume that the A_2^- is created in the middle of the target, then the K^o and K^- would each traverse on average one foot of liquid hydrogen.

From isotopic spin arguments one can show that the total cross section $\sigma_{total}(K^oP) = \sigma_{total}(K^+N)$. We then get

$$\sigma_{total}(K^+N) = \sigma_{total}(K^oP) \sim 18 \text{ mb}^{(26)} \text{ (at 13 GeV/c)}$$

and $\sigma_{total}(K^-P) \simeq 25 \text{ mb}^{(26)}$ (at 10 GeV/c)

Also: $\sigma_{elastic}(K^+N) \simeq 3.5 \text{ mb}^{(27)}$ (at 13 GeV/c)†

$$\sigma_{elastic}(K^oP) \simeq 3.5 \text{ mb}$$

$$\sigma_{elastic}(K^-P) \simeq 4.0 \text{ mb}^{(27)} \text{ (at 10 GeV/c)}$$

As in Section 9 we estimate an effective cross section defined by $\sigma_{effective} \simeq \sigma_{inelastic} + \frac{1}{2}\sigma_{elastic}$. Then the fraction of events lost due to K^oP interactions is:

$$\frac{N_{events}}{N_{incident}(\pi)} \simeq \rho L N_o \sigma_{effective}(K^oP) = .021$$

and the fraction of events lost due to K^-P interactions is:

$$\frac{N_{events}}{N_{incident}(\pi^-)} \simeq \rho L N_o \sigma_{effective}(K^-P) = .029.$$

So the probability that either the K^o or the K^- interacts would be

---

† We have assumed that $\sigma_{elastic}(K^+N) \simeq \sigma_{elastic}(K^+P)$.

$\simeq .021 + .029$.[†] Therefore the fraction of events lost because of interactions in the target is approximately $.05 \pm .01$, where the error is dominated by the uncertainty of the length of liquid hydrogen traversed by the K^o and K^-.

11. $K^o \rightarrow K^o_s$ Branching Ratio

The A_2^- decays strongly into a K^oK^- pair. At the time of production the K^o can be written as a linear combination of a shorter-lived component and a longer-lived component:

$$|K^o\rangle \simeq \frac{1}{\sqrt{2}} |K^o_s\rangle + \frac{1}{\sqrt{2}} |K^o_L\rangle \quad *$$

with 50% K_{short} and 50% K_{long}. Since our trigger required three forward-going charged particles slightly downstream of the target (at Z = 44.5"), we did not observe the longer-lived component ($c\tau$ for K^o_s = 2.65 cm and $c\tau$ for K^o_L = 1553 cm). We therefore correct the cross sections by a factor of two.

12. Unseen K^o_s Branching Ratio

The cross sections we quote are corrected for the unseen decay modes of the K^o_s. The correction factor we use is the inverse of the following:

$$\frac{K^o_s \rightarrow \pi^+\pi^-}{K^o_s \text{ (all modes)}} = .6885 \quad (14)$$

---

† We neglect the probability of both the K^o and the K^- interacting since this effect is essentially negligible.

* The equation would be an exact equality except for a small CP violating term. However, that term has a negligible effect on this calculation.

13. Pion Decay in Spectrometer

Some of the π's from the decay of the K_s^o will themselves decay into a $\mu^{\pm} + \nu_\mu$ pair (mean life time = 2.602×10^{-8} sec.) If the π's do decay far enough upstream in the spectrometer, the direction of the decaying muon would be such that the pattern recognition program (BEADS) would not be able to reconstruct the event. We can calculate the fraction of events lost due to pions decaying upstream of the last gap in the I-chamber* (Z = 238.0").

From our data the mean momentum of the π's from the decay of the K_s^o is $\approx$ 7 GeV/c. We associate a γ of 50 (i.e. $E = M_o\gamma$) and a mean decay distance of approximately 1280 feet (i.e. $c\tau\gamma$) for a 7-GeV/c pion. Then the fraction of pions which have not decayed at Z = 238.0" = 19.8' is given by:

$$N = N_o e^{-\frac{19.8}{1280}} = N_o(.985)$$

or 1.5% of the π's will have decayed before the end of the I-chamber. Since we have two pions we would lose approximately $3.0 \pm .5\%$ of the events. The error on this correction is due to the uncertainty in the Z decay point criterion on the pions.

14. Correction to the Total Cross-Section for Events with $|t'| > 1.0$

The differential cross-section in both sets of data at large $|t'|$ is well fitted by a decreasing exponential of the form $\frac{d\sigma}{dt'} = e^{bt'}$ where

---

* See Chapter VI, Sec. G.

$b = 4.55 \pm .15$ $(GeV/c)^{-2}$ and $|t'| > .13$ $(GeV/c)^2$.† Due to the behavior of $\frac{d\sigma}{dt'}$ we expect almost all of the events to fall between $t' = t_{min}$ and $|t'| = 1.0$. We must, however, extrapolate the exponential past $|t'| = 1.0$ and correct for the fraction of the events we lose. The fraction of events lost if one assumes the same exponential behavior to continue past $|t'| > 1.0$ would be the ratio of the two integrals:

$$\text{fraction lost} = \frac{\int_{-1.0}^{-\infty} e^{bt'}\, dt'}{\int_{-.13}^{-1.0} e^{bt'}\, dt' + \sum_{t'=0}^{-.13} \frac{d\sigma}{dt'}\, \Delta t'} \quad \text{where } b = 4.55 \pm .15 \ (GeV/c)^{-2}$$

Doing the integration we get:

$$= 1.84 \pm 1.0\%$$

where the error associated with the correction is due to the statistical uncertainty in the slope parameter b.

H. Overall Systematic Error on the Cross Section

Table 6ℓ is a list of the systematic errors associated with the factors that determine the cross-sections. There are three dominant errors: (1) the acceptance (10%), (2) the program efficiency (8%), and (c) the trigger efficiency (5%). Since these errors are in principle uncorrelated, we fold in the above errors plus the other errors in

† See Sec. I.

Table 6&

A list of the systematic errors associated with the factors that determine the differential and total cross sections.

Correction factor	Systematic error*
Acceptance	10%
Program efficiency	8%
Trigger efficiency	5%
Proton cut	1%
Contamination of proton peak	2%
Empty target	1%
Beam contamination	.5%
Nuclear attenuation in target	1%
$K^{o}K^{-}$ interactions in target	1%
Pion decay in spectrometer	1%
Events lost for $-t' > 1.0$	1%
Length of target	.3%

* The systematic errors for the 22.4 and 23.9 GeV/c data are essentially the same.

Table 6ℓ in quadrature. The resultant error is 14%.

We note that there is a sizeable (1/8) chance that the three dominant errors mentioned above may all point in one direction, in which case the quadrature method of obtaining a rms error may not be appropriate. In fact it may be appropriate to consider alternatively the calculation of the systematic error range which, of course, would then not be subject to ordinary statistical fluctuations but would be in the nature of a limit error. This overall limit error was obtained by adding all the errors linearly; the result leads to an overall limit error of 32%. However, one should note that it is very unlikely ($1/2^9$) that all the smaller ($\sim$ 1%) errors would add linearly and a ($1/2^{11}$) chance that all the errors would add linearly. Therefore we believe a more realistic estimate of the effect of these smaller errors on the limit error is to compound them in quadrature, which gives a systematic error of 3.2%, and add this number linearly to the linear sum of the three dominant errors. Doing this, we obtain a reasonable estimate of the limit error to be 26%.

In summary, the estimate of the systematic limit error is 32% and the rms value of the systematic error is 14%. The number we used for the systematic error on the cross section was the rms value of 14%.

I. Differential Cross-Section Data

After applying the corrections previously described, we present the differential cross-section data in both tabular and graphical form for the reaction:

$$\pi^- P \rightarrow A_2^- P$$
$$\downarrow$$
$$K^o K^-$$

at 22.4 and 23.9 GeV/c incident momenta using two effective mass cuts: (1) $1.2 < M(K_s^o K^-) < 1.4$ GeV and (2) $1.1 < M(K_s^o K^-) < 1.5$ GeV.

Tables 6m, 6n, 6o, and 6p indicate the fitted events, acceptance and differential cross-section as a function of -t' for the above reaction at each momentum (22.4 and 23.9 GeV/c) for both effective mass cuts (1) $1.2 < M(K_s^o K^-) < 1.4$ GeV, and (2) $1.1 < M(K_s^o K^-) < 1.5$ GeV. The errors indicated are statistical only. There is an additional 14% rms systematic error. The smooth curves in Figs. 28-31 are the results of a least-squares fit to the differential cross-section of the form $-t'e^{bt'}$ where $0.0 < |t'| < 1.0$. The dashed lines in Figs. 28-31 are the result of a least-squares fit to the differential cross-section of the form $e^{bt'}$ for $|t'| > .13$ $(GeV/c)^2$.

The cross-sections show a forward dip near $|t'| \approx .02$ $(GeV/c)^2$ and an exponential fall approximately as $e^{4.5t'}$ for $|t'|$ larger than .13 $(GeV/c)^2$. A least-squares fit to the differential cross-section data of the form $-t'e^{bt'}$ in the $|t'|$ interval $0.0 < |t'| < 1.0$ $(GeV/c)^2$ gave a value for the parameter $b = 7.0 \pm .2$ $(GeV/c)^{-2}$. We also fitted the differential cross-section data for $0.0 < |t'| < 1.0$ $(GeV/c)^2$ with a form $(-t')^a e^{bt'}$. The results of the fit gave a value for the parameter "a" consistent with 1 (i.e. $a = .94 \pm .14$ and $1.2 \pm .11$ $(GeV/c)^{-2}$ for the 22.4 and 23.9 GeV/c runs respectively).

Table 6q indicates the results of a least-squares fit to the differential cross-section data for the two momenta (22.4 and 23.9 GeV/c) in the mass ranges 1.2-1.4 GeV and 1.1-1.5 GeV for the two functional

Table 6m

Fitted events, acceptance, and differential cross section as a function of $-t'$ for the reaction $\pi^- p \to A_2^- P$ at 22.4 GeV/c and $1.2 < M(K_s^o K^-) < 1.4$ GeV. ($A_2^- \downarrow K^o K^-$)

$-t'$ $(GeV/c)^2$	Fitted Events	Acceptance	$\frac{d\sigma}{dt'}\left[\frac{\mu b}{(GeV/c)^2}\right]$
.0 -.02	7.8	.054 ± .001	1.55 ± .74
.02-.04	19.0	.054 ± .001	3.77 ± 1.01
.04-.06	18.7	.054 ± .001	3.72 ± 1.13
.06-.08	25.4	.054 ± .001	5.04 ± 1.13
.08-.10	30.9	.054 ± .001	6.14 ± 1.23
.10-.12	36.4	.054 ± .001	7.23 ± 1.25
.12-.14	42.6	.054 ± .001	8.47 ± 1.45
.14-.16	40.1	.054 ± .001	7.97 ± 1.29
.16-.18	35.9	.054 ± .001	7.14 ± 1.23
.18-.20	28.8	.053 ± .001	5.83 ± 1.19
.20-.22	27.6	.053 ± .001	5.59 ± 1.15
.22-.24	24.2	.053 ± .001	4.90 ± 1.05
.24-.26	35.9	.053 ± .001	7.27 ± 1.28
.25-.28	14.8	.052 ± .001	3.06 ± 1.05
.28-.30	33.0	.052 ± .001	6.81 ± 1.17
.30-.35	60.9	.052 ± .001	5.02 ± .64
.35-.40	27.4	.051 ± .001	2.31 ± .51
.40-.45	29.6	.050 ± .002	2.54 ± .46
.45-.50	26.0	.049 ± .002	2.28 ± .45
.50-.60	25.6	.048 ± .002	1.14 ± .26
.60-.70	17.8	.046 ± .002	.83 ± .20
.70-1.0	19.3	.042 ± .003	.33 ± .08

Errors shown are statistical only. There is also a 14% rms overall systematic error.

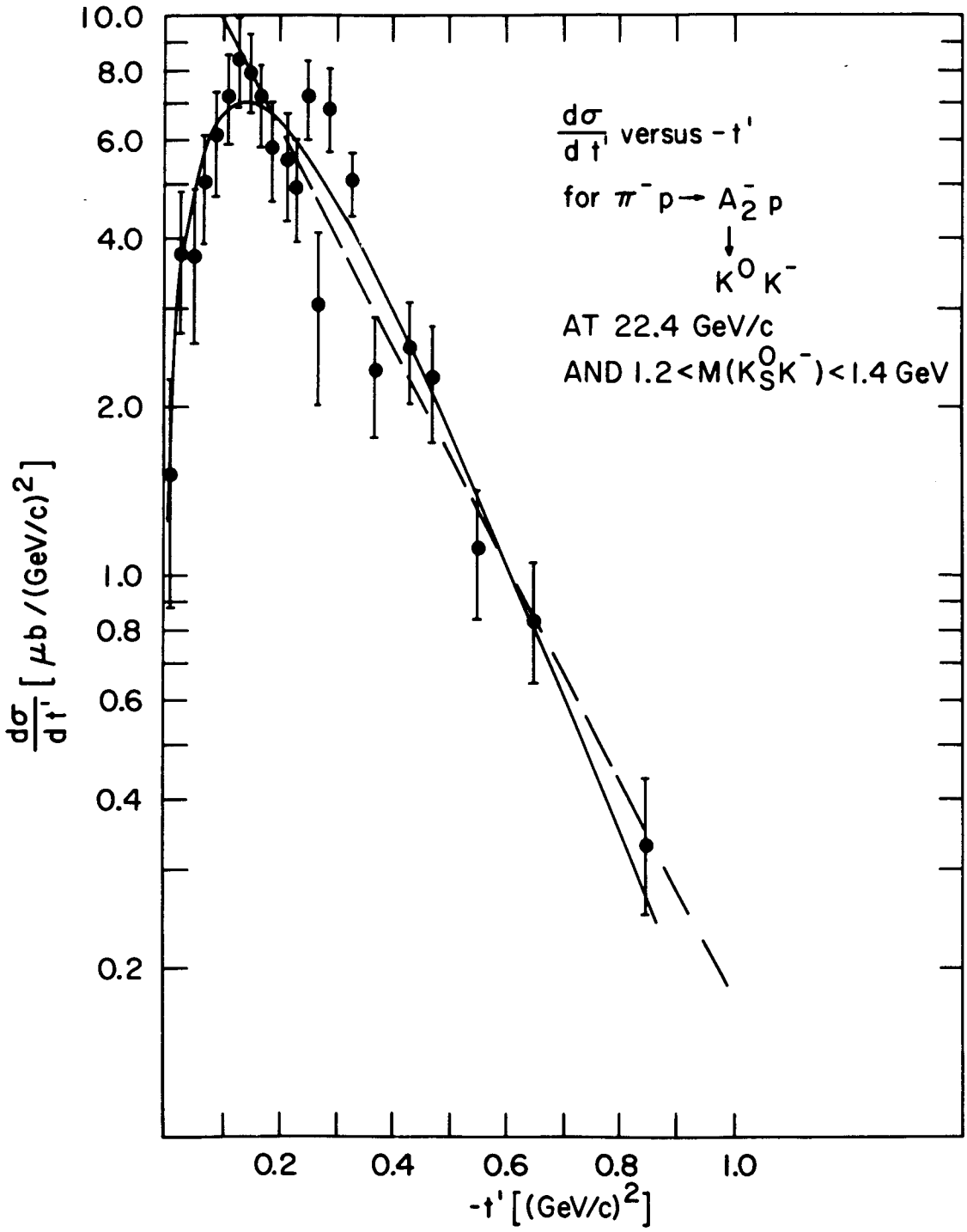
10.0
8.0
6.0
4.0
2.0
1.0
0.8
0.6
0.4
0.2
0.2
0.4
0.6
0.8
1.0
$\frac{d\sigma}{dt'}$ versus $-t'$
for $\pi^- p \rightarrow A_2^- p$
$\downarrow$
$K^0 K^-$
AT 22.4 GeV/c
AND $1.2 < M(K_S^0 K^-) < 1.4$ GeV
$\frac{d\sigma}{dt'}$ [μb / (GeV/c)^2]
$-t'$ [(GeV/c)^2]

Figure 28

Table 6n

Fitted events, acceptance, and differential cross section as a function of $-t'$ for the reaction $\pi^- P \to A_2^- P$ at 22.4 GeV/c and $1.1 < M(K_s^0 K^-) < 1.5$ GeV. ($A_2^- \to K^0 K^-$)

$-t'$ $(GeV/c)^2$	Fitted Events	Acceptance	$\frac{d\sigma}{dt'}\left[\frac{\mu b}{(GeV/c)^2}\right]$
.0 -.02	9.2	.054 ± .001	1.83 ± .92
.02-.04	22.5	.054 ± .001	4.47 ± 1.19
.04-.06	22.2	.054 ± .001	4.41 ± 1.37
.06-.08	29.9	.054 ± .001	5.94 ± 1.31
.08-.10	36.6	.054 ± .001	7.28 ± 1.43
.10-.12	43.0	.054 ± .001	8.55 ± 1.41
.12-.14	50.2	.054 ± .001	9.98 ± 1.65
.14-.16	47.5	.054 ± .001	9.44 ± 1.45
.16-.18	42.4	.054 ± .001	8.43 ± 1.37
.18-.20	33.8	.053 ± .001	6.85 ± 1.38
.20-.22	32.5	.053 ± .001	6.58 ± 1.32
.22-.24	28.6	.053 ± .001	5.79 ± 1.15
.24-.26	42.3	.053 ± .001	8.57 ± 1.42
.26-.28	17.5	.052 ± .001	3.61 ± 1.28
.28-.30	39.0	.052 ± .001	8.05 ± 1.28
.30-.35	72.0	.052 ± .001	5.94 ± .70
.35-.40	32.4	.051 ± .001	2.73 ± .59
.40-.45	35.2	.050 ± .001	3.02 ± .52
.45-.50	30.7	.049 ± .002	2.69 ± .49
.50-.60	30.1	.048 ± .002	1.35 ± .29
.60-.70	21.0	.046 ± .002	.98 ± .21
.70-1.0	22.8	.042 ± .003	.38 ± .08

Errors shown are statistical only. There is also a 14% rms overall systematic error.

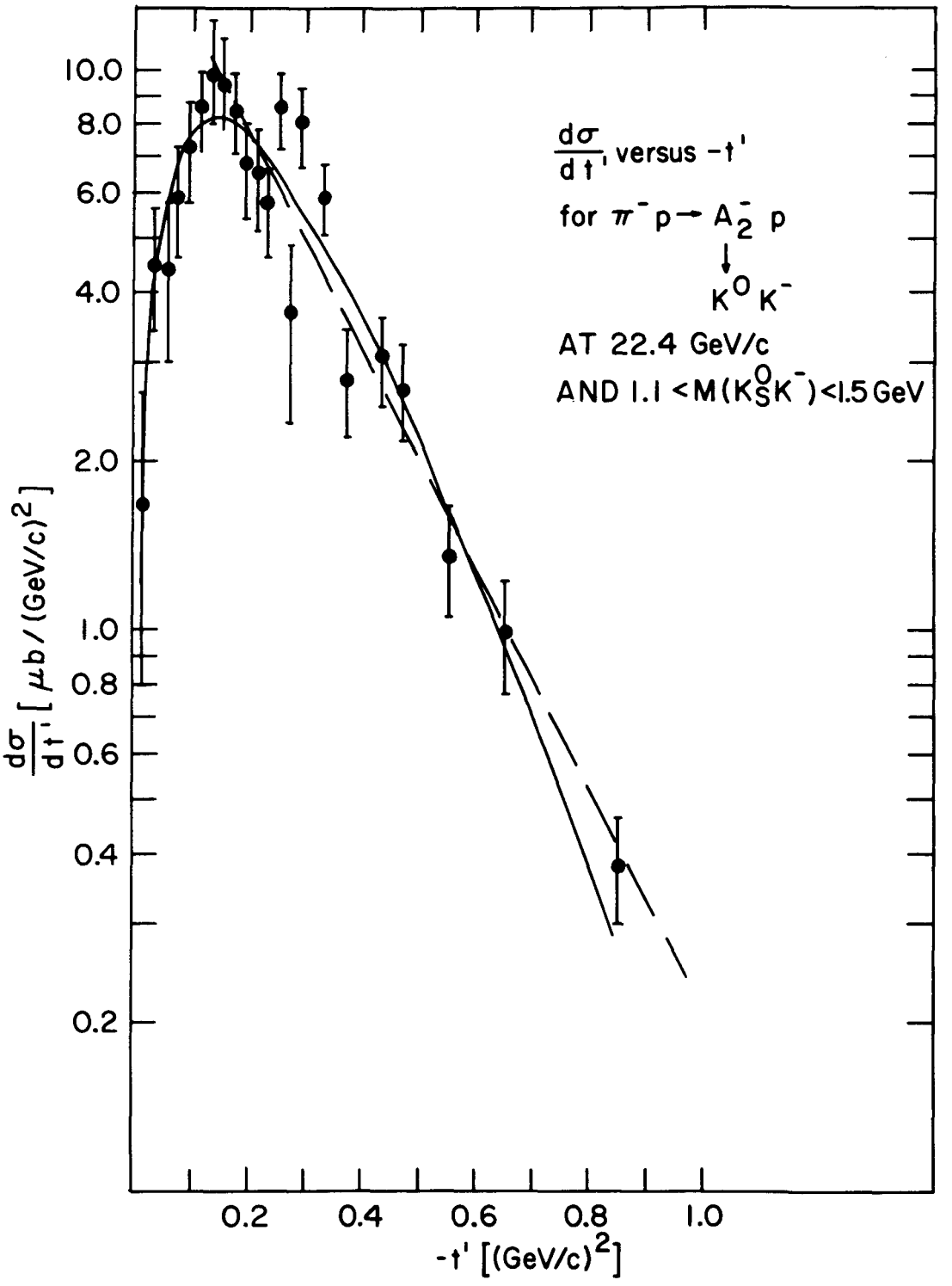
10.0
8.0
6.0
4.0
2.0
1.0
0.8
0.6
0.4
0.2
dσ/dt' [μb/(GeV/c)²]
0.2
0.4
0.6
0.8
1.0
-t' [(GeV/c)²]
dσ/dt' versus -t'
for π⁻p → A₂⁻ p
↓
K⁰ K⁻
AT 22.4 GeV/c
AND 1.1 < M(K⁰S K⁻) < 1.5 GeV

Figure 29

Table 6o

Fitted events, acceptance, and differential cross section as a function of -t' for the reaction $\pi^- P \to A_2^- P$ at 23.9 GeV/c and $1.2 < M(K_s^o K^-) < 1.4$ GeV. ($A_2^- \to K^o K^-$)

$-t'$ $(GeV/c)^2$	Fitted Events	Acceptance	$\frac{d\sigma}{dt'}\left[\frac{\mu b}{(GeV/c)^2}\right]$
.0 -.02	19.2	.055 ± .001	1.64 ± .48
.02-.04	28.6	.055 ± .001	2.44 ± .58
.04-.06	41.3	.055 ± .001	3.51 ± .62
.06-.08	36.3	.055 ± .001	3.09 ± .62
.08-.10	72.8	.055 ± .001	6.20 ± .75
.10-.12	66.4	.055 ± .001	5.65 ± .75
.12-.14	80.2	.055 ± .001	6.83 ± .83
.14-.16	70.3	.055 ± .001	5.98 ± .76
.16-.18	88.9	.055 ± .001	7.57 ± .83
.18-.20	87.2	.055 ± .001	7.43 ± .80
.20-.22	79.3	.055 ± .001	6.76 ± .80
.22-.24	79.9	.054 ± .001	6.93 ± .78
.24-.26	59.0	.054 ± .001	5.12 ± .69
.26-.28	60.2	.054 ± .001	5.22 ± .71
.28-.30	48.8	.054 ± .001	4.23 ± .66
.30-.35	116.6	.054 ± .001	4.05 ± .39
.35-.40	103.2	.053 ± .001	3.65 ± .39
.40-.45	60.9	.053 ± .002	2.15 ± .28
.45-.50	61.2	.053 ± .002	2.16 ± .28
.50-.60	77.3	.053 ± .002	1.37 ± .16
.60-.70	46.0	.051 ± .002	.85 ± .13
.70-1.0	33.9	.047 ± .003	.23 ± .04

Errors shown are statistical only. There is also a 14% rms overall systematic error.

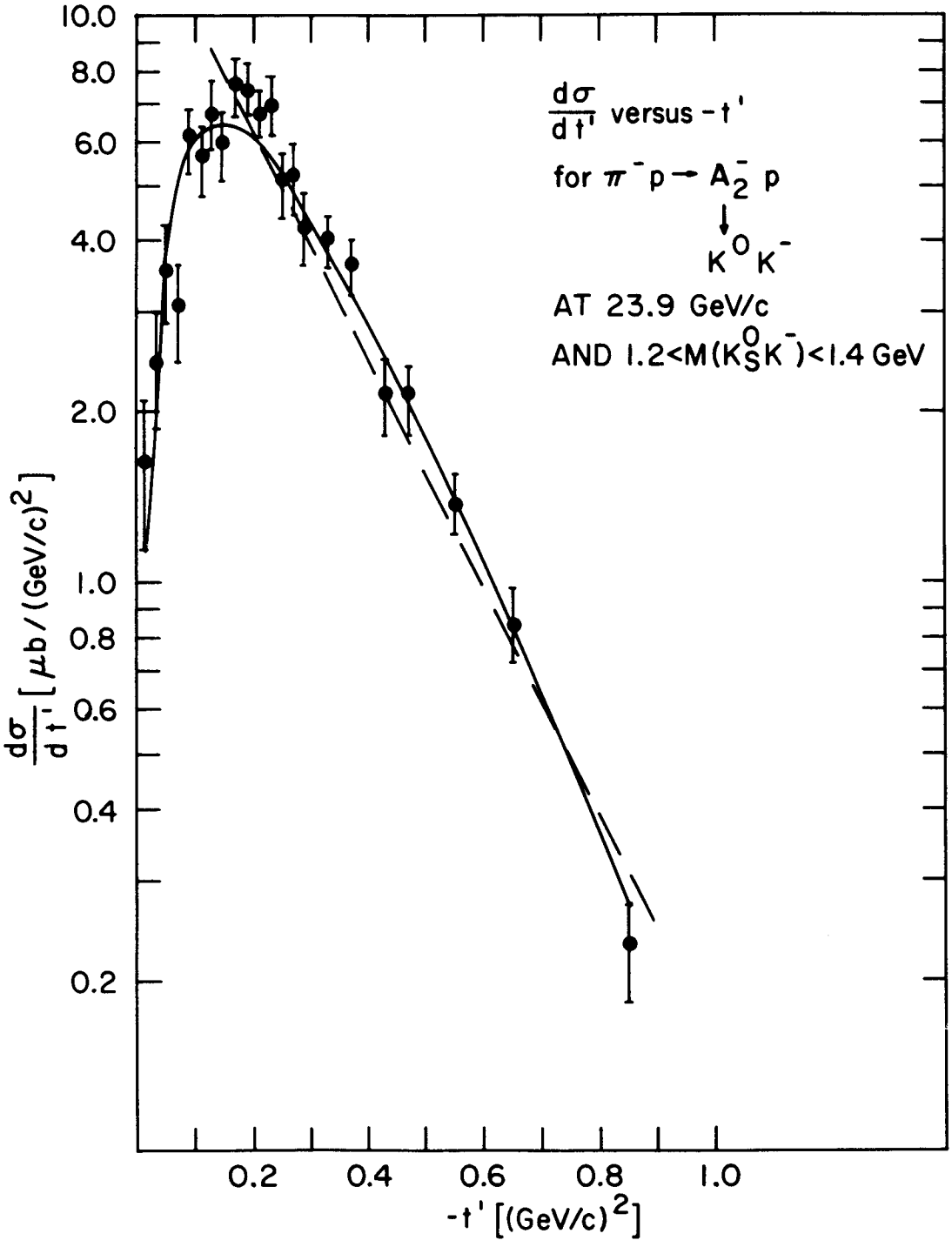
10.0
8.0
6.0
4.0
2.0
1.0
0.8
0.6
0.4
0.2
$\frac{d\sigma}{dt'}$ versus $-t'$
for $\pi^- p \rightarrow A_2^- p$
$\downarrow$
$K^0 K^-$
AT 23.9 GeV/c
AND $1.2 < M(K_S^0 K^-) < 1.4$ GeV
$\frac{d\sigma}{dt'}[\mu b/(GeV/c)^2]$
0.2
0.4
0.6
0.8
1.0
$-t'[(GeV/c)^2]$

Figure 30

Table 6p

Fitted events, acceptance, and differential cross section as a function of $-t'$ for the reaction $\pi^- P \to A_2^- P$ at 23.9 GeV/c and $1.1 < M(K_S^0 K^-) < 1.5$ GeV. ($A_2^- \to K^0 K^-$)

$-t'$ $(GeV/c)^2$	Fitted Events	Acceptance	$\frac{d\sigma}{dt'}\left[\frac{\mu b}{(GeV/c)^2}\right]$
.0 -.02	22.7	.055 ± .001	1.93 ± .57
.02-.04	33.9	.055 ± .001	2.88 ± .69
.04-.06	47.8	.055 ± .001	4.07 ± .72
.06-.08	43.1	.055 ± .001	3.67 ± .75
.08-.10	86.7	.055 ± .001	7.39 ± .84
.10-.12	79.0	.055 ± .001	6.73 ± .85
.12-.14	95.5	.055 ± .001	8.14 ± .95
.14-.16	83.8	.055 ± .001	7.14 ± .85
.16-.18	105.9	.055 ± .001	9.02 ± .94
.18-.20	102.7	.055 ± .001	8.75 ± .88
.20-.22	94.5	.055 ± .001	8.05 ± .89
.22-.24	95.2	.054 ± .001	8.26 ± .86
.24-.26	70.0	.054 ± .001	6.07 ± .77
.26-.28	71.9	.054 ± .001	6.24 ± .81
.28-.30	58.3	.054 ± .001	5.06 ± .76
.30-.35	138.9	.054 ± .001	4.82 ± .43
.35-.40	122.9	.053 ± .001	4.34 ± .44
.40-.45	72.7	.053 ± .002	2.57 ± .31
.45-.50	73.0	.053 ± .002	2.58 ± .30
.50-.60	92.3	.053 ± .002	1.63 ± .18
.60-.70	54.7	.051 ± .002	1.01 ± .14
.70-1.0	40.3	.047 ± .003	.27 ± .05

Errors shown are statistical only. There is also a 14% rms overall systematic error.

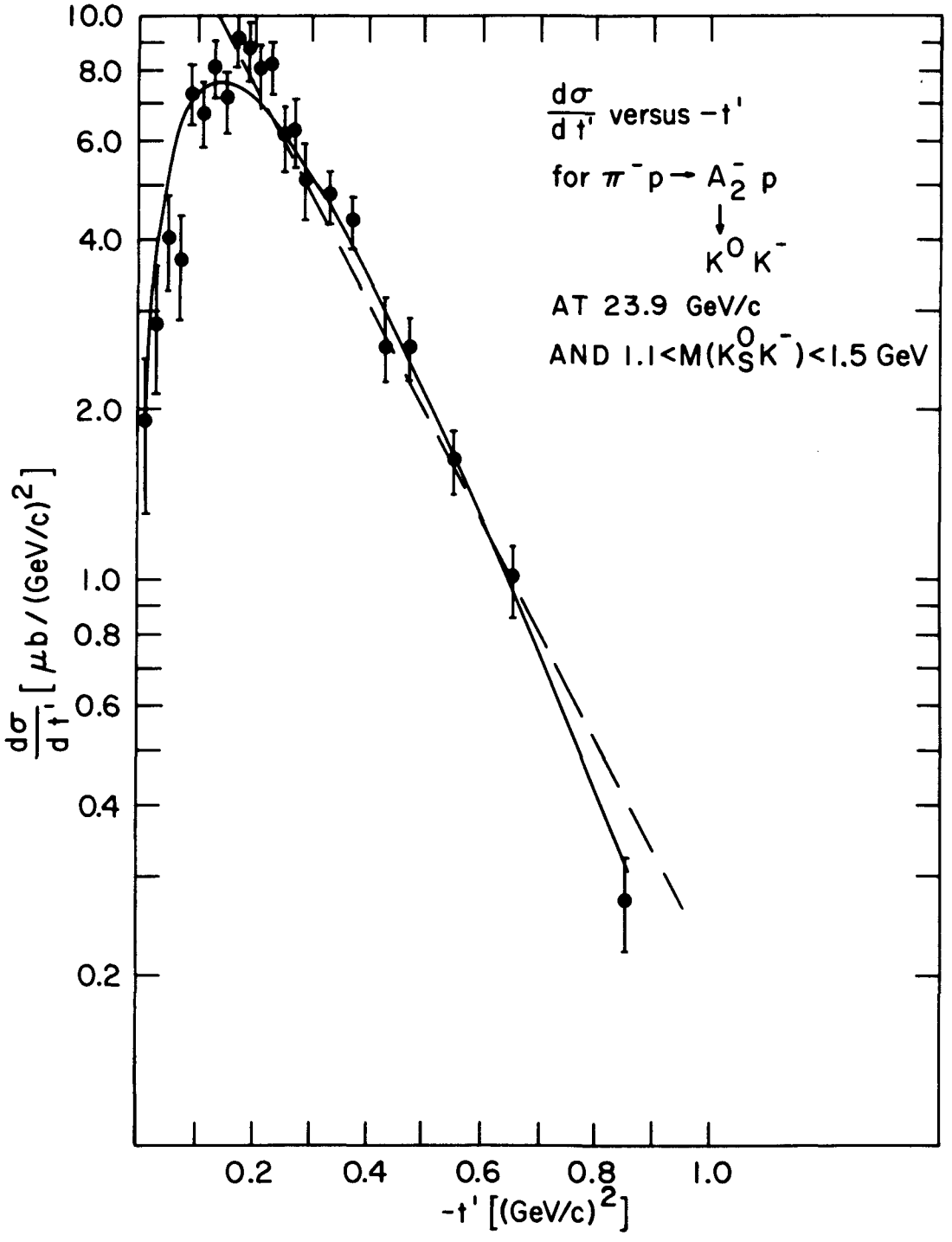
dσ/dt' versus -t'
for π⁻p → A₂⁻ p
↓
K⁰ K⁻
AT 23.9 GeV/c
AND 1.1<M(K⁰S K⁻)<1.5 GeV
dσ/dt' [μb/(GeV/c)²]
-t' [(GeV/c)²]
10.0
8.0
6.0
4.0
2.0
1.0
0.8
0.6
0.4
0.2
0.2
0.4
0.6
0.8
1.0

Figure 31

Table 6q

Functional form of $\frac{d\sigma}{dt'}$	P(GeV/c)	Mass cut (GeV)	t' region $(GeV/c)^2$	Fit Parameters
$-t'e^{bt'}$	22.4	$1.2<M(K^0_sK^-)<1.4$	$0.0<\|t'\|<1.0$	$b=7.25\pm.26$
$-t'e^{bt'}$	22.4	$1.1<M(K^0_sK^-)<1.5$	$0.0<\|t'\|<1.0$	$b=7.23\pm.24$
$-t'e^{bt'}$	23.9	$1.2<M(K^0_sK^-)<1.4$	$0.0<\|t'\|<1.0$	$b=7.01\pm.14$
$-t'e^{bt'}$	23.9	$1.1<M(K^0_sK^-)<1.5$	$0.0<\|t'\|<1.0$	$b=7.01\pm.14$
$e^{bt'}$	22.4	$1.2<M(K^0_sK^-)<1.4$	$.13<\|t'\|$	$b=4.47\pm.25$
$e^{bt'}$	22.4	$1.1<M(K^0_sK^-)<1.5$	$.13<\|t'\|$	$b=4.50\pm.21$
$e^{bt'}$	23.9	$1.2<M(K^0_sK^-)<1.4$	$.13<\|t'\|$	$b=4.59\pm.15$
$e^{bt'}$	23.9	$1.1<M(K^0_sK^-)<1.5$	$.13<\|t'\|$	$b=4.56\pm.14$

forms: (1) $-t'e^{bt'}$ and (2) $e^{bt'}$ in the $|t'|$ intervals $0.0 < |t'| < 1.0$ $(GeV/c)^2$ and $|t'| > .13$ $(GeV/c)^2$ respectively. The errors on the parameters shown in Table 6q are statistical only.

J. Results of the Total Cross-Section Measurements

After having applied all the corrections previously described, we present the total cross sections in Table 6r for the reaction

$$\pi^- P \to A_2^- P \downarrow K^o K^-$$

at 22.4 and 23.9 GeV/c incident momenta using the two effective mass cuts: (1) $1.2 < M(K_s^o K^-) < 1.4$ GeV, and (2) $1.1 < M(K_s^o K^-) < 1.5$ GeV.

Figure 32 is a plot of the available total cross-section data for this reaction above 3.9 GeV/c.[1,2] We note that the total cross sections plotted in Fig. 32 are corrected to include all t' regions and are restricted to the mass interval $1.2 < M(K_s^o K^-) < 1.4$ GeV. The rms systematic error compounded with the statistical error was used on our points. A least-squares fit to the momentum dependence of the form $\sigma_{tot} \alpha P^{-N}$[28] yields $N = 1.18 \pm .11$.

The total cross section for the reaction $\pi^- P \to A_2^- P \downarrow K^o K^-$ seems to have a momentum dependence which falls off faster than that reported by other investigators[3] for the $\rho^o \pi^-$ decay mode of the A_2^-. From the data published in the XVII International Conference on High Energy Physics (London), it appears that in the reaction

$$\pi^- P \to A_2^- P \downarrow \rho^o \pi^- \downarrow \pi^+ \pi^-$$

Table 6r

Total Cross-Section Results

P(GeV/c)	$1.2 < M(K_S^0 K^-) < 1.4$	$1.1 < M(K_S^0 K^-) < 1.5$
22.4	$\sigma_T = 2.64 \pm .10$ μb	$\sigma_T = 3.12 \pm .11$ μb
23.9	$\sigma_T = 2.51 \pm .07$ μb	$\sigma_T = 2.99 \pm .07$ μb

(The errors shown are statistical only. There is also a 14% overall systematic error.)

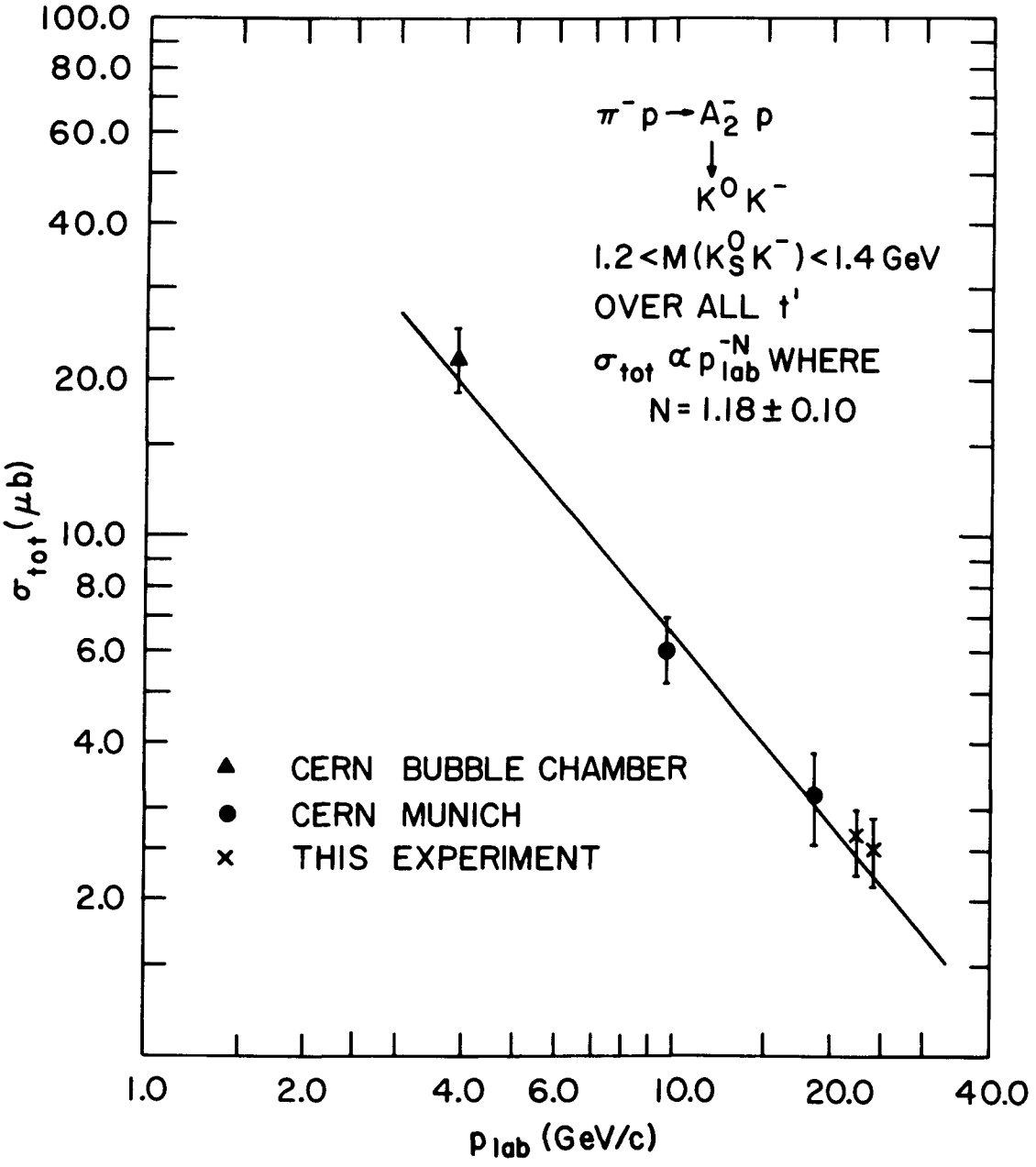
100.0
80.0
60.0
40.0
20.0
10.0
8.0
6.0
4.0
2.0
σ_{tot} (μb)
$\pi^- p \rightarrow A_2^- p$
$K^0 K^-$
$1.2 < M(K_S^0 K^-) < 1.4$ GeV
OVER ALL t'
$\sigma_{tot} \propto p_{lab}^{-N}$ WHERE
$N = 1.18 \pm 0.10$
CERN BUBBLE CHAMBER
CERN MUNICH
THIS EXPERIMENT
1.0
2.0
4.0
6.0
10.0
20.0
40.0
p_{lab} (GeV/c)

Figure 32

where $1.2 < M(3\pi) < 1.4$ GeV, the momentum dependence of the total cross section falls off approximately as $\sigma_{tot} \alpha P_{Lab}^{-N}$ where $N \approx .58 \pm .18$.

It should be noted that, in the data from which the $\rho^o\pi^-$ decay mode of the A_2^- was determined, the signal-to-background ratio is typically one to three,[29] whereas in the K^oK^- decay mode of the A_2^- the signal-to-background ratio in the mass range of the $K_s^oK^-$ = 1.2-1.4 GeV is typically four to one. This may possibly be a source of systematic error in the evaluation of the cross section, resulting in a difference in the momentum dependence of the cross sections for the two reactions.

K. Conclusions

The differential cross sections show a forward dip near $|t'| \approx .02$ $(GeV/c)^2$, which is expected for natural spin-parity vector meson exchange,[30] and an exponential fall approximately as $e^{4.5t'}$ for $|t'|$ larger than .13 $(GeV/c)^2$. A least-squares fit to the differential cross-section data of the form $-t'e^{bt'}$ in the $|t'|$ interval $0.0 < |t'| < 1.0$ $(GeV/c)^2$ gave a value for the parameter $b = 7.0 \pm .2$ $(GeV/c)^{-2}$.

The total cross sections for the reaction

$$\pi^-P \rightarrow A_2^-P$$
$$\downarrow$$
$$K^oK^-$$

at 22.4 and 23.9 GeV/c are $2.64 \pm .10$ μb and $2.51 \pm .07$ μb respectively. These cross sections were calculated for the mass interval of the $K_s^oK^-$ between 1.2 and 1.4 GeV and have been corrected for all t'.

The errors shown on the cross sections are statistical only; there is also a 14% rms systematic error on the cross sections.

The result of a least-squares fit to the momentum dependence of the cross sections (for the above reaction) to the form $\sigma_{Tot} \alpha P_{Lab}^{-N}$, using our data and the data from other experiments,[1,2] yields a value of $N = 1.18 \pm .11$. We note that the cross-section numbers from the other experiments were also calculated for the $K_s^o K^-$ mass region 1.2-1.4 GeV, and included the corrections for all t' regions.

The total cross section for the reaction $\pi^- p \to A_2^- P$, $A_2^- \to K^o K^-$ seems to have a momentum dependence which falls off faster than that reported by other investigators[3] for the $\rho^o \pi^-$ decay mode. It appears that in the reaction

$$\pi^- P \to A_2^- P, \quad A_2^- \to \rho^o \pi^-, \quad \rho^o \to \pi^+ \pi^-$$

where $1.2 < M(3\pi) < 1.4$ GeV, the momentum dependence of the total cross section falls off approximately as $\sigma_{Tot} \alpha P_{Lab}^{-N}$ where $N \approx .58 \pm .18$.

CHAPTER VII

ANGULAR DECAY DISTRIBUTIONS

A. Decay Angular Distributions in the Gottfried-Jackson Frame

Figures 33, 34 show the projected angular distributions in the Gottfried-Jackson frame[17] as a function of $\cos\theta$ and ϕ. The data are uncorrected for the acceptance of the apparatus. The angle θ is the angle between the incoming π^- and the outgoing K^- in the A_2 rest frame, and ϕ is the angle between the plane of production and the decay plane in the A_2 rest frame. The smaller peak for positive values of $\cos\theta$ results from a lower acceptance for low-momentum K^o's in our apparatus. Figures 35, 36 are the above projected angular distributions in the Gottfried-Jackson frame corrected for the acceptance of the apparatus. The smooth curves in Figs. 35,36 are the results of a maximum likelihood fit to the data assuming a functional form described below.

B. Nature of the Exchanged Particle

We performed a maximum likelihood fit to the data assuming (a) that we were observing the decay of a $J^P = 2^+$ meson into two pseudoscalar mesons, and (b) that the 2^+ meson was originally produced by the exchange of natural spin-parity vector mesons.

The angular decay distribution for a spin 2^+ meson decaying into two pseudoscalar mesons (i.e. $J^P = 0^-$), where we restrict ourselves to pseudoscalar and vector meson exchange, is[31]

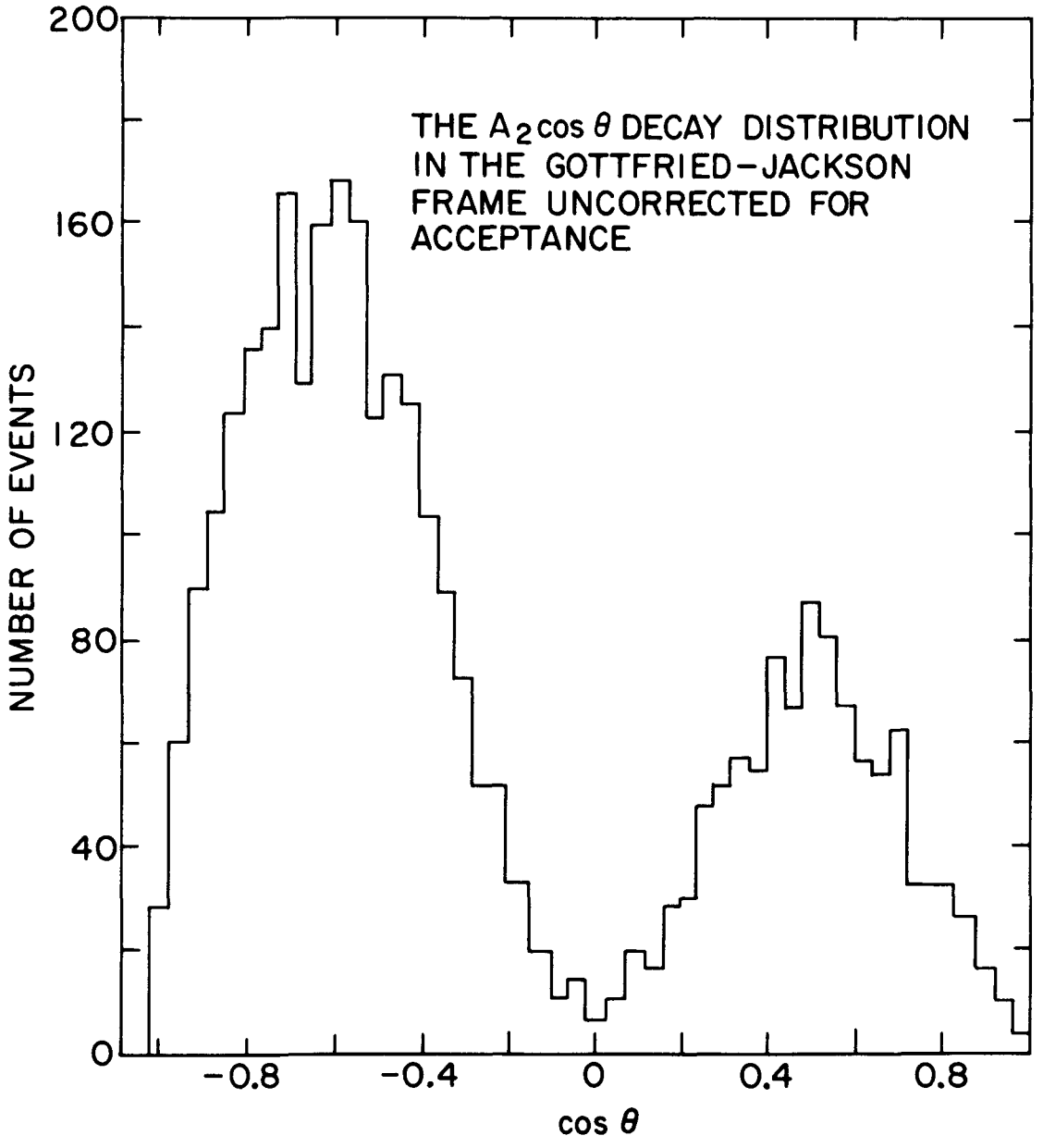
THE $A_2 \cos\theta$ DECAY DISTRIBUTION IN THE GOTTFRIED-JACKSON FRAME UNCORRECTED FOR ACCEPTANCE
NUMBER OF EVENTS
200
160
120
80
40
0
-0.8
-0.4
0
0.4
0.8
cos θ

Figure 33

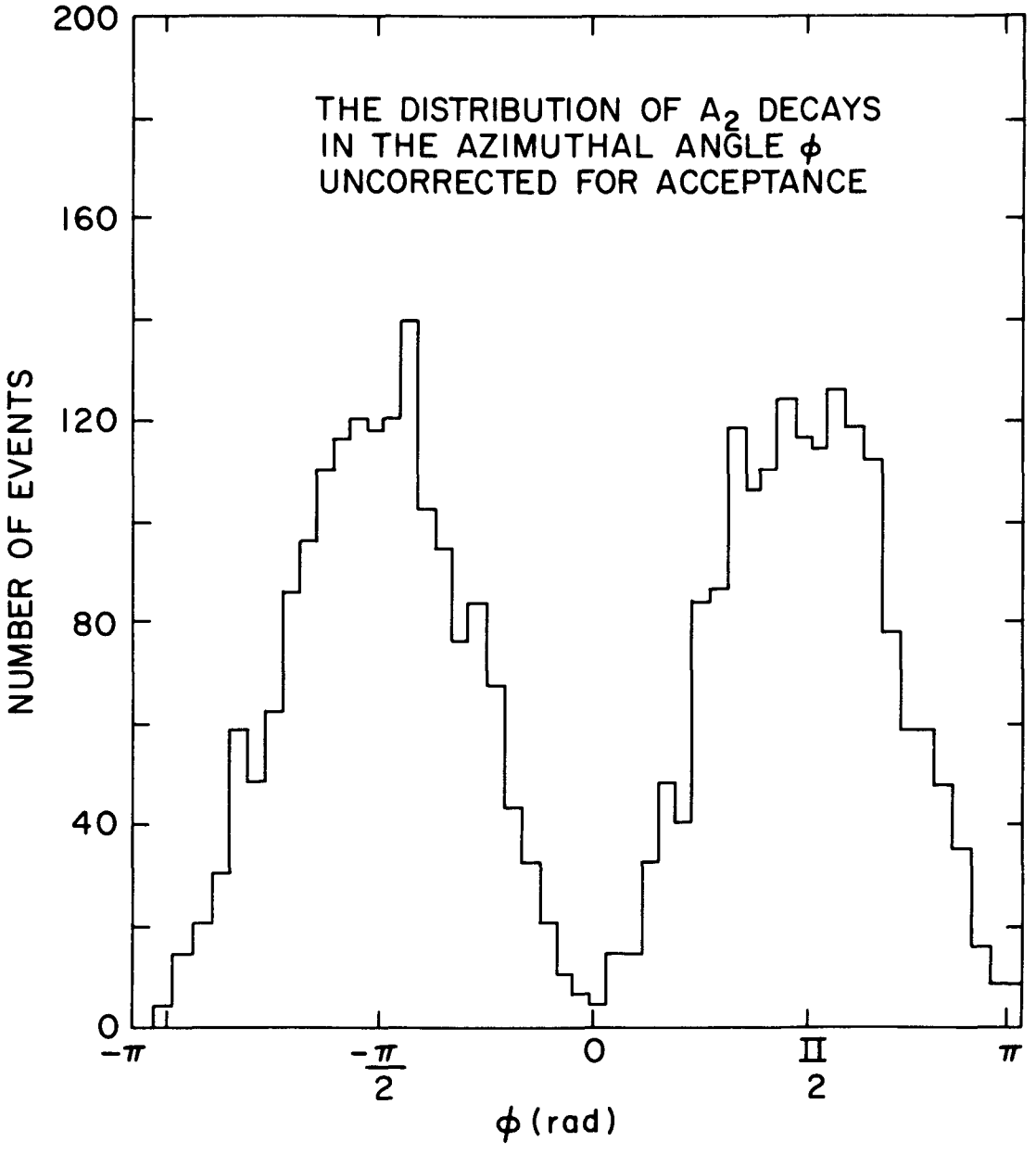
THE DISTRIBUTION OF A_2 DECAYS
IN THE AZIMUTHAL ANGLE ϕ
UNCORRECTED FOR ACCEPTANCE
NUMBER OF EVENTS
200
160
120
80
40
0
$-\pi$
$-\frac{\pi}{2}$
0
$\frac{\pi}{2}$
π
ϕ (rad)

Figure 34

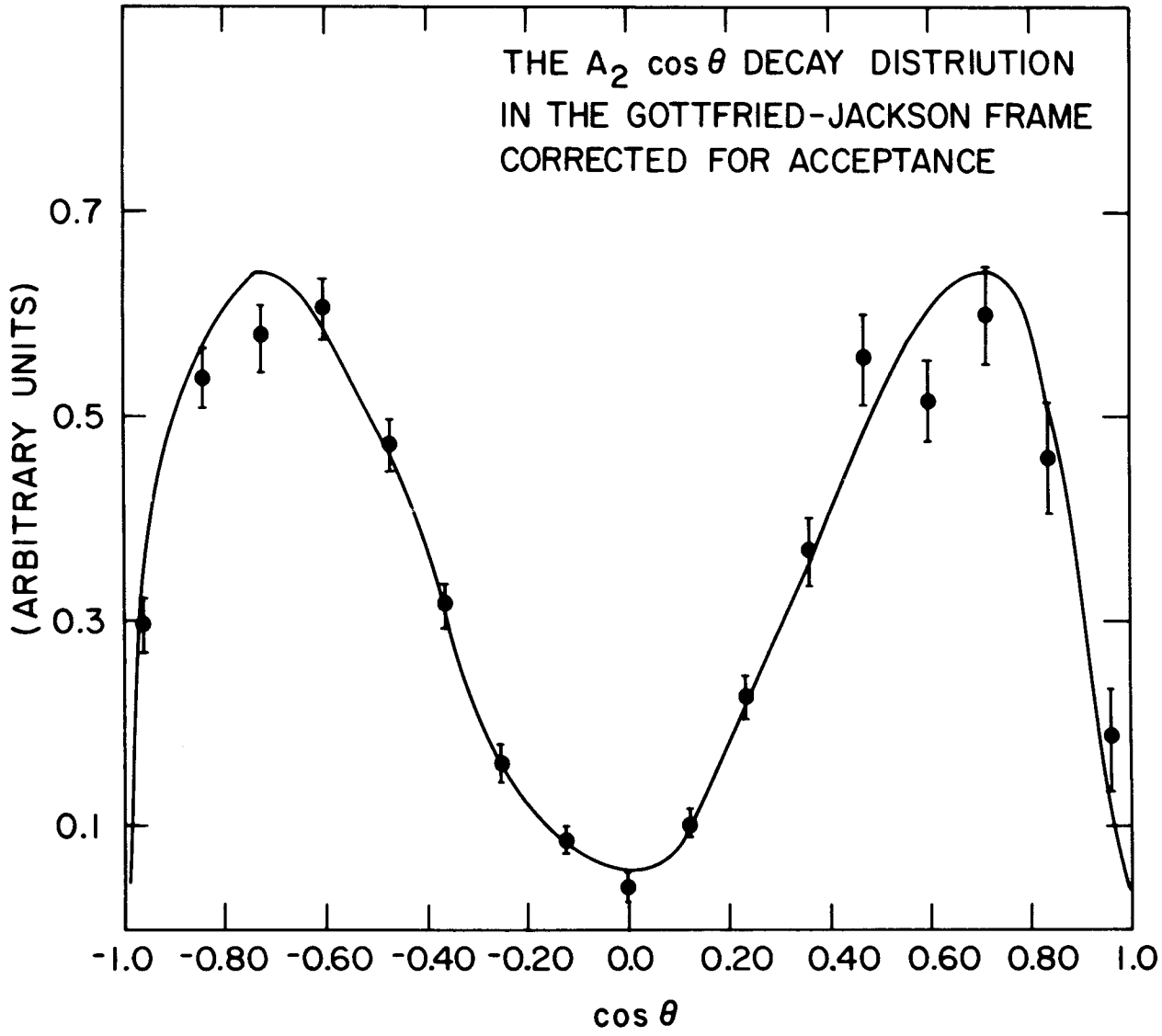
THE $A_2 \cos\theta$ DECAY DISTRIUTION
IN THE GOTTFRIED-JACKSON FRAME
CORRECTED FOR ACCEPTANCE
(ARBITRARY UNITS)
0.7
0.5
0.3
0.1
-1.0
-0.80
-0.60
-0.40
-0.20
0.0
0.20
0.40
0.60
0.80
1.0
$\cos\theta$

Figure 35

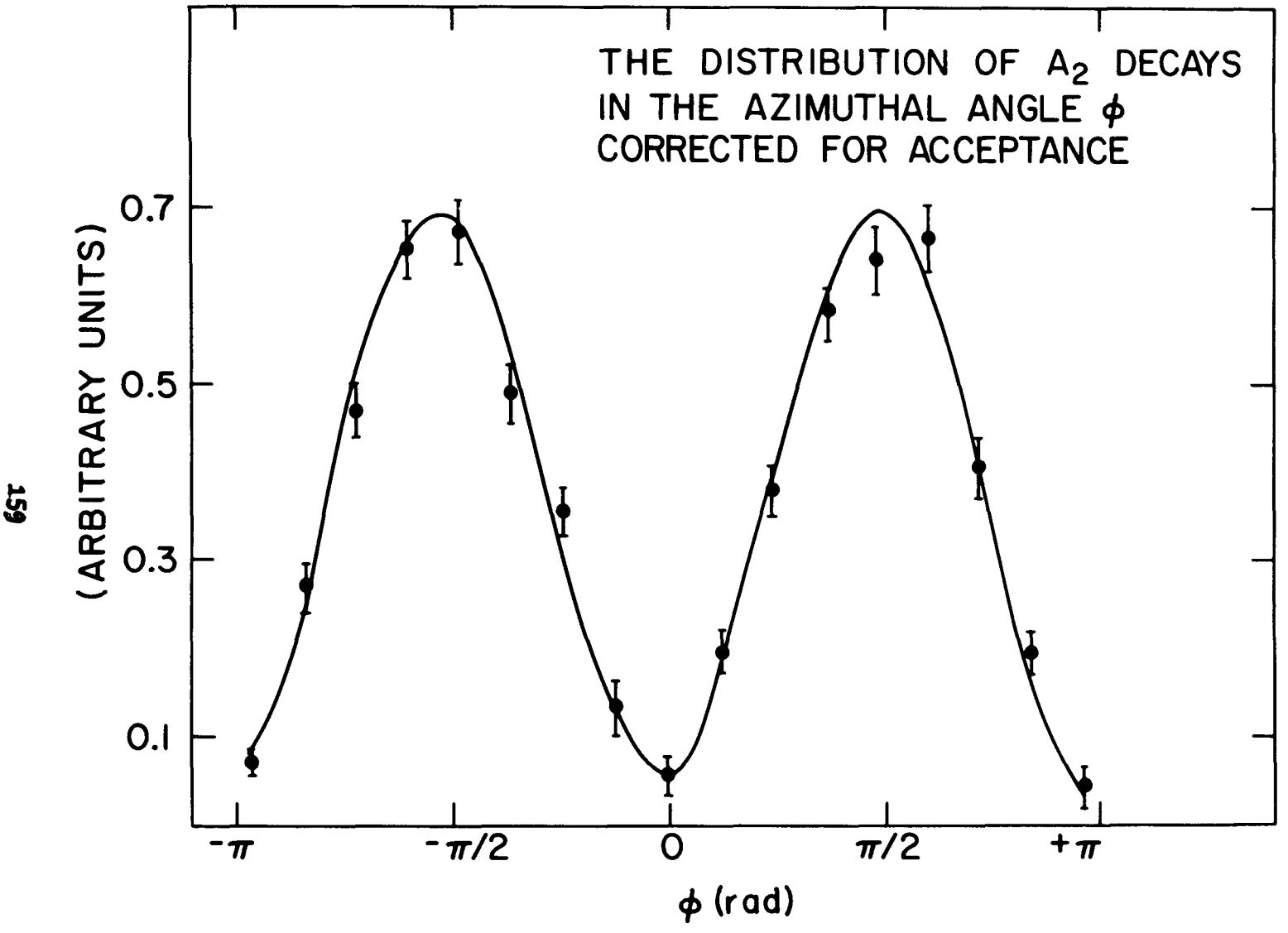
THE DISTRIBUTION OF A_2 DECAYS
IN THE AZIMUTHAL ANGLE ϕ
CORRECTED FOR ACCEPTANCE
(ARBITRARY UNITS)
0.7
0.5
0.3
0.1
$-\pi$
$-\pi/2$
0
$\pi/2$
$+\pi$
ϕ (rad)

Figure 36

$$(1)\quad W(\cos\theta,\phi) \propto \{3\rho_{oo}(\cos^2\theta - \tfrac{1}{3})^2 + 4\sin^2\theta\cos^2\theta\,(\rho_{11} - \rho_{1-1}\cos 2\phi)$$

A density matrix analysis for the decay of the A_2^- into a K^oK^- pair from other experiments[10,32] performed at energies close to ours are consistent with

$$\rho_{oo} \simeq 0 \text{ and } \rho_{11} \simeq \rho_{1-1} \simeq \frac{1}{2}\,.$$

The projected angular distributions in $\cos\theta$ and ϕ were fit assuming a functional form for the angular distribution:

$$W(\cos\theta,\phi) \propto \cos^2\theta\,\sin^2\theta\,\sin^2\phi$$

and an isotropic background. The result of a maximum likelihood fit using the above form yielded $\chi^2(\cos\theta) = 62$ for 48 degrees of freedom and $\chi^2(\phi) = 57$ for 48 degrees of freedom. The number of events in the background was $\simeq$ 10-15% of the total events, which is in good agreement with the background as determined by fits to the effective mass spectrum.

The good fit to our angular distribution data with the above assumptions clearly implies that our assumptions were reasonable. Furthermore, our observed decay angular distribution may be explained by and strongly implies that the dominant particles exchanged in our production process are natural spin parity vector particles (i.e. $\rho_o(770)$, $f_o(1270)$).

CHAPTER VIII

CONCLUSIONS

A. The Shape of the A_2 Mass Spectra

For the reaction $\pi^- P \to K_s^o K^- + P$ using $\simeq$ 23 GeV/c pions, we have obtained and analyzed 3346 new events in the effective mass range $1.1 < M(K_s^o K^-) < 1.5$ GeV. The data are well fit ($\chi^2 = 69$ for 76 degrees of freedom) by a single D-wave Breit-Wigner (and $\sim$ 10-20% background). No two-peak structure was observed. The previously reported CERN dipole type fit was rejected by 7.9 standard deviations.

Analysis of the mass spectra for different t' ranges $0 < -t' < .2$, $.2 < -t' < .29$, and $-t' > .29$ reveals that a single D-wave Breit-Wigner is an excellent fit (χ^2 per degree of freedom $\simeq 1$) to the data.

The dipole fits to the data in the $-t'$ ranges $0. < -t' < .20$ and $-t' > .29$ in the mass interval 1.2-1.4 GeV were improbable by 3.0 and 3.8 standard deviations respectively. The region $0.2 < -t' < 0.29$ has generated considerable interest. In the mass interval 1.2-1.4 GeV, the dipole fit was still improbable by 3 standard deviations, whereas the single D-wave Breit-Wigner gave an excellent fit.

In order to concentrate on the region where the functional form of the dipole has a dip and to eliminate contributions to the χ^2 from the tails of the mass spectrum, we fitted the total data in the mass region $1.25 < M(K_s^o K^-) < 1.35$ GeV. The best fit had a χ^2 of 71 for 18 degrees of freedom or a six-standard-deviation rejection.

B. Differential and Total Cross Sections

The differential cross-section data exhibit a forward dip near four-momentum transfer $|t| \simeq .02$ $(GeV/c)^2$ and an exponential fall approximately as $e^{4.5t'}$ for $|t'|$ larger than .13 $(GeV/c)^2$. The differential cross-section data are well fitted to the form $-t'e^{bt'}$ in the $|t'|$ interval $0.0 < |t'| < 1.0$ $(GeV/c)^2$ with a value for the parameter $b = 7.0 \pm .2$ $(GeV/c)^{-2}$.

The total cross sections for the reaction

$$\pi^- P \rightarrow \begin{matrix} A_2^- P \\ \downarrow \\ K^o K^- \end{matrix}$$

at 22.4 and 23.9 GeV/c are $2.64 \pm .10$ μb and $2.51 \pm .07$ μb respectively. These cross sections were calculated for the mass interval of the $K_s^o K^-$ between 1.2 and 1.4 GeV and have been corrected for all t'. The errors shown on the cross sections are statistical only; there is also a 14% rms systematic error on the cross sections.

A fit to the momentum dependence of the cross sections for the reaction $\begin{matrix} \pi^- P \rightarrow A_2^- P \\ \qquad\quad \downarrow \\ \qquad\quad K^o K^- \end{matrix}$ (using our data in conjunction with the total cross-section data from other experiments[1,2]) to the form $\sigma_{Tot} \propto P_{Lab}^{-N}$ yields a value of $N = 1.18 \pm .11$. All the cross sections used in the fit were calculated for events where $1.2 < M(K_s^o K^-) < 1.4$ GeV, and included the correction for all t' regions.

The total cross sections for the reaction $\begin{matrix} \pi^- P \rightarrow A_2^- P \\ \qquad\quad \downarrow \\ \qquad\quad K^o K^- \end{matrix}$ seems to have a momentum dependence which falls off faster than that reported by other investigators[3] for the $\rho^o \pi^-$ decay mode. It appears that

in the reaction

$$\begin{array}{l} \pi^- P \to A_2^- P \\ \qquad\quad \hookrightarrow \rho^o \pi^- \\ \qquad\qquad\quad \hookrightarrow \pi^+ \pi^- \end{array}$$

where $1.2 < M(3\pi) < 1.4$ GeV, the momentum dependence of the total cross section falls off approximately as $\sigma_{Tot} \alpha P_{Lab}^{-N}$ where $N \simeq .58 \pm .18$.

C. Angular Distributions

We have measured the A_2 decay angular distribution in the Gottfried-Jackson frame for the K^oK^- decay of the A_2^-. The projected angular distributions in $\cos\theta$ and ϕ are well fitted assuming a functional form for the angular distribution:

$$W(\cos\theta,\phi) \alpha \mathrm{Cos}^2\theta \sin^2\theta \sin^2\phi$$

and an isotropic background term. The angular distribution may be explained by a dominant exchange of natural spin parity vector mesons (i.e. ρ^o, f^o) in the production process. The A_2 decay angular distributions are consistent with a single resonance having a $J^P = 2^+$.

APPENDIX A

DEFINITION OF t AND t_{min}

The theoretical formulation of the peripheral one-particle-exchange model starts from the Feynman diagram shown below. The incident particles a and b interact with each other by the exchange of particle e; this interaction leads to the particle systems c and d.[16]

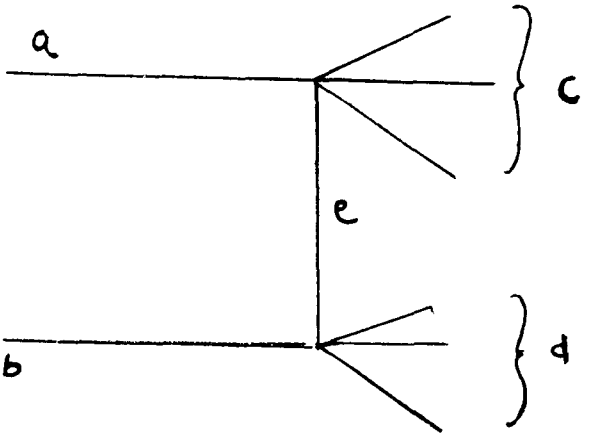

We define a Lorentz Invariant parameter t to be

$$t = (P_c^\mu - P_a^\mu)^2 = (E_c - E_a)^2 - (\vec{P}_c - \vec{P}_a)^2$$

where P_c^μ and P_a^μ are the 4-momenta of all particles in systems c and d respectively. For the reaction $\pi^- P \rightarrow A_2^- P$, we define t to be

$$t = (E_{A_2^-} - E_{\pi^-})^2 - (\vec{P}_{A_2^-} - \vec{P}_{\pi^-})^2$$

or

$$t = M^2_{A_2^-} + M^2_{\pi^-} - 2E_{A_2^-} E_{\pi^-} + 2P_{A_2^-} P_{\pi^-} \cos\theta,$$

where θ is the angle between the incident pion and the outgoing A_2^-. We define t_{min} to be the value of t when $\theta = 0$.

APPENDIX B

CONTRIBUTIONS TO THE ANGULAR RESOLUTION DUE TO FINITE POSITION RESOLUTION

We make a position measurement at two points i and f. The two points lie in a plane and are separated by some perpendicular distance L. (See Figure below.)

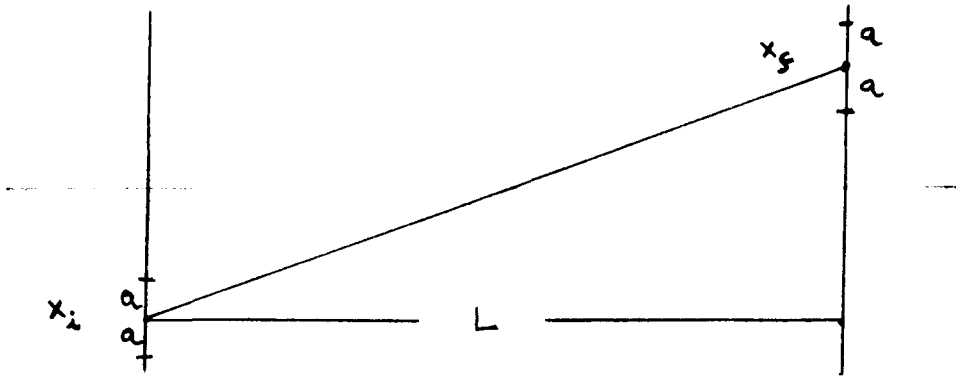

If we have some finite rms position resolution "a" then the position measurements at i and f are uncertain by an amount $x_i \pm a$ and $x_f \pm a$ respectively.

The tangent of the angle would be

$$\tan\theta = \frac{(x_f \pm a) - (x_i \pm a)}{L} \qquad (1)$$

Adding the errors in quadrature, Eq. (1) becomes

$$\tan\theta = \frac{(x_f - x_i) + \sqrt{2}\, a}{L} \,. \qquad (2)$$

For small θ, $\tan\theta$ approaches θ and Eq. (2) reduces to

(3) $$\theta \approx \frac{x_f - x_i}{L} \pm \frac{\sqrt{2}a}{L}$$

and (4) $$\sigma(\theta) \approx \frac{\sqrt{2}a}{L}$$

Equation (4) is valid for one position measurement at i and one at f. The uncertainty in the angle due to position resolution depends directly on the position resolution and inversely as the distance between the measurements. If more than two position measurements are made, then the uncertainty in the angle would decrease by the square root of the number of measurements.

If, instead of taking one measurement at i and f, we took three position measurements, the corresponding

(5) $$\sigma_{\text{position}}(\theta) = \frac{1}{\sqrt{3}} \frac{\sqrt{2}a}{L}$$

The above form for the angular resolution due to finite position measurement assumes that the three position measurements are made at both i and f. However, in our spark chambers, the position measurements (from 4-6 in each leg) are made approximately uniformly along Z; this, coupled with the fact that we do not always get six position measurements in each leg, leads us to believe that the $1/\sqrt{3}$ reduction is an underestimate of the true angular resolution due to position. The expression for $\sigma_{\text{position}}(\theta_{xz})$ if we take N measurements at positions z_N is

$$\sigma_{\text{position}}(\theta_{xz}) = \frac{\sqrt{2}\, a}{(\sqrt{\sum_N z_N^2})\, L}$$

where a is the rms position resolution, L is the length of the lever

arm and the z_N's are normalized such that $z_1 = 0$ and $z_N/L = 1$. Using the actual normalized z_N positions of the planes where the x-position measurements are made, we get that the factor $\frac{1}{\sqrt{\sum_N z_N^2}} \simeq \frac{1}{\sqrt{2.3}}$ for both the back and front legs of the spectrometer.

From the given position resolutions for the upstream and downstream arms of the spectrometer of $\sim$ .010" and .012" respectively, and from the given lever arms in the upstream and downstream arms, 33.4" and 103.0" respectively, we arrive at the calculated value for the position resolution contribution to the angular resolution in the upstream and downstream arms:

$$(6) \quad \sigma_{\text{position}}(\theta_{xz})_{\text{front}} \simeq \frac{\sqrt{2}\ (.010)}{\sqrt{2.3}\ (33.4)} = .279 \text{ mrad}$$

$$(7) \quad \sigma_{\text{position}}(\theta_{xz})_{\text{back}} \simeq \frac{\sqrt{2}\ (.012)}{\sqrt{2.3}\ (103.0)} = .101 \text{ mrad.}$$

BIBLIOGRAPHY

1. M.J. Losty, Private Communication, CERN, European Organization for Nuclear Research, Geneva, Switzerland.

2. H. Dietl, Private Communication, Max-Planck Institute of Physics, Munich, Germany.

3. G. Ascoli, Data presented at the XVIIth International Conference on High Energy Physics, London, England (1974), Sec. II-11.

4. G.E. Chikovani, M.N. Focacci, W. Kienzle, C. Lechanoine, B.L. Levrat, B. Maglic, M. Martin, P. Schubelin, L. Dubal, M. Fischer, P. Grieder, H.A. Neal and C. Nef, Phys. Lett. 25B, 44 (1967).

5. H. Benz, G.E. Chikovani, G. Damgaard, M.N. Focacci, W. Kienzle, C. Lechanoine, M. Martin, C. Nef, P. Schubelin, R. Baud, B. Bosnjakovic, J. Cotteron, R. Klanner, and A. Weitsch, Phys. Lett. 28B, 233 (1968).

6. R. Baud, H. Benz, B. Bosnjakovic, D.R. Botterill, G. Damgaard, M.N. Focacci, W. Kienzle, R. Klanner, C. Lechanoine, M. Martin, C. Nef, V. Roinishvili, P. Schubelin, A. Weitsch, H. Blumenfeld, H. Jostlein and P. Lecomte, Phys. Lett. 31B, 397 (1970).

7. D.J. Crennell, U. Karshon, K.-W. Lai, J.M. Scarr and I.O. Skillicorn, Phys. Rev. Lett. 20, 1318 (1968).

8. K. Bockman, et al., Bonn-Durham-Nijmegen-Paris (E.P.)-Torino Collaboration, Nucl. Phys. B16, 221 (1970).

9. M. Alston-Garnjost, A. Barbaro-Galtieri, W.F. Buhl, S.E. Derenzo, L.D. Epperson, S.M. Flatte, J.H. Friedman, G.R. Lynch, R.L. Ott, S.D. Protopopescu, M.S. Rabin and F.T. Solmitz, Phys. Lett. 33B, 607 (1970).

10. K.J. Foley, W.A. Love, S. Ozaki, E.D. Platner, A.C. Saulys, E.H. Willen and S.J. Lindenbaum, Phys. Rev. D6, 747 (1972).

11. G. Grayer, et al., Phys. Lett. 34B, 333 (1971).

12. C.M. Ankenbrandt, B.B. Brabson, R.R. Crittenden, R.M. Heinz, J.C. Krider, J.E. Mott, H.A. Neal and A.J. Pawlicki, Phys. Rev. Lett. 29, 1688 (1972).

13. D. Bowen, D. Earles, W. Faissler, D. Garelick, M. Gettner, M. Glaubman, B. Gottschalk, G. Lutz, J. Moromisato, E.I. Shibata, Y.W. Tang, E. von Goeler, H.R. Blieden, G. Finocchiaro, J. Kirz, and R. Thun, Phys. Rev. Lett. 26, 1663 (1971).

14. Particle Data Group, Rev. Mod. Phys., Supplement April 1973.

15. G. Kallen, Elementary Particle Physics (Addison-Wesley Publishing Co., Inc., Reading, Mass., 1964) p. 317.

16. N. Schmitz, in Proc. of the 1965 Easter School for Physicists, Bad Kreuznach, Germany (1965).

17. K. Gottfried and J.D. Jackson, Nuovo Cimento 33, 309 (1964).

18. K.J. Foley, S.J. Lindenbaum, W.A. Love, S. Ozaki, E.D. Platner, A.C. Saulys and E.H. Willen, Nucl. Instrum. Meth. 108, 33 (1973).

19. J.M. Paul, Nucl. Instrum. Meth. 96, 51 (1971).

20. R.M. Bozorth, Ferromagnetism (D. Van Nostrand Co., Inc., Princeton, N.J., 8th printing, 1964) p. 627.

21. D.H. Wilkinson, Nucl. Instrum. Meth. 95, 259 (1971).

22. F. James and M. Roos, D506, D516, CERN Computer Program Library.

23. J.D. Jackson, Nuovo Cimento 34, 1644 (1964).

24. This shape is similar to that suggested by Quigg and von Hippel, Experimental Meson Spectroscopy (Columbia University Press, New York, 1970) p. 477.

25. E. Flaminio, J.D. Hansen, D.R.O. Morrison, N. Tovey, Compilation of Cross Sections VI: π^- Induced Reactions, Geneva, Switzerland (Oct. 1970).

26. S.J. Lindenbaum, Particle-Interaction Physics at High Energies (Oxford University Press, 1973) p. 397.

27. E. Bracci, J.P. Droulez, E. Flaminio, J.D. Hansen and D.R.O. Morrison, Compilation of Cross Sections II: K^- and K^+ Induced Reactions, Geneva, Switzerland (Oct. 1972).

28. It has previously been shown that this expression fits two-body reactions and that the exponent n is related to the exchange mechanism which dominates the reaction. See for example, D.R.O. Morrison, Stony Brook Conference on Two-Body Reactions (1966).

29. Elton Duane Schafer, Ph.D. Thesis, University of Illinois.

30. C. Michael and P.V. Ruuskanen, Phys. Lett. 35B, 47 (1971).

31. R.H. Dalitz, Lecture Series, The Production and Decay of Resonant States, Oxford University, London, p. 141.

32. H. Dietl, Ph.D. Thesis, Max-Planck Institute of Physics, Munich, Germany.